PDC
Center for Parallel Computers

Progress Report 1998-1999

Progress Report
1998-99

PDC
Parallelldatorcentrum

Progress Report
1998-99

VETENSKAP
OCH
KONST

KTH

Front Cover Pictures

Top row, far left and far right: The singly occupied orbital of the tetragonal and trigonal $Cu(SH)(NH_3)_3+$ complex1 (see figure 5.8 on page 63).

Top row, middle: Vortex breakdown over a double-bevel delta-wing model, turbulent computation (see figure 5.13 on page 66).

Middle row, left: Blade passage meshes for the NASA Rotor 67 (see figure 5.21 on page 72).

Middle row, right: Protons on clean mica surface (see figure 5.4 on page 60).

Bottom: A DPPC membrane patch sized 16×16 nm. This system consists of 121,856 atoms including water and is the largest membrane simulation performed to date (see figure 5 on page 58).

Contents

Foreword

The first *PDC Progress Report* covered the years 1990–1991. The current report covers research at Swedish academic institutions enabled by the PDC facilities during the final two years of the final decade of the millennium.

There are six progress reports from PDC describing the fascinating progress in high-performance computing during the 1990s. It is interesting to reflect on the change that has occurred.

During the first years, many of the projects emphasized computer science issues. The Connection Machine, which was the first parallel computer for broad academic use in Sweden, had just been installed at KTH, and PDC was formed in 1990. It became important to learn how to benefit from this new technology, and this led to the concentration on parallel algorithmic and implementation issues.

Later progress reports show the maturity of high-performance computing in the Swedish academic community. The project reports concentrate much more on the scientific achievements that were facilitated by the use of this new computing power. High-performance computing in general and parallel computing in particular have now become natural tools in many scientific disciplines.

During this decade, the computational capability at PDC has gradually increased to meet the increasing demand from the user community. Researchers can now run their jobs on 300 IBM SP processors at 200 Gflop/s, using 100 Gbytes of memory. They also have access to substantial vector processing power.

PDC has recently expanded its capabilities in the areas of visualization and mass storage technology. The effect of this is not yet seen in the progress reports. We are confident that these new facilities will soon become natural tools in research, similar to parallel computing in the beginning of the decade.

Visualization and mass storage techniques should also be beneficial to new fields of research outside the more traditional users of high-performance computing.

I would like to thank the editors of *PDC Progress Report* through-

out the past decade. The progress reports in the future will most likely have a new format and will be seen as a complement to other forms of presentations on the Web and in regular journals and proceedings.

Björn Engquist
Director
Stockholm, 2000

1 Parallelldatorcentrum: PDC

This sixth progress report of Parallelldatorcentrum (PDC, Center for Parallel Computers) at Kungliga Tekniska Högskolan (KTH, Royal Institute of Technology) covers the activities of the center from the end of 1997 up until the end of 1999. Chapter 1 includes a brief overview of the most important events at the center during this period, as well as information about the center's hardware and usage. The PDCTTN is described in Chapter 2, and user projects are described in Chapter 3 through Chapter 8.

1.1 Background

The center was formed in January 1990 to act as a focal point and national forum for research on and use of parallel computers. Our goal is to stimulate research and education using high-performance computing and rich visualization environments, and to disseminate information about these areas.

The center is a national forum for research.

This goal is approached by providing high-performance parallel computers, two virtual reality enviroments for visualization and knowledge discovery, and expertise on their use for the benefit of Swedish academic institutions. The facilities are predominantly used by the engineering and science communities, but an increased interest from other disciplines, such as medicine, architecture, and art is noticeable.

1.2 Events and Educational Activities

A number of seminars, workshops, classes, and conferences have been held at PDC during 1998 and 1999. Table 1.1 and 1.2 show some of the most important of these events. The computing resources at PDC are regularly used in graduate and undergraduate courses at KTH and CTH.

PDC resources are regularly used in courses.

Table 1.1. Events in 1999

1999	
PDC Annual Conference: "Simulation and Visualization on the Grid"	December 15–17
PDC Anniversary Seminar: "A Celebration of PDC's Tenth Anniversay"	October 18
Niornas vecka (Ninth-Graders' Week): "The Basics of High-Performance Computing"	October 13–15
Barbara Chapman Seminar: "Current Parallel Programming Paradigms"	October 4
John Levesque Seminar: "The IBM Roadmap towards Teraflop Computing"	September 29
David Jackson Seminar: "The Maui Scheduler"	September 23
PDC/NGSSC Summer School: "Introduction to High-Performance Computing"	August 16–27
RoboCup: "World Championships in Robot Soccer"	August 4– July 29
Gymnasisternas vecka (High School Students' Week): "The Basics of High-Performance Computing"	April 19–22

1998	
PDC Annual Conference: "High-Performance Computing in Visualization and VR"	December 17–18
User Workshop: "SMP Programming for IBM SP"	November 17–18
User Workshop: "Cluster and Distributed Computing Workshop"	September 24–25
Nordic IBM SP User Group (NSPUG)	September 14
PDC/NGSSC Summer School: "Introduction to High-Performance Computing"	August 17–28
User Workshop: "Introduction to Parallel Computing on the IBM SP"	April 21–22 March 4–5
Dr. Dan Edelstein (IBM Research) Seminar: "Copper Technology in Chip Manufacturing: Prespectives for the Future"	April 21
First Meeting of the Nordic IBM SP User Group	April 20–21

Table 1.2. Events in 1998

1.3 Hardware Resources

Networking

PDC is connected directly to the KTH Network Operations Center, KTHNOC, via a dedicated FDDI connection. KTHNOC is also managing the NOCs for SUNET and Nordunet. Internally, PDC has implemented a high-speed network infrastructure to support large-scale I/O and enable computational clusters of PDC systems. An Ascend/Netstar Gigarouter is the heart of the network, with a HiPPI connection to large systems and FDDI connections to various networks. All large systems are connected to a HiPPI network (800 Mbp/s) via a NetStar HiPPI ClusterSwitch. Other systems, such as AFS file servers, are connected to a number of FDDI (100 Mbp/s) rings separated by a Digital Equipment Corp. FDDI GigaSwitch.

Current Hardware

- Strindberg, a 300 CPU IBM SP consisting of 178 nodes: 148 P2SC nodes, 22 four-way 604e SMP, and 8 Nighthawk nodes. There are about 2,000 Gbytes of disk available to users. The peak performance of the Strindberg system is 204 Gflop/s, and the total memory is 115 Gbytes.

- Kallsup, a CRAY J932se managed by PDC for the KALLSUP Consortium at KTH. The peak performance is 6.4 Gflop/s, the total memory is 8 Gbytes, and the total disk space is 225 Gbytes.

- Selma, a vector computer from Fujitsu, with three processors, providing 6.6 Gflop/s and 2 Gbytes memory each. The system is equipped with 36 Gbytes of SCSI disk and 63 Gbytes of high-performace HiPPI disk.

- Boye, an SGI Onyx2 computer with 12 R10000 CPUs, 4 Gbytes of memory, and 120 Gbytes of disk. It is also equipped with three InfiniteReality2 graphics pipes, each with two raster managers with 64 Mbytes of memory.

- Sprat, an SGI Octane computer equipped with 2 R10000 CPUs and a total of 1 Gbyte of memory and EMXI graphics. It is used for computation and visualization purposes, specifically for use with the ImmersaDesk.

- A projection-based ImmersaDesk driven by Sprat. The Immersa-Desk enables 3D group viewing in a virtual reality environment.

- The PDC VR-CUBE (the Cube), a fully immersive visualization environment forming a $3 \times 3 \times 2.5\,\text{m}$ ($W \times D \times H$) room driven by Boye. The unique feature of this virtual reality system is the display of images on all surrounding surfaces, including the floor and the ceiling.

  The PDC VR-CUBE is a fully immersive visualization environment.

  Each of Boye's graphics pipes manages two of the six surfaces. The floor and ceiling are currently configured for a resolution of 1024×1024 pixels at a frequency of $96\,\text{Hz}$ (*i.e.*, $48\,\text{Hz}$ per eye, due to stereo projection). The walls are configured for a resolution of 1024×852 pixels to keep the pixels square and to keep the resolution constant along the edges.

Mass Storage

Mass storage, provided by an IBM 3494 Tape Library Dataserver with four IBM 3590 Magstar tape drives, can store up to $12\,\text{Tbytes}$ of data. The Hierarchical Storage Management (HSM) system currently runs on the CRAY J932se. The HSM functionality is provided by the Data Migration Facility (DMF) from SGI CRAY.

Parallel File System

The computer Strindberg offers a fast file system through IBMs General Parallel File System (GPFS) for high-performance I/O. GPFS can be used as a large ($60\,\text{Gbytes}$) scratch file system, or for storing large files temporarily.

1.4 Resource Usage

Currently, all scheduling on the IBM SP at PDC is performed by PDC's derivative of the EASY scheduler. The usage is kept at a continously high level. Two planned shut downs for hardware and software upgrades were made: one in January of 1998, and one in March of 1999.

Figure 1.1. The percentage of total used computer time on the IBM SP for different scientific disciplines for each half of 1998 and 1999.
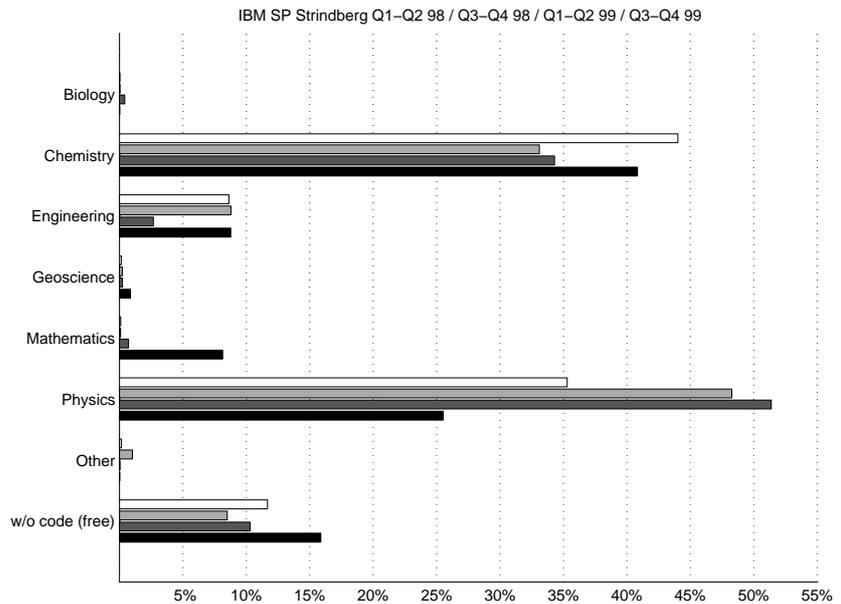
Figure 1.2. Used computer time per month on the IBM SP during 1998 and 1999. In January of 1998 Strindberg was taken out of production for an upgrade to increase the number of nodes. In March of 1999 Strindberg was taken out of production for 5 days for a major upgrade of systems and hardware.

IBM SP Strindberg Q1–Q2 98 / Q3–Q4 98 / Q1–Q2 99 / Q3–Q4 99
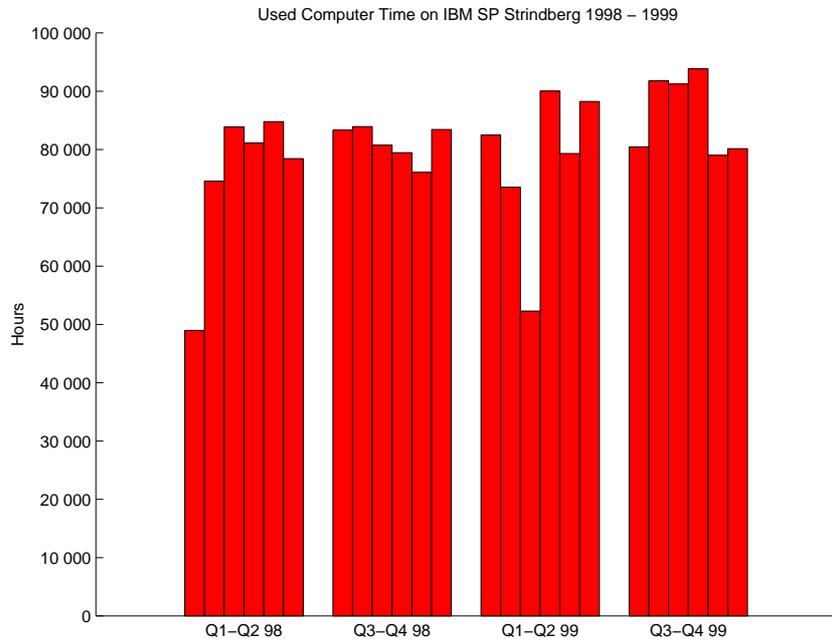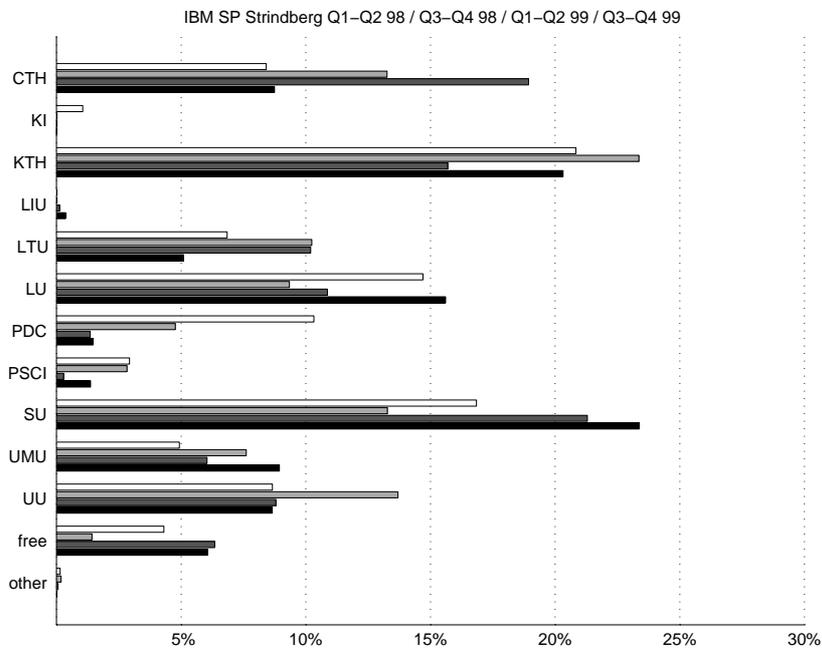
Figure 1.3. The percentage of total computer time used by the different Swedish universities. For each university, the numbers are presented by period (Q1–Q2 98, Q3–Q4 98, Q1–Q2 99 and, Q3–Q4 99) from top to bottom. The label "free" indicates low-priority jobs running free of charge and allocating otherwise unused computer time. PSCI is the NUTEK Center of Excellence in Parallel and Scientific Computing, and it is charged for its computing time.

2 PDC Technology Transfer Node: PDCTTN

In order to start the process of technology transfer with Swedish industry, PDC/PSCI established PDCTTN, the Swedish European HPCN Technology Transfer Node, in April of 1997. Interest from industry to develop HPCN solutions was achieved in 1997, leading to more than fifteen proposals forwarded to the European Commission, of which six were accepted.

PDCTTN initiated and coordinated the following PST (preparatory, support, and transfer) activities: VIDEOGRAPH, SIMMILL, OPTIBLADE, IDASTAR, OPTIMOM, and 3Demo. All of these resulted in technology transfer between end users on the one hand and technology providers/HPCN experts on the other. To ensure the European dimension, all activities have had partners from different European countries—Denmark, Finland, France, Norway, and Switzerland. Based on the characteristics of the PST activities and to ensure having a framework for marketing and disseminating the PST results, PDCTTN chose to be an active member in four of the HPCNTTN defined industry sector groups: Aerospace, Construction, Machinery, and Media & Entertainment. Figure 2.1 shows the locations of the European TTN network. The following results can be seen.

- PDCTTN and its PST activities have finished with encouraging results. New and improved products, new services, further development projects, as well as new companies have spun off. From a financial standpoint, the partners estimate an increase generated from the projects—today and three-year onwards: in turnover by a factor 4.5; in profit by a factor 5.5 and; additional employment by a factor 3. As a consequence, the European citizen will see additional and new employment in the future as well as environment savings due to optimized manufacturing cycles in industry—avoiding risky errors and achieving less faulty products.

- Together with partners in the PST activities, contacts with industry have been established. Roughly 10,000 SMEs (small- and

Figure 2.1. Locations of the European TTN network.
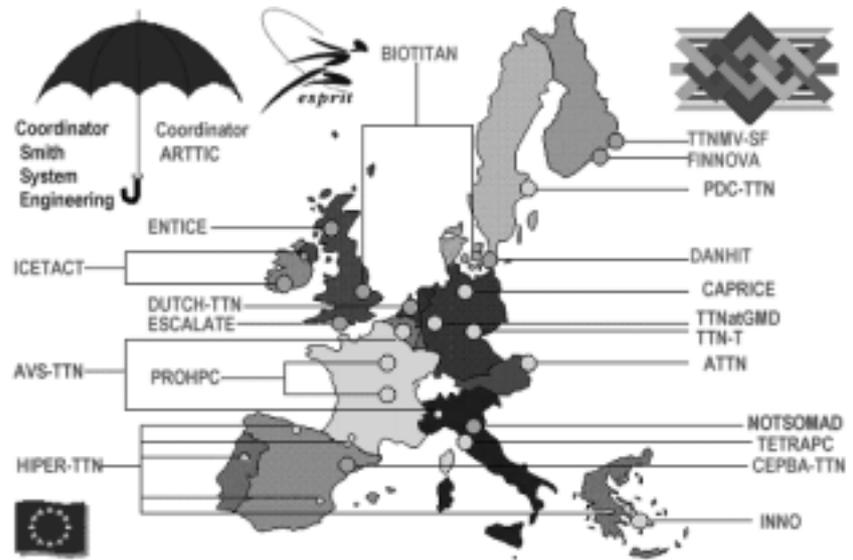
medium-sized enterprises), mainly in building and machinery, have been targeted in Sweden and Finland through press articles, participation at events, fairs, *etc.* An estimated 5 percent have shown interest or simply been chosen to be directly contacted as potential prospects. Together with PST partners, today a dialogue is going on with an estimated 50 SMEs, trying to understand and meet specific HPCN requirements to support their business goals.

- Important contacts have been established with industry organizations, often leading to further cooperations and joint actions.

- Industries have been able to see interesting solutions and openings to their day-to-day problems. Compared to before the start of the HPCNTTN program, today's offerings are better described and positioned for SMEs. The dialogue starts from an interest in business and non-technology advantages, enabling a wider business community to get involved. Industry exposure shows that few businesses will accept HPCN due to its scientific background, but rather are interested in solutions and the potential business benefits from those solutions.

- Being a member of a European network is essential to get enough awareness, impact, and respect from industry. To be based only

on a national level is not enough if the goal is transfer technology to European industry. It is highly important to have access to a critical mass of experience and knowledge. To be a member of HPCNTTN network has therefore proven to be an important element in our everyday work.

More information is available from the PDCTTN coordinator Marina Backer Skaar `pdcttn@pdc.kth.se` or at `http://www.pdc.kth.se/pdcttn/`.

3 Biology

3.1 Carbohydrate Dynamics Systems

Christer Höög, Göran Widmalm
Department of Organic Chemistry, Arrhenius Laboratory,
Stockholm University

The dynamic as well as structural properties of carbohydrates and surrounding waters have been investigated by molecular dynamics (MD) simulations. At the present time, the systems studied consist of oligosaccharides (2–12 sugars) in water solution (up to $\sim 4,000$ water molecules) and counter ions (sodium) to negatively charged groups on the sugars.

A simulation usually spans 1–10 nanoseconds (ns). A number of starting conformations are used to facilitate good sampling of conformational space. As an example, the flexibility and the conformational preference of a glucotriose oligosaccharide (figure 3.1 on page 14) were studied by MD simulations. A 10-ns trajectory is shown in figure 3.2 on page 15, where transitions to and from different conformational states occur on a nanosecond time-scale. In total, 83 ns were simulated for this system using the TIP3P water model as solvent with the CHARMM program on the IBM SP.

Extensive simulation times are needed to obtain some confidence in the sampling of the conformational space for a system as small as a trisaccharide in solution. Commonly, these simulations make use of 16–32 nodes. Comparison of the simulations to high-quality experimental nuclear magnetic resonance (NMR) data makes it possible to interpret the results in a quantitative way, not previously done for such a system in water solution.

Simulations of larger oligosaccharides with 12 sugar residues also carrying negatively charged carboxyl groups have been initiated. Sodium is used as counter ion. For simulations of this type, it is important not to truncate potential functions at a distance that is too short. We are therefore using an 18 Å cut-off for the non-bonding interactions. First, longer interactions are needed; second, this results in larger box sizes to be simulated, increasing the simulation requirements. For these systems we use a cubic box with a side length of ~ 50 Å.

Figure 3.1. Schematic representation of the glucotriose oligosaccharide simulated by the MD technique.
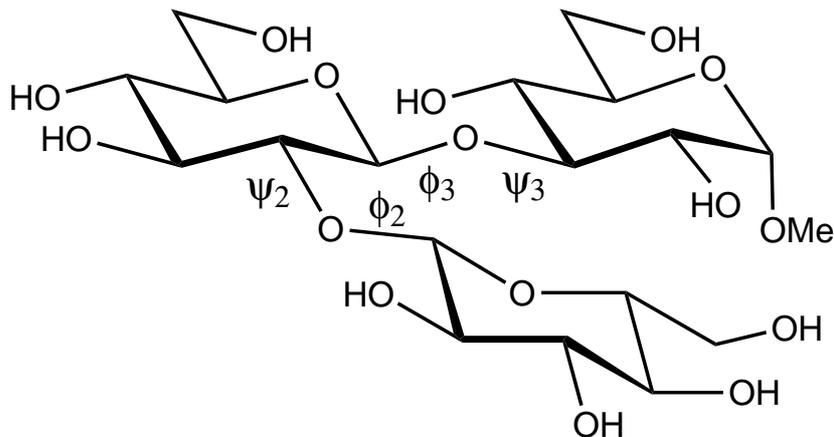
The predictive power of these simulations is to be used to obtain new insights into the properties and behavior of carbohydrates.

3.2 Dynamic Properties of Membranes

Erik Lindahl, Olle Edholm
Department of Theoretical Physics, KTH

This project concerns the study of order and dynamical properties at interfaces in biological systems, in particular biological membranes. These membranes consist of a special sort of molecules, phospholipids, with one hydrophobic and one hydrophilic part. In an aqueous solution, they will form double layers where the hydrophobic ends point towards each other on the inside and the hydrophilic parts face the water (see figure 5.1).

However, a membrane is much more complex than a simple wall! At physiological conditions they are very flexible and behave more or less like fluids. This is crucial for all living organisms, because it gives the cell a possibility to selectively transport atoms and even insert whole proteins into the membrane. It thus has a double role—it is passively upholding concentration gradients and also hosting active transport proteins.

Unfortunately, their flexible properties make membrane systems quite hard to study by experimental methods. That's were PDC enters. Computer simulations offer a possibility of studying these systems and their interactions, without the limitations posed by experiments. There are however other obstacles to overcome: To

Computer simulations offer a possibility of studying systems and their interactions, without the limitations posed by experiments.
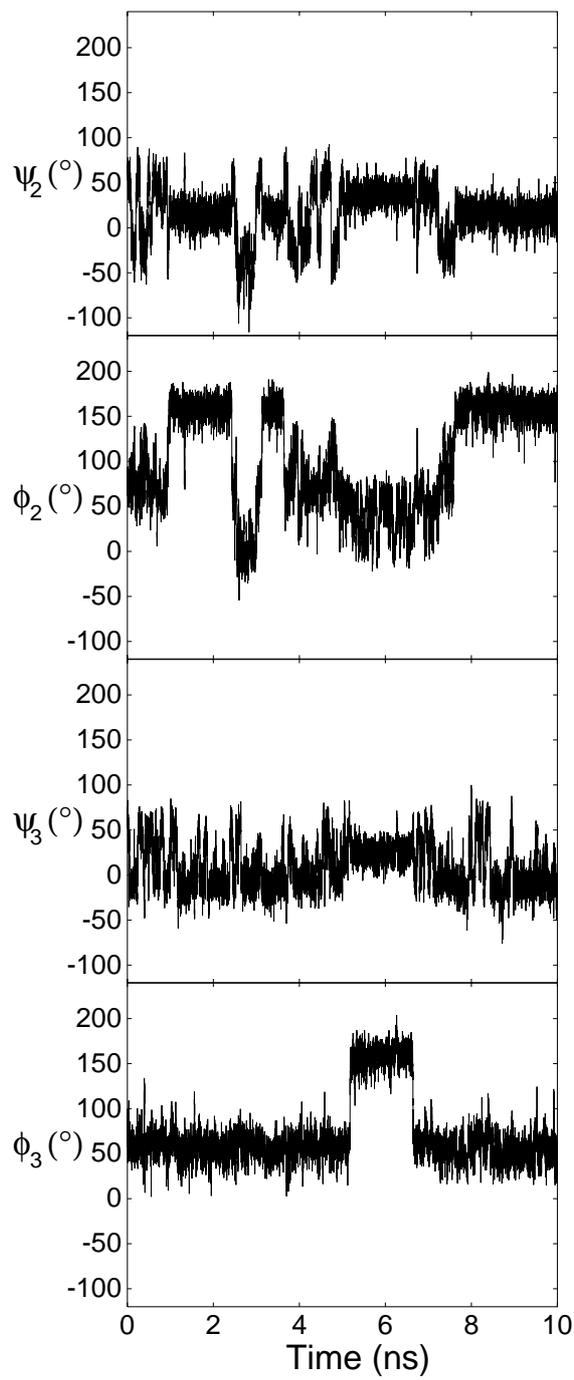
Figure 3.2. Torsion angle trajectories for the major degrees of freedom of the oligosaccharide shown above.

make predictions about the behavior of real-world systems from computer simulations, we must first let the system equilibrate in the simulation and then follow it long enough to get good statistical data. A membrane with a protein in it can consist of up to 100,000 atoms, and so only the recent advances in computer speed and parallelization have made it possible to perfom such simulations.

The first problem when simulating membranes is that the molecular dynamics force fields are not designed for lipid bilayers, but rather for proteins in water. Most simulations (see *e.g.*, [Egberts *et al.*, 1994]) therefore end up with an area and/or volume per lipid differing from the experimental values [Nagle, 1993]. Recently, however, Berger and Edholm developed a new set of parameters that reproduces the experimental results within $1\,\%$ [Berger *et al.*, 1997b]. These new force field parameters introduce the possibility of accurately predicting experimental entities like diffusion coefficients and free energies from simulations.

In the first stage of this project, we're developing and porting the simulation program to the IBM SP, and we've begun to study scaling effects due to the periodic boundary conditions to which the system is subject. The area per lipid does indeed show a clear dependence on the size of the entire system, and we are presently trying to explain this theoretically in terms of correlation effects between the dipoles. With the computational resources at PDC we've also been able to perform simulations of a very large system to study oscillations and collective motions of the entire membrane.

We are further investigating the ordering of water molecules outside the membrane. Close to the surface, the water molecules show a large degree of order and decreased mobility. This has important implications both for the electrostatic interactions with the membrane dipoles and for the dynamics of the water itself. We are modeling this with a generalized langevin system where the particles are subject to both a random force from their neighbors and a deterministic one from the membrane. In many ways, a membrane is much better suited as a model system for such dynamics than proteins, because the latter has a very irregular surface [Lindahl and Edholm, 1998]

For the simulations, we use a newly developed molecular dynamics implementation [Berendsen *et al.*, 1995] especially tailored

for message-passing architectures like the IBM SP. All programs are written in C to be easily readable, while inner loops are written in FORTRAN for speed reasons. Special optimizations have been implemented to improve calculations of common molecules like water and math functions like $\frac{1}{\sqrt{x}}$. The resulting code is faster by about a factor of four than other major molecular dynamics packages. To further increase the scaling, we use a non-iterative constraints solver [Hess *et al.*, 1997].

The resulting code is faster by about a factor of four than other major MD packages.

All the parts of our simulations parallelize well, so the limiting factor is the communication between processors. Fortunately, this is where Strindberg really shows off compared to a workstation cluster, for example. Our largest simulation system (see figure 5) parallelizes nicely on 30–40 processors. We've also had great use of the 2048-Mbyte memory node for calculating autocorrelation functions.

3.3 Long-Range Electrostatics in Molecular Dynamics Simulations of Lipid Bilayers

Alexander Lyubartsev, Aatto Laaksonen
Division of Physical Chemistry, Arrhenius Laboratory,
Stockholm University
Olle Edholm, Erik Lindahl, Lars Sandberg
Department of Theoretical Physics, KTH

Phospholipids are the essential components of biological membranes. In order to understand the function of membranes, it is necessary to have knowledge of the structure and dynamical behavior of the lipids in atomic detail. Computer simulation techniques are natural tools to achieve this goal. However, the understanding of molecular mechanisms of lipid bilayers for the structure and dynamics is still a challenging problem. The problem requires fairly large systems (10,000–200,000 atoms) and long simulation times (1–100 nanoseconds). Moreover, some properties are extremely sensitive to details in the simulation protocol and the applied force field. A typical simulation of this type requires about 40 CPU-days on a fast workstation. Studies involving variation of parameters in the force field or simulation protocol easily requires a CPU-year on workstations.

Computer simulation techniques are natural tools to achieve this goal.

The present work used previous simulations [Berger *et al.*, 1997a] as its point of departure. In that study a careful calibration of the

Lennard-Jones parameters of the fatty acid chains of the dipalmitoylphosphatidylcholine (DPPC) molecules was done against experimental data for long-chain liquid hydrocarbons. Good agreement with experiments was achieved for many parameters, especially for the volume density of lipid bilayers. However, this model is still crude. It uses a unified atom description of the hydrocarbon groups of the lipids, a fairly short cutoff for the electrostatic interactions, and a water model that, although well tested and much used, still could be improved. Furthermore, there is still no consensus among various groups doing lipid simulations about the modeling of fractional charges for the different atoms in the lipid head group. But, the model used gives good results for most of the quantities that are accurately available from experiments.

One important property that comes out differently from different simulations is the surface area per lipid at constant pressure, or, alternatively, the anisotropic pressure (surface tension) at constant surface area. There is a negative contribution to the surface tension from the electrostatic interactions in the water head group region and a positive contribution from the short-range Lennard-Jones interactions in the lipid tail region. Long-range interactions are important only for the electrostatics, which indicates that an improved description of this part of the problem is essential to model the anisotropy correctly.

The necessity for an improvement of the lipid simulations stems from the fact that structure and dynamics in the head group region is very sensitive to several properties of the simulation protocol, such as fractional charges, choice of cutoff, and water model. Monitored through one variable, this is most clearly seen from the variation of the electrostatic potential across the membrane. The simulations recently started on the IBM SP at PDC will systematically test some properties of the lipid bilayer models and evaluate a new model seeking to improve especially the electrostatic field representation.

The software is a molecular dynamics program [Edholm, 1998, Lyubartsev and Laaksone, 1998], developed and tested on simulations of DNA and some smaller molecules (See figure 3.3). It was designed and developed for efficient parallelization using message-passing techniques.

Main features include the use of a double time-step algorithm to separate fast and slow motions, as well as the inclusion of an

Main features include the use of a double time-step algorithm to separate fast and slow motions, as well as the inclusion of an Ewald summation to treat long-range Coulombic interactions.
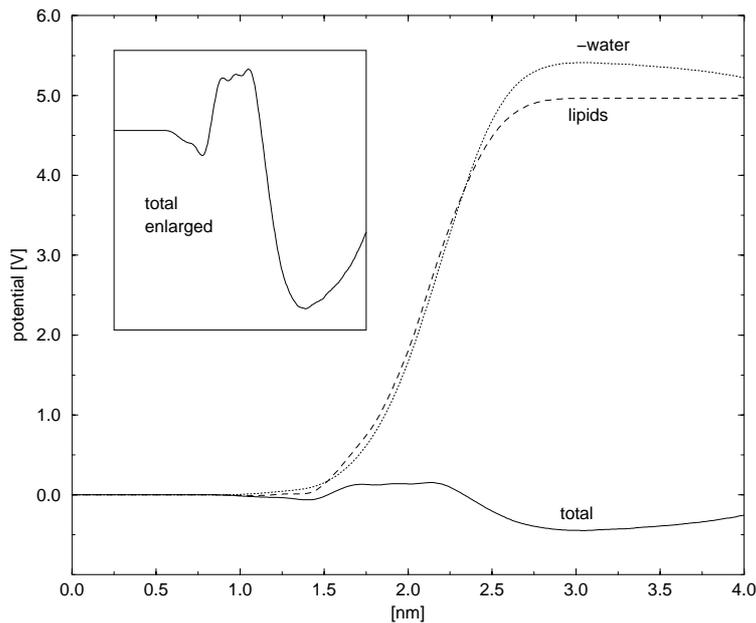
Figure 3.3. The electrostatic potential across the lipid bilayer calculated from a simulation. The potential is about 0.4 V lower in water as compared to the center of the bilayer. The experimental figure is 0.2–0.5 V.

Ewald summation to treat long-range Coulombic interactions. The speed is almost linear in the number of processors up to at least 32 processors. This makes simulations possible that could not have been done on a single workstation.

One purpose of the simulations was to study the hydration properties of the lipid head group for different water models. The degree of hydration affects the dipole moment associated with the hydrated head group, which in turn influences long-range electrostaic properties of the whole system. During 1998, simulations were made of the DPPC lipid bilayer in presence of the flexible SPC water model using Ewald summation for the electrostatic interactions. The simulations were run on the IBM SP Strindberg, normally using 16 processors. The results for the 3D water structure around the lipiad head are given in figure 5.3 on page 59. Testing of other water models and molecular dynamics protocols is in progress.

3.4 Monte Carlo Study of the Phase Structure of Compact Polymer Chains

Anders Irbäck, Erik Sandelin
Department of Theoretical Physics, Lund University

The thermodynamic behavior of isolated homopolymer chains is known in quite some detail at and above their collapse temperature $T = T_\theta$, from analytical work and numerical simulations of very long chains. Much less is known about their behavior at low temperatures. Knowledge of the low-T phase behavior may, in particular, shed light on the mechanism of folding for heteropolymers.

Knowledge of the low-T phase behavior may, in particular, shed light on the mechanism of folding for heteropolymers.

The possibility of an interesting low-T phase structure for homopolymers was predicted several years ago. Recent studies of lattice chains with stiffness have shown that such chains, in addition to the coil-globule transition at T_θ, exhibit a phase transition from the globule phase to a frozen crystalline phase.

In the present study, our starting point was a simple off-lattice model for protein folding with two types of monomers, A (hydrophobic) and B (hydrophilic). In addition to "hydrophobicity" forces, the model also contains sequence-independent local interactions (stiffness terms). A detailed study of A homopolymers in this model was performed, both with and without the local interactions. The results were compared to results for non-uniform AB sequences with known folding behavior.

The most striking feature of the homopolymers, at least for small chain lengths, is a pronounced peak in the specific heat, located well below T_θ. Similar findings have been reported for related models. This could signal that these chains, like lattice chains with stiffness, undergo a low-T phase transition. A careful examination showed, however, that the system size dependence at these temperatures is weak for chains with up to $N = 50$ monomer units. In particular, the specific heat itself seems not to diverge with increasing N.

Simulating the low-T behavior of these systems is computationally demanding. Our calculations were carried out using simulated and parallel tempering, both of which were found to be much more efficient than conventional Monte Carlo methods. An additional advantage of parallel tempering is that it is very easy to parallelize. We used simulated tempering on workstations for our smaller sys-

tems, and parallel tempering implemented on the IBM SP machine at PDC for the larger ones.

In parallel tempering one simulates the distribution

$$P(r_1, \ldots, r_K) \propto \prod_{k=1}^{K} \exp[-E(r_k)/T_k], \qquad (3.1)$$

where each r_k represents a complete chain conformation and $\{T_k\}$ is a predetermined set of allowed temperatures. The simulation is carried out by using two types of updates: ordinary, parallel updates of the different r_k; and accept/reject controlled swaps $r_k \leftrightarrow r_{k+1}$.

When parallelizing this algorithm, the K chains are put on different nodes. The swaps $r_k \leftrightarrow r_{k+1}$ can be accomplished by simply exchanging temperatures between the corresponding nodes. This is the only communication needed in the method. Also, no load balancing is required. Hence, the algorithm is almost ideally parallelizable. Simulating the low-T behavior of an $N = 50$ chain required approximately 500 CPU hours on the IBM SP.

It should be stressed that parallel tempering performs much better than standard Monte Carlo methods already on serial machines; the fact that it is highly parallelizable is only a bonus. In figure 3.4 we compare the performances of simulated and parallel tempering and a standard Monte Carlo. Shown are run-time histories for the sum of all torsional angles along the chain, α, from three simulations of the same system. The horizontal axis can be thought of as CPU time. Note that the system is trapped at negative α during the whole standard Monte Carlo simulation. From the symmetry of the model, it is known that the actual probability distribution of α is symmetric, $P(-\alpha) = P(\alpha)$. [Irbäck and Sandelin, 1999]

Parallel tempering performs much better than standard Monte Carlo methods already on serial machines.

3.5 Quantum Chemical Studies of Chemical Reactions of Biological Importance

Tore Brinck, Ching-Han Hu
Department of Physical Chemistry, KTH
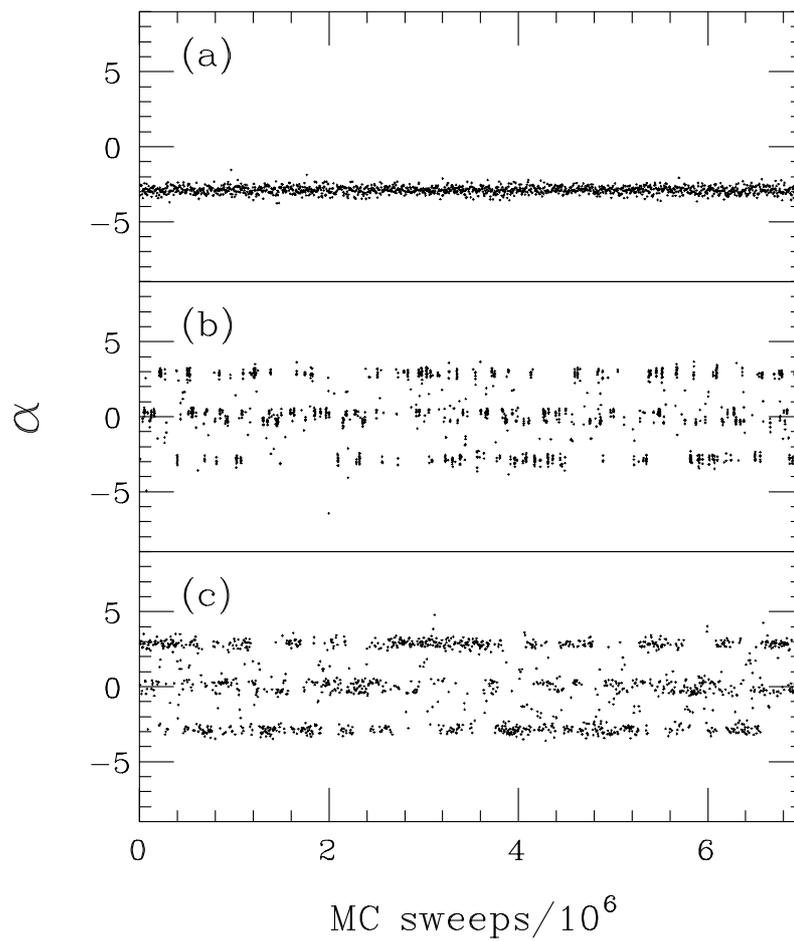*Fredrik Haeffner*
Department of Organic Chemistry, KTH

In recent years we have devoted much of our research efforts to studying the catalytic mechanisms of hydrolytic reactions in dif-

Figure 3.4. Evolution of the sum of all torsional angles, α, in three different simulations of an $N = 12$ A homopolymer: (a) standard Monte Carlo, (b) simulated tempering, and (c) parallel tempering.
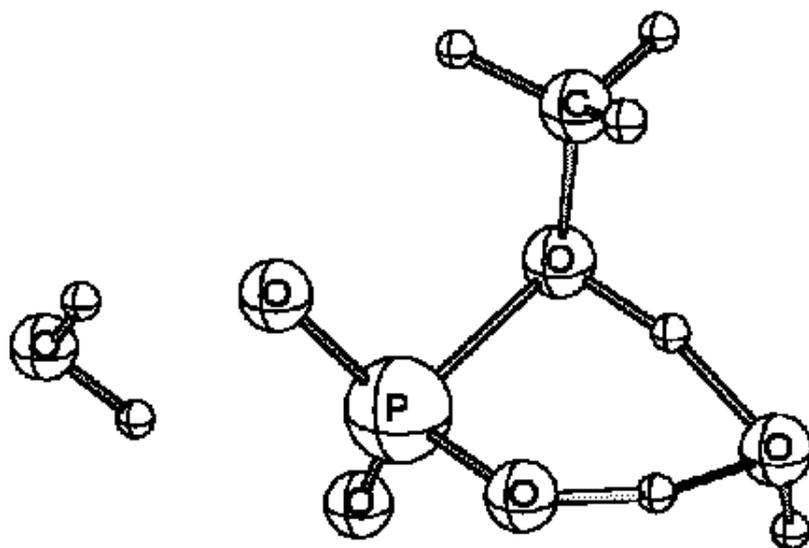
ferent media. Our results on the hydrolysis of carboxylic esters in serine hydrolase enzymes were discussed in the *PDC Progress Report 1997* [Hu *et al.*, 1998]. Since then we have extended our research to other enzymes and to hydrolysis in aqueous solution. We have developed a methodology for studying reactions in solutions in which we represent the solvent by a combination of a few explicit solvent molecules and a polarizable continuum model. Using this method, we have shown that solvent molecules play an active role during base-catalyzed hydrolysis of carboxylic esters, that is, the proton transfer step of the reaction proceeds via a six-centered water-assisted transition state [Haeffner *et al.*, 1999]. A similar type of transition state was also found in the dissociative reaction mechanism for hydrolysis of the methyl phosphate anion (see figure 3.5) [Hu and Brinck, 1999].

We have shown that solvent molecules play an active role during base-catalyzed hydrolysis of carboxylic esters.

On the other hand, we found the associative mechanism of this reaction to proceed without explicit involvement of solvent molecules, due to steric restrictions. The lack of water-assisted proton transfer in this mechanism makes it energetically disfavored compared to the dissociative mechanism. This observation is expected to be important in relation to understanding the mechanisms for phosphate hydrolysis also in enzymes and other biolog-

ical systems.

In addition to the studies of natural enzyme reactions, we have begun investigating catalysis in site-mutated enzymes. In particular, we are studying a serine hydrolase (Candida antarctica lipase B [CALB]) in which the catalytic serine residue has been replaced by a non-polar residue (glycine or alanine). It has been proposed that this modified enzyme might catalyze a number of unnatural reactions. Our initial studies indicate that the enzyme can catalyze the Bayer-Villiger reaction. Quantum chemical calculations on model systems show that the enzyme active site has an influence on the potential energy surface of the reaction similar to the frequently used catalyst boron trifluoride.

Recent studies have shown that proteins may not only be susceptible to oxidation by oxidative radicals at easily oxidized side chains—such as tyrosine, cysteine, and phenyl alanine—but also at the protein backbone, because the alpha-C-H bond dissociation energies are relatively low. The peptide radicals thus formed may react with molecular oxygen to form a peroxyl radical, or form a peptide cation and superoxide through an electron transfer mechanism. If the former pathway dominates, the result could be a chain reaction; this is because the peroxyl radical can abstract a hydrogen atom from a nearby peptide chain, which results in a new peptide radical. The relative distribution between the two pathways is expected to be largely dependent upon substituent effects and solvent effects.

We have used quantum chemical methods to analyze the thermochemical properties of substituted alkyl and peroxyl radicals [Brinck *et al.*, 1999]. In particular, we have studied compounds that can serve as models for peptide and peptide peroxyl radicals (see figure 3.6). In addition to the thermodynamical analysis of the proposed reaction pathways, we have also calculated the relevant transition states in order to estimate rate constants. Our analysis indicates that the peroxyl radical pathway is likely to dominate in the interior of a protein, while the electron transfer pathway may dominate at the solvated protein surface.

The presented research has largely been carried out using computers at PDC. The parallel IBM SP machine Strindberg has been found to be very well suited for molecular geometry optimizations employing Hartree-Fock and density functional theory (DFT) methods. For advanced post Hartree-Fock methods, such as cou-
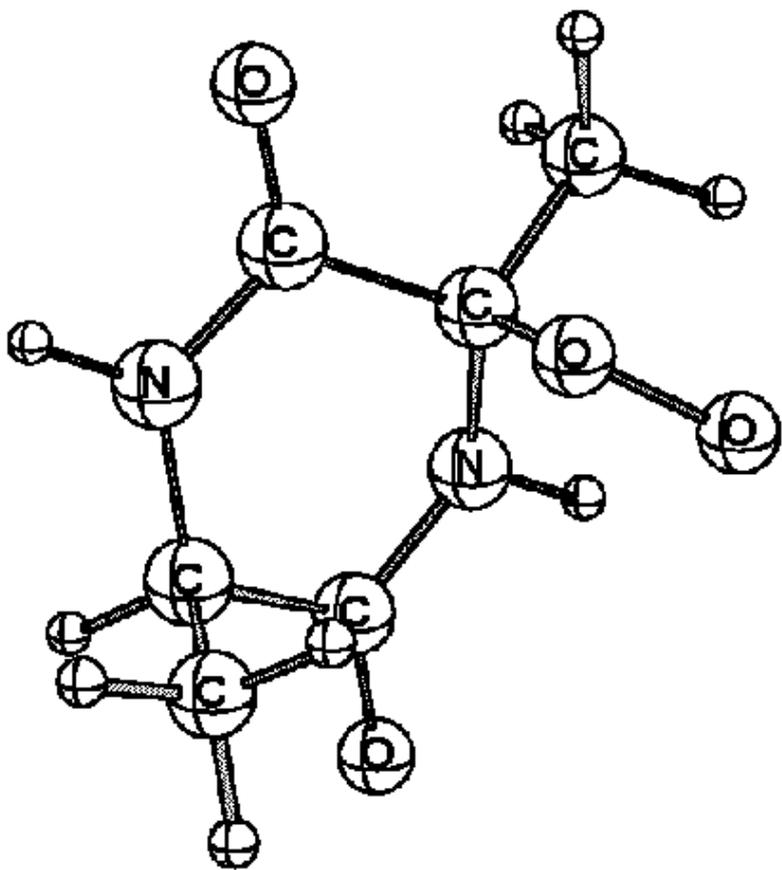
Figure 3.6. The DFT-B3LYP/6-31G** optimized geometry of a model system used to study protein oxidation.

pled cluster techniques, we have found the CRAY J932 computer named Kallsup to be the best choice, due mainly to its large memory bandwidth. In conclusion, the presented projects have benefited tremendously by the access to resources at PDC.

4 Chemistry

4.1 First-Principles Studies of Mica

Michael Odelius
Department of Physical Chemistry, Uppsala University

First-Principles Molecular Dynamics Simulations

I have studied hydrogen bonding in systems in which the accuracy or conceptual framework of classical molecular dynamics (MD) simulations is insufficient.

The first-principles molecular dynamics method, based on density functional theory (DFT), gives the unique opportunity to combine high accuracy and large systems. Structure, dynamics, energetics, and electronic properties are contained within the first-principles MD simulation.

In order to study reactions in condensed phases, it is necessary to employ a description of the reactive groups with "chemical" accuracy and to include a sufficiently large surrounding to account for the solvation. If the size or accuracy is reduced to enable studies on smaller computers, the results become unreliable, and the whole purpose of the calculations is lost.

The calculations including up to 160 atoms have been run on 30 and 60 nodes of the IBM SP using 30,000 node-hours.

The first-principles MD method gives the opportunity to combine high accuracy and large systems.

Dehydroxylation of Muscovite

Mica ($2M_1$-Muscovite) is a layered silicate structure of tetrahedral SiO_4 (with substitutions of AlO_4) units and octahedral AlO_6 units connected in separate sheets. The structure also contains potassium ions and protons. The protons form hydroxyl groups with oxygens in the octahedral layer. Upon heating, $2M_1$-Muscovite dehydroxylates (*i.e.,*, the hydroxyl groups) react with each other to form water and O^{-2}, and a phase transition to a dehydroxylated form of $2M_1$-Muscovite occurs.

The dehydroxylation of $2M_1$-Muscovite and other mica have been carefully studied by many different experimental techniques, which have been successful in determining the differences between the $2M_1$-Muscovite crystal and its dehydroxylated form. However,

Figure 4.1. Hydroxyl groups in muscovite react to form water, which initiates the phase transition to the dehydroxylated mica. In first principles molecular dynamics simulations at elevated temperatures, the dynamics indicated that the reorientational motion of the hydroxyl groups is responsible for the reaction. This was corroborated by geometry optimizations, in which it was found that the reaction of hydroxyl groups connected to the same Al^{3+} (in cis-position) is energetically favorable to the reaction in trans-position.
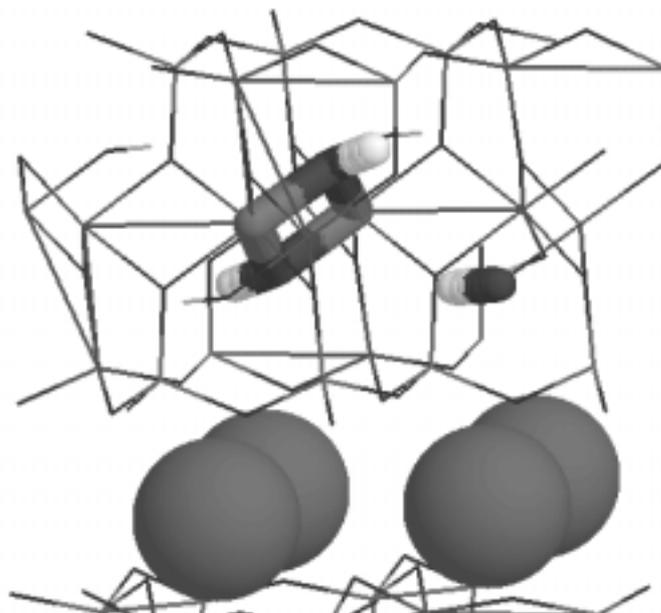
the detailed mechanism for the reaction is difficult to reach from the experimental data, which motivates a theoretical study.

The quality of the method was confirmed by optimizations of the crystal structure [Odelius *et al.*, 1997a]. Short MD simulations at different temperatures (300–1500 K) did not result in any spontaneous reaction, but at elevated temperatures the motion of the hydroxyl groups increased significantly. In particular, high amplitude reorientational modes of the hydroxyl groups and large deviations in the $Al - OH$ distances arise at the phase transition temperature. Through geometry optimizations, the water formation was studied. In combination with the MD simulations, a model for the dehydroxylation was formulated [Odelius, 1999]. The reaction of hydroxyl groups in cis-position is favored over those in trans-position (see figure 4.1), in agreement with conclusions from the dynamic analysis.

Proton Diffusion of Mica

In the $2M_1$-Muscovite crystal, bitrigonal rings in the silicate layers sandwich potassium ions. Mica is easily cleaved along the potassium ions and forms a molecularly smooth surface, which is used as an experimental model system and for support of adsorbants,

such as proteins and ions.

In previous work [Odelius *et al.*, 1997b], we have studied the hydration of the mica surface, its effect on the potassium ions, and the formation of a "2D-Ice" at monolayer coverage.

Because neither the potassium ions nor the proton are visible in atomic force microscopy (AFM) images, calculations of the clean mica surface with K^+ exchanged for different ions (Li^+, Na^+, and Mg^{2+}) were performed. In perfect agreement with AFM experiments, the Li^+ and Mg^{2+} ions reside in the rings in the plane of basal oxygens. In contrast, the potassium ions reside $1.4\,Å$ above the rings, only slightly displaced ($0.11\,Å$) towards the surface after cleavage [Odelius *et al.*, 1997b]. Sodium ions have intermediate size, and they behaved similarly to the potassium ions.

On the wet mica surface [Odelius *et al.*, 1997b], hydration pulls the potassium ions out $0.47\,Å$ from the surface, which has been argued to make them mobile and invisible to the AFM tip. The hydration forces would be insufficient to pull up the Li^+ and Mg^{2+} ions from the rings.

The mica surface has a high affinity for protons, which thus will influence surface phenomena on the mica surface. The solvation and diffusion of protons in bulk water is well understood. The situation on the mica surface, upon which the proton diffusion is restricted to two dimensions, is less clear.

Water adsorbs molecularly off the K^+-mica surface [Odelius *et al.*, 1997b]. Protons, on the other hand, hydroxylate the surface and bind highly preferentially to AlO_4 tetrahedra. An oxonium H_3O^+ ion on the surface undergoes barrier-free dissociation into a water hydrogen bound to basal oxygens and to a hydroxyl group on the surface.

In MD simulations in the presence of more water, there was a balance between oxonium H_3O^+ ions and surface hydroxyl groups, and proton transfer occurred. The proton jumping between different AlO_4 tetrahedra was mediated by the water molecules (see figure 5.4 on page 60).

4.2 Metal Clusters and Surfaces: DFT-Based Molecular Dynamics

Henrik Grönbeck, Alessandro Curioni, Wanda Andreoni
IBM Research Division, Zurich Research Laboratory, Switzerland

In our research program at PDC we apply density functional theory (DFT) [Hohenberg and Kohn, 1964, Kohn and Sham, 1965] and the Car-Parrinello method [Car and Parrinello, 1985] for *ab initio* molecular dynamics to problems in the area of atomic clusters and molecular adsorption on surfaces. The computational approach uses pseudopotentials to describe the interaction between the valence electrons and the inner core together with plane waves for the expansion of the electronic wave functions[1]. The size and accuracy of the calculations performed require the use of parallel computers, and the IBM SP resources have been vital for the realization of our projects. Moreover, we have benefited from the large storage capacities available at PDC.

Generation and Tests of Pseudopotentials

In all our calculations, the first step is the construction and test of the pseudopotentials. To generate them, we have generally been using the scheme according to Troullier and Martins [Troullier and Martins, 1992]. It is well known that relativistic effects are of crucial importance in the description of the physical and chemical properties of heavy elements such as gold. In the computational method we use, the spin-orbit coupling is neglected and the relativistic effects are accounted for by the use of a pseudopotential obtained from scalar relativistic all-electron calculations. The frozen core is Au^{11+} for gold and Pt^{18+} for platinum.

Metal Clusters

Computational methods based on DFT have proven important for understanding the evolution of the structural and electronic properties of metal clusters.

The study of atomic clusters is interesting because the clusters constitute a phase of matter for which valuable comparisons between *ab initio* calculations and highly accurate measurements have become possible. Especially computational methods based on DFT have proven important for understanding the evolution of the structural and electronic properties of metal clusters[Ballone

---

[1]We used the CPMD code, Version 2.5 (Copyright IBM Corporation) and Version 3.0 (Copyright IBM Corporation and MPI, Stuttgart).

Method	a (Å)	E_c (eV)	B (MBar)
LDA	4.06	4.43	2.02
BP	4.18	2.96	1.44
BLYP	4.24	2.38	1.14
PBE	4.15	3.15	1.56
Exp.	4.07	3.81	1.72

Table 4.1. Calculated bulk properties for fcc Au.

and Andreoni, 1999]. In 1998, we published an extension of our earlier work on neutral niobium clusters [Grönbeck *et al.*, 1997] to positively and negatively charged clusters [Grönbeck *et al.*, 1998]. Our work was motivated by the recent availability of photoelectron spectra on size-selected anionic Nb clusters [Kietzmann *et al.*, 1998]. We have also calculated the electronic and structural properties of neutral and anionic Au and Pt clusters, for which comparison with experiments on the electronic structure is possible. Our results provide information on the structural growth and the bond characteristics; and the calculated values for vertical detachment energies compare well with the experimental data.

Metal Bulk

Calculations of the structural properties and energetics of the bulk phase of Au, Pt, and Nb have been performed with the aim of verifying the performance of various exchange correlation functionals. The calculations are at convergence with respect to k-point sampling of the Brillouin zone. The functionals we investigated are the local density approximation (LDA) [Perdew and Zunge, 1981, Ceperley and Adler, 1980] and other functionals that include gradient corrections, namely, BLYP [Becke, 1988, Lee *et al.*, 1988], BP [Becke, 1988, Perdew, 1986], and PBE [Perdew *et al.*, 1996]. We find important differences in the computed values of the lattice constant (a), the cohesive energy (E_c), and the bulk modulus (B). In Table 4.1 this is exemplified by our results for Au.

$Au_{38}(SCH_3)_{24}$

Recent experimental advances have been made in fabricating crystalline molecular solids of passivated Au clusters [Whetten *et al.*, 1996]. These systems, which exhibit novel electronic properties, are proposed to consist of a crystalline Au core surrounded by

Figure 4.2. The computed DOS for an Au(111) slab using the PBE functional. The zero energy is the computed Fermi energy. The arrows indicate the surface states discussed in the text.
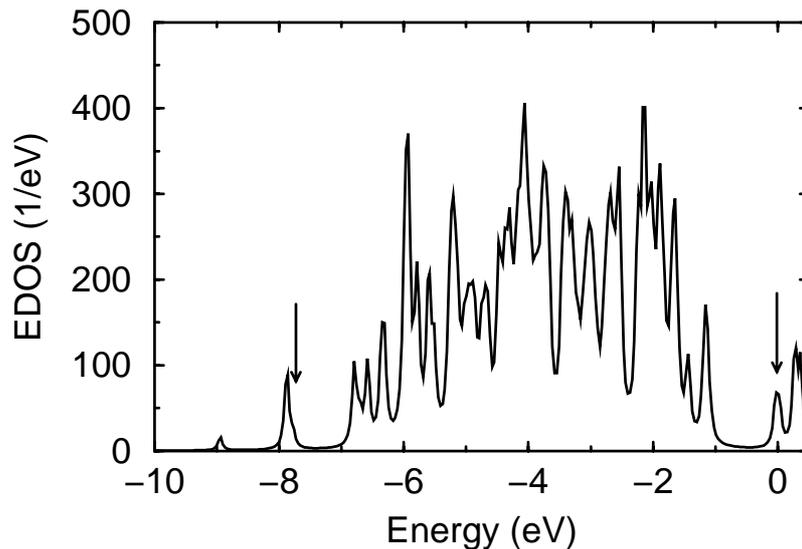
chemisorbed thiolates $(S - (CH_2)_n CH_3)$. The smallest passivated cluster observed so far consists of 38 Au atoms and 24 thiolates. The Au core has tentatively been proposed to have the structure of a truncated octahedron. We have studied $Au_38(SCH_3)_{24}$ starting from the proposed core structure. Further relaxation, however, showed unambiguously that this is a thermodynamically unstable atomic configuration.

Au(111) Surface

Calculations were performed on a slab with periodic boundary conditions. Tests were done with respect to system size. The final model we assume is one with four atomic layers, each consisting of 25 atoms (a 5×5 supercell). For this supercell, only the $k = 0$ point is used as representative of the Brillouin zone. It is known from experiments, in particular from angle-resolved photoemission [Kevan and Gaylord, 1987], that the Au(111) surface exhibits two characteristic intrinsic surface states with *sp* character. One appears at binding energies $\sim 7.8\,\text{eV}$, and another is located close to the Fermi level. Figure 4.2 shows our results for the electronic density of states (DOS). The qualitative agreement with experiments is good.

Adsorption on Au(111)

Alkyl sulfides adsorbed onto Au(111) are a prototype system for self-assembled monolayers (SAMs) [Ulman, 1996]. Despite the fact that the experimental research on SAMs has been intense in the past 15 years, several open questions still remain, for example, regarding the nature of the sulfur-metal bond. In fact, no consensus has been reached on the adsorption state. Using different exchange correlation functionals, we are currently investigating these problems using methyl sulfides as adsorbates.

4.3 Molecular Dynamics Simulation of Ion Mobility in the Polymer/Inorganic Interface

Alvo Aabloo
Institute of Materials Science, Tartu University, Estonia
Mattias Klintenberg, Josh O. Thomas
Inorganic Chemistry Department, Angstrom Laboratory,
Uppsala University

In endeavoring to optimize the design of the Li-ion polymer battery (the current state-of-the-art in cellular phone batteries), much fundamental understanding is lacking in our efforts to reach a balanced compromise between the requirements of individually appropriate electrode and electrolyte materials. We therefore turn to a molecular dynamics (MD) simulation approach to establish an initial basic understanding of structural and dynamical aspects of the inorganic electrode/polymer-electrolyte interface region, as well as an understanding of how ions move in such a region.

Earlier work has confirmed the simple textbook picture of an ion moving through the archetypal poly(ethylene oxide) [PEO] polymer host, while maintaining its coordination to the ether oxygens. Successful MD simulations have also been made of an amorphous PEO surface, as well as of the surface of a V_2O_5 cathode material. It is thus very natural that our next step should be to attempt to model the most primitive of electrode/electrolyte interfaces involving these same component materials, and the motion of simple lithium-salt ions therein.

The amorphous PEO model has been achieved through the initial use of periodic Monte Carlo (MC) simulation. A chain of 200 EO units (each $-CH_2 - CH_2 - O-$) is created in a simulation box of dimensions $28 \times 23 \times 37$ Å; the x- and y-direction edge-

lengths are chosen to match to $2a \times 8b$ on the ab-basal plane of V_2O_5. The V_2O_5 slab model reproduces the amorphous sol-gel synthesized phase known to contain a double-layer of corner- and edge-shared VO5 pyramids; the simulation box also contains 32 V_2O_5 units; in total: 1,848 atoms + two extra H atoms to convert CH_2 groups to chain-terminating methyl groups; 22 lithium and 22 chlorine ions were later added randomly and their behavior was monitored.

The content of the MD simulation box was first allowed to equilibrate (150 ps) to a target temperature of 400 K. MD simulation in an NVT ensemble mode was then run for 300 ps, followed by 1,000 ps in the final NpT ensemble mode. The simulation step-time throughout was 0.5 fs. The final 800 ps of NpT-mode simulation was sampled every 1,000 steps. The potentials used have been described [Neyertz *et al.*, 1995, Linde and Thomas, 1996]. An Ewald summation routine was included in the algorithm. The calculations used a local version of the polymer simulation program DL_POLY 2.1 [Smith and Forester, 1999].

A typical snapshot of the simulated model during the final "sampled" stages of the simulation is shown in figure 5.5 on page 61. The major feature that emerges from an analysis of the simulations is that the dynamics of both the PEO and V_2O_5 in the interface region (as represented by the motion of the ether oxygens and the outermost V = O vanadyl bonds) is significantly lower than in the bulk. A stable, non-periodic, disordered structure would appear to form on both sides of the interface. It is especially significant to note that Li-Cl ion pairs form in the pseudo-bulk of the layers, and not at all in the interface region. This has major electrochemical implications.

Because fundamental experimental data on the structural nature of the polymer-inorganic interface at the atomic level is scarce (not to say non-existent), molecular dynamics simulation can give the first suggestive insights into how an idealized interface of this type can behave. Moreover, the calculations are of such a magnitude that they necessitate a machine the size of the IBM SP.

Li-Cl ion pairs form in the pseudo-bulk of the layers, and not at all in the interface region.

4.4 Quantum Chemical Calculations of EPR Parameters

Maria Engström
Department of Physics and Measurement Technology,
Linköping University

By using Electron Paramagnetic Resonance (EPR), the structure and dynamics of radicals and their interactions with surrounding molecules can be investigated. The EPR spectra are commonly interpreted from simulations, where experimental results are matched with parameters in the theoretical energy expression. These parameters are sensitive probes of the environment and geometry of the radicals. Owing to the radicals' short lifetime, experimental interpretations are sometimes ambiguous. Quantum chemical calculations may therefore provide further information. The objective of the present project is to calculate the g-tensor and the hyperfine coupling constants (hfcc) with quantum chemical methods and to make applications to radicals in biomolecular systems.

The objective is to calculate the g-tensor and the hyperfine coupling constants, and to make applications to radicals in biomolecular systems.

Substituted Benzene Radicals

The g-values for several substituted benzene radicals were calculated in order to test the range of validity of ROHF reference states [Engström *et al.*, 1999b]. Calculated g-values were in excellent agreement with experiments for six out of nine radicals. Two radicals showed minor discrepancies, while the g-tensor of the phenoxyl radical was incorrect. The problem with the phenoxyl radical was traced to a complex electronic structure. Results consistent with experiments could in that case be obtained with electron-correlated calculations.

Tyrosyl Radical

Tyrosyl is a stable radical in several enzymes, such as ribonucleotide reductase (RNR) and galactose oxidase (GO). A relatively large g-tensor anisotropy of the component directed along the CO bond of the tyrosyl ring, g_x, is detected by EPR. Hydrogen bonding to the tyrosyl radical was simulated by a complex between the phenoxyl radical and a water molecule [Engström *et al.*, 2000b]. The calculated g-tensors reproduced the anisotropy of the tyrosyl radical as well as the shift of g_x towards lower values upon hydrogen bonding that was observed experimentally in RNR.

The tyrosyl radical in GO is covalently cross-linked to a neighboring cysteine residue through a thioether bond. The g-tensors of unsubstituted and thioether substituted phenoxyl radicals were calculated [Engström *et al.*, 2000a]. In contrast to some previous interpretations, but in agreement with recent EPR measurements, we found that the sulfur substitution induces only minor shifts in the g-tensor components. The spin distribution retained the odd-alternant pattern of the unsubstituted radical, and only a small amount of spin was localized to the sulfur center.

Sulfur-Centered Radicals

The EPR parameters of sulfur-centered radicals differ depending on the radical structure and charging. Especially, the g-tensor components provide significant patterns that may distinguish radical structures from each other. The g-tensor and hfcc were calculated for monosulfide radicals (RS·), disulfide radicals (RSS·), radical cations (RS·SR$^+$) and anions (RS·SR$^-$) with results in agreement with experimental data [Engström *et al.*, 2000]. Particularly, the assignment of the disulfide anion in RNR was confirmed. The results indicate that investigations with the present computational methods might provide interpretations of experimental data on unassigned radical species.

Investigations with the present computational methods might provide interpretations of experimental data on unassigned radical species.

Nitroxide Spin Labels

Nitroxide radicals are used as spin-probes to study protein interactions. The objective of this project is to experimentally and theoretically investigate how different molecular environments influence the EPR parameters. The Self Consistent Reaction Field Polarizable Continuum Model (SCRF-PCM) was used to calculate the hyperfine couplings constants and geometry of the spin labels in solvents of different polarity [Engström *et al.*, 1999a]. Further, the hfcc as well as the g-tensors were calculated for different geometrical structures and hydrogen-bonding models. The results indicate that the hfcc varies nonlinearly with solvent polarity. The component along the NO bond, g_x, decreased with hydrogen bonding while A_z increased upon hydrogen bonding, in agreement with experimental findings.

The *g*-tensors were calculated with the linear response method with ROHF and MCSCF reference states implemented in a local version of the DALTON quantum chemistry program [Helgaker and *et al.*, 1997]. The hyperfine coupling constants were calculated with the DFT/B3LYP method in Gaussian 98 [Frisch and *et al.*, 1998]. The calculations were performed on the Strindberg IBM SP. Calculations of spin-orbit coupling integrals (necessary for the *g*-tensor calculations) demand large disc space and are time consuming for large molecular systems. For this reason, the present research projects could not be accomplished without access to PDC resources.

An example of (1-oxyl-2,2,5,5-tetramethylpyrroline-3-methyl) methanethiosulfonate spin label (MTSSL) can be seen in figure 5.6 on page 61.

4.5 Quantum Chemical Molecular Modeling for Development of New Palladium and Ruthenium Catalyzed Transformations

Kálmán J. Szabó
Arrhenius Laboratory, Department of Organic Chemistry,
Stockholm University

This project has focused on substituent and ligand effects on the reactivity of palladium and ruthenium intermediates of synthetically important transformations, such as palladium catalyzed oxidation reactions and ruthenium catalyzed hydride transfer processes [Szabo, 1988, Aranyos *et al.*, 1998, Szabo *et al.*, 1998, Szabo, 1998, Aranyos *et al.*, 1999].

Because alteration of the coordinated ligands is frequently used for fine tuning the reactivity and for increasing the selectivity in transition metal catalyzed reactions, a fundamental understanding of the ligand effects on transition metal reactivity is a prerequisite for designing new catalytic procedures. One of the most interesting results from this project was obtained in 1998 by investigating the *cis* migration aptitude of the chloride ligand in (η^3-allyl)palladium complexes [Szabo, 1998].

The migration of chloride (see figure 4.3) is particularly difficult to accomplish using standard activating ligands, such as phosphines or the commonly used benzoquinone derivatives, because

Figure 4.3. The migration of chloride.

Chloro-complex   TS   Product
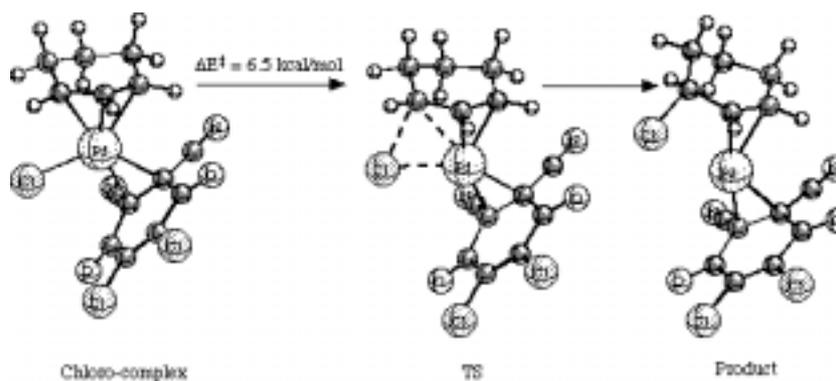
the chloride ligand has a large coordination affinity to palladium. Studies in high-level quantum chemistry (B3PW91/LANL2DZ+P) have shown, however, that the activation barrier to the ligand migration can be decreased by employing non-bulky electron-withdrawing substituents on benzoquinone. The lowest activation barrier was encountered for an $[\eta^3\text{-}(1,2,3)\text{-cyclohexenyl}]$palladium complex coordinated to 2,3-dichloro-5,6-dicyanobenzoquinone (DDQ). Experimental studies verified that in such complexes, chloride migration is feasible, resulting in stereodefined 3-chlorocyclohexene products.

4.6 Quantum Chemistry as a Tool in Organometallic Chemistry

Peter Brandt
Department of Medicinal Chemistry, Royal Danish School of Pharmacy
Pher G. Andersson
Department of Organic Chemistry, Uppsala University

Dialkylzinc Additions to N-(Diphenylphosphinoyl) Benzalimine

Chiral amine derivatives are of ultimate importance in both catalytic asymmetric synthesis and in medicinal chemistry. One way to synthesize these compounds is by the addition of organozinc reagents to prochiral imines. Although several more or less enantioselective reactions have been developed recently, both the mechanism and the selectivity process have remained unclear. In one of our projects performed with support from PDC, we decided to uncover these facts by a combined quantum chemical and experimental approach [Brandt *et al.*, 1999]. The large size of the molecules

and the many diastereomeric TSs that had to be analyzed in order to understand the selectivity process required computer resources beyond our own facilities.

Mechanistically, this reaction bears some resemblance to the analogous addition of dialkylzinc reagents to aldehydes. However, as the calculations have shown, a new view of the mechanism has to be considered in the imine reaction. Based on this new knowledge, the enantioselectivity of the reaction can be understood and future design of better ligands can be facilitated. Two illustrative diastereomeric TSs of the new mechanism are shown in figure 4.4. The results from this investigation will be used in future design of faster and more selective systems.

Ruthenium-Catalyzed Transfer Hydrogenation of Aromatic Ketones

Reductions of unsaturated systems occupies a large field of organic synthesis, and especially asymmetric hydrogenations are currently being intensely studied. One very attractive way of reducing ketones is to use cheep i-propanol as both solvent and reductant. This reaction, catalyzed by chiral ruthenium complexes with aminoalcohol and arene ligands, has experienced a rapid development during the last few years. In order to understand how the rate of the reaction could be increased and to rationalize the enantioselectivity of the reaction, we investigated this reaction by means of quantum chemical calculations [Alonso *et al.*, 1998]. See figure 4.5.

The reaction was found to take place via a concerted process where both a hydride and a proton are transferred simultaneously to the ketone from a ruthenium hydride intermediate with a coordinated primary or secondary amine (figure 4.6). By the comprehensive knowledge of the mechanism, we have been able to explain both how the rate and the selectivity are influenced by structural elements of the ligand. Most importantly, this investigation has a direct influence on the development of new catalysts in our lab.

Figure 4.4. The two lowest diastereomeric transition states for the addition of dimethylzinc to N-(dimetylphosphinoyl) benzalimine (B3PW91/(6-311+G,6-31G)).
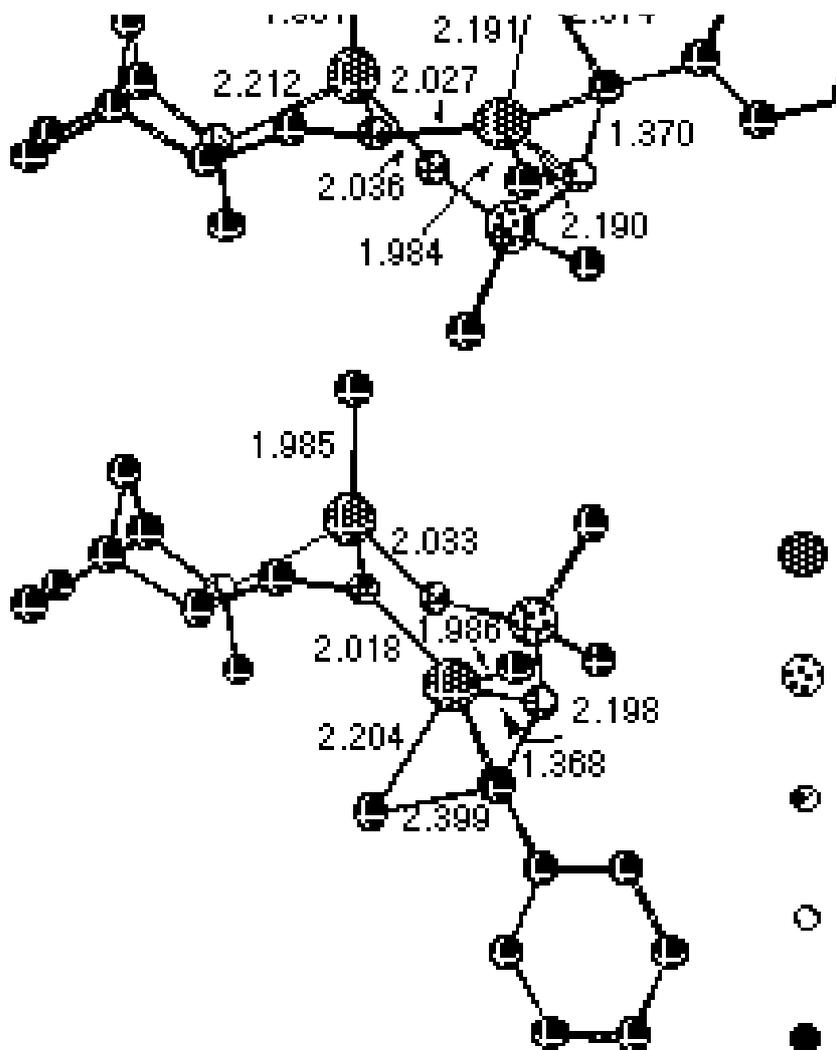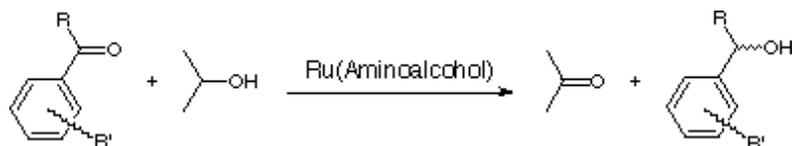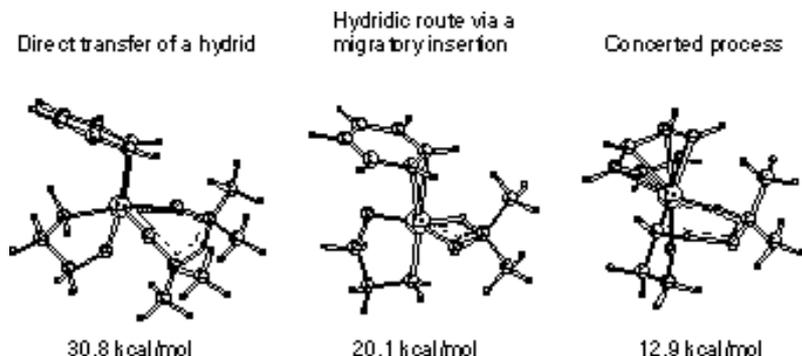
Figure 4.5. Reaction scheme.

Direct transfer of a hydrid   Hydridic route via a migratory insertion   Concerted process

30.8 kcal/mol   20.1 kcal/mol   12.9 kcal/mol

Figure 4.6. Three different TSs evaluated for the ruthenium-catalyzed transfer hydrogenation of ketones (B3PW91/(SDD(f),6-311+G**)//B3PW91/LANL2DZ).

4.7 Structure in Charged Colloidal Systems

Vladimir Lobaskin, Per Linse
Department of Chemistry and Chemical Engineering,
Lund University

Introduction

Theoretical studies of highly charged colloidal systems possess several challenging aspects. Two of them are the long-range Coulomb interaction and the existence of spatial correlations among the charged species on different length scales. Such studies are of utmost importance, because such colloids appear in everyday life in detergents and dyes, in drug delivery systems, in flotation, and not least in biological systems.

Our aim is to perform numerical simulations of highly charged colloidal solutions employing the so-called two-component model. In this model, the charged colloidal particles (referred to here as macroions) and the small counterions (referred to here as ions) enter the model on an equal level, and all charged species interact through a Coulomb potential screened by the dielectric permittivity of the solvent. Besides giving new physical insights, our results are of great value for assessing the accuracy of (i) simpler theories, such as the classical Derjaguin-Landau-Verway-Overbeek (DLVO) theory, and (ii) simpler statistical mechanical theories, such as liquid state theories.

Our aim is to perform numerical simulations of highly charged colloidal solutions employing the two-component model.

Methodological Improvements

The Ewald summation technique is a very accurate method to handle the long-range interactions in liquid systems of charged

species. During 1998, we compared results using the Ewald summation with results from other methods for systems with a charge asymmetry of 20:1 (*e.g.*, a macroion with 20 elementary charges and monovalent counterions), and we obtained very good agreement [Lobaskin and Linse, 1998a]. We have established that the Ewald summation is appropriate to use for modeling charged colloidal solutions.

We have also devoted substantial effort to examining the efficiency of molecular dynamics (MD) and Monte Carlo (MC) simulations of charged colloidal systems. We concluded that simulations of systems with charge asymmetry much larger than 60:1 would essentially be impossible, even with very extended computer resources [Linse, 1999]. The problem is the large buildup of small ions close to the surface of the colloidal particles (as illustrated in figure 4.7b), and this buildup impedes the movement of the macroions. This is a real physical effect, of course, but it still constitutes a major problem for performing such simulations. To avoid this difficulty, we have implemented a new MC simulation technique, where cluster moves are performed [Lobaskin and Linse, 1998b]. In essence, the macroion and its closest ions are moved together. However, some care has to be taken to fulfill microscopic reversibility, and hence to retain the Boltzmann statistics.

Structure in Colloidal Solutions

We have performed extensive simulations of a system composed of macroions with 60 elementary charges mimicking surfactant micelles formed by dodecyl sulfate in aqueous solution also containing monovalent ions [Lobaskin and Linse, 1998b]. Two short-range potentials have been applied: a hard-sphere and a soft-sphere potential. The former one is most often employed in theory, whereas the latter one is probably more appropriate for describing experimental systems.

Figure 4.8 displays a snapshot taken at the end of a simulation, and it illustrates the spatial arrangements in such systems. We see an accumulation of the ions around the macroions, which are separated from each other.

Quantitatively, the structures are usually characterized by radial distribution functions, $g(r)$, which express the relative density of a particle of the same or different type at some distance r from a given particle. Figure 4.7 displays the three distinct $g(r)$s for
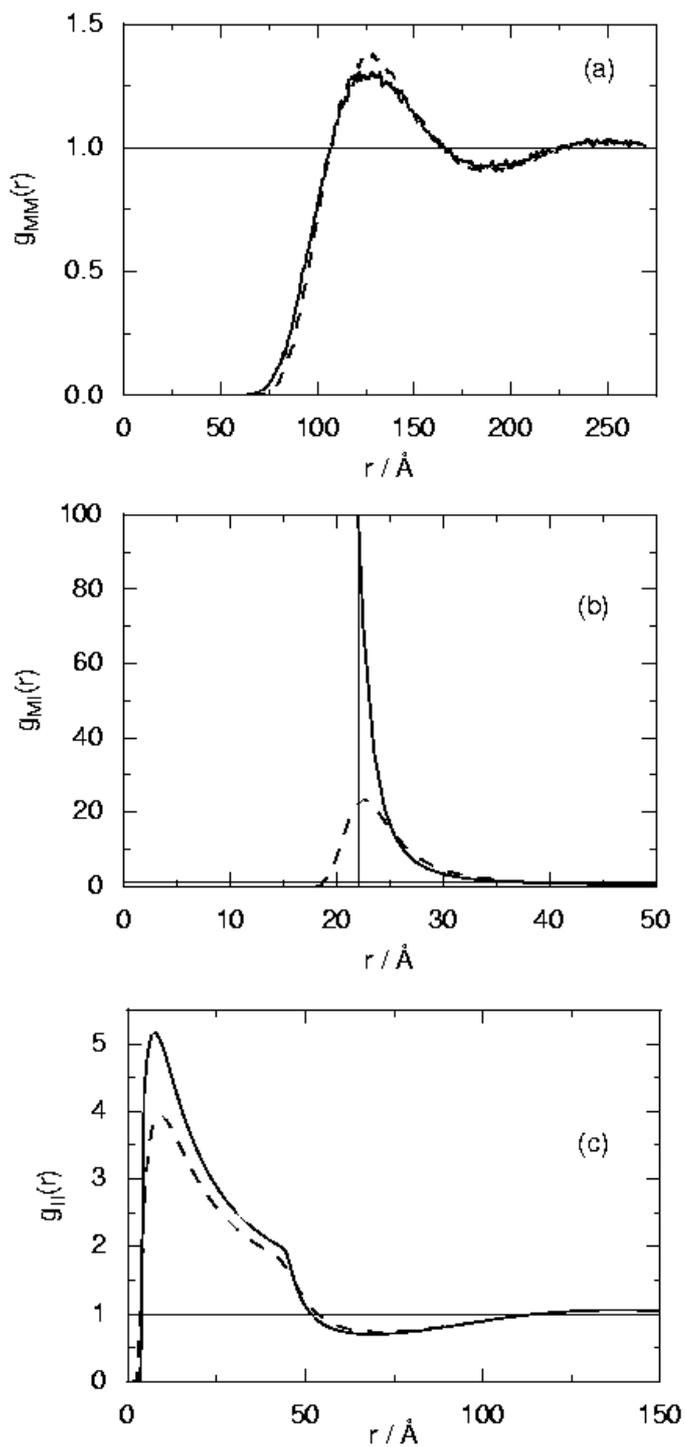
Figure 4.7. (a) Macroion-macroion, (b) macroion-ion, and (c) ion-ion radial distribution function for the 60:1 system for the hard-sphere (solid curves) and the soft-sphere (dashed curves) models from simulations with 80 macroions and 4800 ions. Other conditions as in figure 4.8. Thin solid lines denote homogeneous distributions (no spatial correlations). Note the different scales of the r- and g-axes.

Figure 4.8. A snapshot of the primary box for the 60:1 system with 80 macroions and 4,800 ions illustrating the separated macroions and the accumulation of the ions in the neighborhood of the macroions. Periodical boundary conditions are applied. Macroion radius $= 20\,\text{Å}$, ion radius $= 2\,\text{Å}$, macroion volume density $= 1.67\,\%$, temperature $= 298\,\text{K}$, and relative dielectric permittivity $= 78.3$
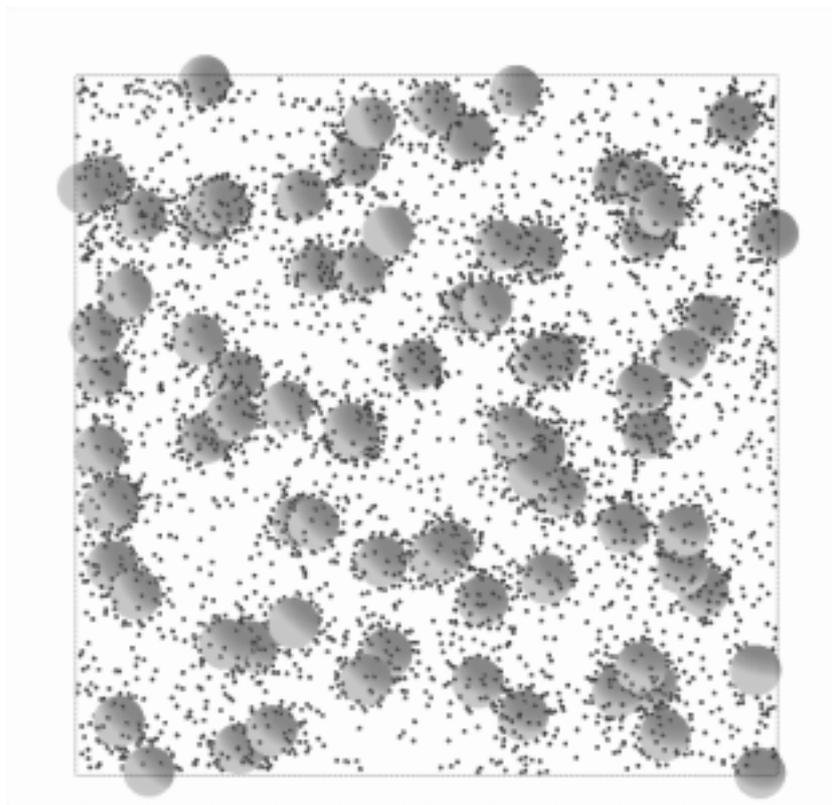
the 60:1 system for the two short-range potentials. Independent of the short-range potential, the g_{MM} in figure 4.7a verifies that the macroions are indeed well separated and form a liquid characterized by short-range order but long-range disorder. The closest macroion-macroion separation is about 70 Å, which should be compared to the contact separation of 40 Å. The repulsive interaction among the macroions typically creates an effective repulsion (when averaged over the small ions) among the macroions, as shown here. The strong accumulation of the ions to the macroions mentioned above is clearly visible by the large peak in g_{MI} at 22 Å in figure 4.7b.

Finally, the ion-ion radial distribution function displays a positive correlation in the range 5–50 Å due to the combined effect of the repulsion among the macroions and the attraction between the ions and the macroions. Thus, figure 4.7 more firmly illustrates the richness of different types of spatial correlations appearing on different length scales that exist in charged colloidal systems.

We can also make a comparison between the two short-range potentials. From g_{MM}, we infer that the macroion structure is slightly more pronounced in the case of the soft-sphere potential. This behavior is consistent with the larger accumulation of the small ions close to the macroion displayed by g_{MI} and indirectly inferred from g_{II} (a larger number of ions close to the surface of a macroion). Hence, the so-called electrostatic screening differs between the two models.

In our work, we have been benefitted from using Strindberg at PDC for parallel MD simulations and (not yet parallelized) MC simulations. This has been a necessary extension to our local computer capacity.

4.8 Surface and Gas Phase Reactions during Film Growth

Karin Larsson
Inorganic Chemistry Department, Angstrom Laboratory,
Uppsala University

Thin films of various materials play an important role in materials sciences today. A combination of suitable, cheaper, and less demanding bulk materials with functional thin-film coatings would offer an ideal solution to the problems with material choice in a

wide number of applications. However, there might be severe difficulties in the fabrication of various materials. For instance, there are often problems with heteroepitaxial growth of one material on another material. In order to succeed in a well-controlled growth of materials, we must have detailed understanding at the molecular level of the growth processes. This can be achieved, at least in part, by performing quantum mechanical calculations.

Vapor growth of materials is a very dynamic process, because it involves the generation of surface vacancies and adsorption of different gaseous species (including the growth species) to various radical surface sites. Adsorption processes are, therefore, of particular importance to investigate. These adsorbed species must not, however, be too strongly adsorbed to the surface. For example, growth precursors have to be mobile. Hence, other interesting growth processes should include surface abstraction and migration, as well as nucleation and a continued lateral growth process. The effect of different experimental parameters on these growth processes has been focused within the present project. These parameters will include temperature, gas phase-content, and degree of purity of the substrate. Reduction of the substrate temperature is strongly desired for growth of, for example, diamond, c-BN, or SiC on materials that cannot tolerate high temperatures.

Different types of surface reactions occurring during the growth of diamond, c-BN, and different allotropes of SiC were simulated theoretically at PDC during 1998. There are important industrial and technical applications for these compounds. This is mainly due to their extraordinary chemical and physical properties (*e.g.*, extreme hardness, high thermal conductivity and electric resistivity, large band gap, chemical inertness), which are very similar. The most striking dissimilarity is the fact that reproducible thin film growth of diamond and silicon carbide can be rather easily obtained, while there are problems in the current CVD-synthesis of c-BN.

Adsorption, abstraction, and surface migration were investigated thoroughly.

The different surface processes investigated thoroughly were adsorption, abstraction, and surface migration. The aims were first, to get a deep knowledge of the general growth processes for each compound; and second, to compare these growth processes. Total energies and geometrical structures were then calculated by using the *ab initio* MO method (HF and MP-2) within the Gaussian 92 package. Moreover, potential-energy surfaces (PES) and

transition states (TS) were calculated for the migration reactions. An estimate of the barrier of energy can be obtained from the PES and the TS. This barrier is generally regarded as a measure of the driving force of the specific reaction studied. Information can therefore be obtained about the tendency for the migration process to occur on the different surfaces. In addition, electron densities and an estimation of atomic charges were studied for the adsorption reactions, which can be regarded as electron-transfer (partial) reactions.

It was extremely important to use computer resources at PDC during 1998 for the calculations described above. It would be far too time-consuming for us to use the required large templates, in addition to the more sophisticated basis sets, on ordinary workstations. Further, it is impossible for us to perform electron correlation corrections on these types of calculations with the workstations at our department, because of the large amounts of memory and disk space needed. The present project is, hence, totally dependent on access to supercomputers, such as the Fujitsu VX/3, at PDC in Stockholm. Fortunately, we were able to perform calculations at the HF level, as well as at the MP-2 level, of theory on this computer during 1998 [Larsson and Carlsson, 1999b, Larsson and Carlsson, 1999a, Larsson and Carlsson, 1998a, Larsson and Carlsson, 1999c, Larsson and Carlsson, 1998b].

4.9 Theoretical Studies of the Structure and Function of Metal Proteins

Ulf Ryde, Mats H. M. Olsson, Emma Sigfridsson, Björn O. Roos
Department of Theoretical Chemistry,
Lund University
Jan O. A. De Kerpel, Kristin Pierloot
University of Leuven

Almost all chemical reactions in biology are catalyzed by enzymes. Therefore, one of the most important goals of biochemistry is to understand how enzymes work. Due to the development of fast computers and effective quantum chemical and statistical mechanical software, theoretical methods have now become an alternative to experimental methods for the study of enzyme mechanisms. Our group studies the relation between structure and function of several important groups of metal proteins with theoretical meth-

ods.

One such group is the blue copper proteins, which are characterized by a number of unusual properties, including an intense blue colour, distinctive electron spin resonance spectra, and unusually high reduction potentials. These properties are accompanied by a special cupric geometry: a copper ion bound in a distorted trigonal plane formed by a cysteine and two histidine ligands. In addition, a methionine sulphur atom (and in some proteins a backbone amide oxygen) binds in an axial position at a large distance. These extraordinary properties have traditionally been explained by the protein forcing the Cu(II) ion into a geometry similar to that preferred by Cu(I), the entatic state, and induced rack theories. However, we have optimized the geometry of realistic models of blue copper proteins with quantum chemical methods and shown that the optimal vacuum structures are virtually identical to the crystal structure of the blue copper proteins (figure 5.7 on page 62); that is, there is no need for protein strain.

Therefore, we have started to look for alternative explanations to the unique properties of these proteins. First, we have investigated why the blue copper proteins prefer a trigonal geometry, whereas small inorganic complexes normally assume a tetragonal structure [Olsson *et al.*, 1998a]. In tetragonal structures, four equatorial ligands form σ bonds to the copper ion. Trigonal structures, on the other hand, arise when one ligand instead forms a π bond with two lobes of a Cu 3d orbital, thereby formally occupying two positions in a square coordination (figure 5.8 on page 63). Small and hard ligands give ionic bonds and flattened tetragonal structures, whereas large, soft, and polarizable ligands, such as cysteine and, to a smaller extent, methionine, give rise to covalent copper–ligand bonds and structures close to a tetrahedron.

In fact, a group of blue copper proteins, the rhombic type 1 proteins, have a tetragonal structure with mainly σ bonds to all four ligands [Olsson *et al.*, 1998a, Pierloot *et al.*, 1998]. Yet, their copper geometry is also close to a tetrahedron due to the covalent interaction between copper and cysteine, in which much charge is transferred to the copper ion. The trigonal and tetragonal structures are local minima with almost the same energy (within 7 kJ/mole), separated by a small barrier. Therefore small differences in the proteins may stabilize either structure. We have shown by free-energy perturbations that plastocyanin stabilizes

the trigonal structure by favoring its bond lengths and electrostatics, whereas nitrite reductase prefers the angles of the tetragonal structure, although they have the same copper ligands [De Kerpel and Ryde, 1998].

Second, we have studied the relation between the structure and electronic spectra of the copper-cysteinate proteins [De Kerpel *et al.*, 1998, Pierloot *et al.*, 1998]. The spectra are dominated by two cysteine-to-copper charge-transfer excitations, one from the π-bonding orbital (around 600 nm) and one from the σ orbital (around 460 nm). The relative intensity of these two lines depends on the electronic structure of the ground state of the copper site. Axial type 1 copper proteins with a π-bonded trigonal structure have a low $\epsilon_{460}/\epsilon_{600}$ ratio, whereas the rhombic type 1 proteins have a tetragonal structure with a mixture of σ and π interactions, and therefore a high $\epsilon_{460}/\epsilon_{600}$ ratio. If the structure becomes more flattened, the σ interactions become stronger and the $\epsilon_{460}/\epsilon_{600}$ ratio increases, which may explain the spectra of type 1.5 and type 2 mutant copper proteins.

Finally, we have calculated the inner-sphere reorganization energy of several copper complexes [Olsson *et al.*, 1998b]. The low reorganization energy of the blue copper protein is attained by soft and flexible ligands (small force constants), a low coordination number, and ligands that give oxidized structures close to a tetrahedron. We have also started to investigate the redox potentials of the blue copper proteins. The axial ligands seem to have a smaller influence on the redox potentials than what is normally assumed [Ryde *et al.*, 2000]. Instead, solvent effects seem to play the major role. More information on our blue copper project can be found at `http://signe.teokem.lu.se/~ulf/Projects/bluecop.html`.

Porphyrin proteins are another group of proteins we have studied. Porphyrins are large, cyclic, aromatic molecules that may bind metal ions. They function as electron transfer sites as well as catalytic centres; they also play a pivotal role in many biological processes, such a photosynthesis and respiration. Typical examples are haem, chlorophyll, vitamin B12, and coenzyme F430.

After a thorough test of various methods and basis sets to be used on metal porphyrins, we have investigated how myoglobin discriminates between O_2 and CO [Sigfridsson and Ryde, 1999]. CO binds around 20,000 times as strongly as O_2 to free haem group in solution, but in the proteins this factor is only 25. Thus,

We have calculated the inner-sphere reorganization energy of several copper complexes.

myoglobin favors O_2 before CO by about $17\,$kJ/mole. This is crucial to life, because about $1\,\%$ of the haem units are poisoned by endogenously produced CO. According to biochemical textbooks, the reason for this is that the so-called distal histidine residue forces CO to bind in a bent fashion (the natural conformation of O_2). Although this suggestion is supported by X-ray and neutron structures, recent spectroscopic experiments have questioned it. We have studied hydrogen bonds between histidine and a haem-bound CO or O_2 (figure 5.9 on page 64). The energy difference of hydrogen bonds to these two ligands, 24 kJ/mole, is close to the size of the protein's discrimination between these two molecules. Thus, our results indicate that the protein discriminates between the two ligands by electrostatic means rather than by strain.

At PDC we use the IBM SP parallel computer for quantum chemical geometry optimizations, using density functional methods. Mostly we use the hybrid B3LYP functional, but for the largest systems we have also used the Becke-Perdew-86 functional together with the RI (resolution of identity) approximation for the calculation of the repulsion integrals, which typically speeds up the calculation with a factor of five. We have used the Turbomole software for the calculations, because it shows a nearly linear scaling on up to at least 64 nodes. Other calculations are done on our local sequential computers. PDC is clearly essential for our research. Typically our model systems contain 40–60 atoms and 300–800 basis functions. Although we study the smallest system that gives reliable results and use as effective methods and as small basis sets as possible, the geometry optimizations are on the verge of present computational capacity. A typical geometry optimization of a metal porphyrin with two axial ligands and no symmetry takes about 2–3 CPU-months (1,500–2,000 hours) to optimize on a sequential computer. At PDC we can optimize three or four such models each month.

4.10 Transport Properties and Phase Behavior of Liquid Crystals via Molecular Dynamics Simulation Systems

Sten Sarman
Department of Physical Chemistry, Göteborg University

There is a wide variety of liquid crystal phases and phase transitions between them [Chandrasekhar, 1992]. The lower symmetry of the liquid crystal means that the transport properties are much richer than those of isotropic liquids. This is because linear cross couplings between thermodynamic forces and fluxes of different rank and parity are allowed. An example of this is the coupling between the symmetric traceless strain rate and the antisymmetric pressure, which gives rise to flow alignment in nematic liquid crystals. Another example is the coupling between the temperature gradient and the director angular velocity in cholesteric liquid crystals.

In order to study a liquid crystal by computer simulation, one needs a molecular model system. We use models that are based on the Gay-Berne potential [Gay and Berne, 1981, Brown *et al.*, 1998], which can be regarded as a Lennard-Jones potential generalized to elliptical molecular cores. It has been shown to display a rich liquid crystal phase diagram. One can form more complicated molecules by joining a number of interaction sites. We have studied two such models and mapped parts of their phase diagrams.

One of the models consists of rigid linear strings of oblate Gay-Berne ellipsoids, the symmetry axes of which are parallel to each other and perpendicular to the line joining their centers of symmetry (see figure 4.9). These molecules are elongated in one direction and flattened in another direction. They have been found to form liquid crystal phases that are ordered in two directions [Sarman, 1996]. The long axes of the molecules orient in approximately the same direction, and the symmetry axes of the oblate interaction sites orient around the perpendicular direction. Such phases are known as biaxial nematic liquid crystal phases, and their potential technological applications include switching devices in electronic equipment. We have studied the dependence of the topology of this fluid's phase diagram upon the molecular shape and have compared the results with various theories. The results can be used to guide the synthesis of molecules that can form biaxial liquid

Applications for biaxial nematic liquid crystal phases include switching devices in electronic equipment.

Figure 4.9. The model system. The particles consist of a linear string of oblate Gay-Berne ellipsoids of revolution. Their symmetry axes are parallel to each other and perpendicular to the line joining their centers of mass. The principal axes are denoted by $\hat{u}$, parallel to the symmetry axes of the ellipsoids; $\hat{v}$; and $\hat{w}$, parallel to the line through the centres of mass. (a) Projection perpendicular to the $\hat{u}$-axis. (b) Projection perpendicular to the $\hat{w}$-axis.
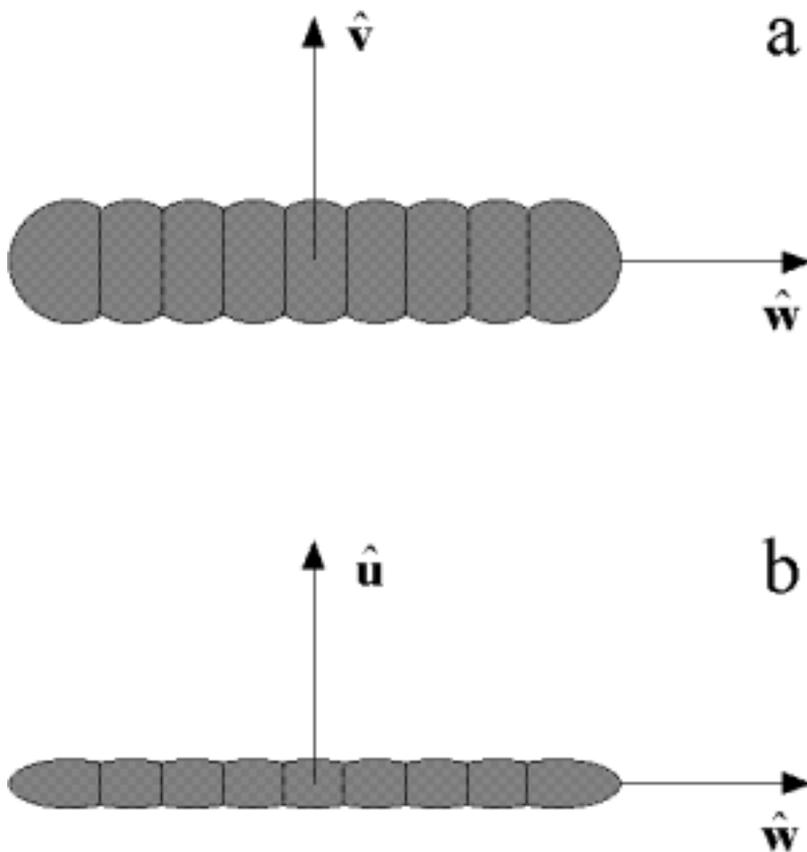
crystals.

By modifying the biaxial model in such a way that the symmetry axes of the oblate interaction sites are still perpendicular to the line joining their centers of symmetry but letting the angle between the symmetry axes of two adjacent interaction sites be constant, one generates a twisted object (see figure 4.10). At high densities they form cholesteric liquid crystals. They can be regarded as nematic liquid crystals where the director is twisted around an axis, the cholesteric axis, perpendicular to itself. A cholesteric liquid crystal is different from its mirror image. A consequence of this is that a temperature gradient (which is a polar vector) parallel to the cholesteric axis can induce a torque (which is a pseudo-vector) that rotates the director. This is known as the Lehman effect. Three transport coefficients are involved in the Lehman effect: the thermal conductivity, the twist viscosity, and

the cross-coupling coefficient between the temperature gradient and the angular velocity of the local director.

We have derived novel Green-Kubo methods and nonequilibrium molecular dynamics (NEMD) simulation methods [Evans and Morriss, 1990, Sarman *et al.*, 1998, Sarman, 1998, Sarman, 1999] to evaluate these coefficients in cholesteric liquid crystals. These methods are based on linear response theory, and similar methods have previously been applied successfully to evaluate the viscosities of nematic and smectic liquid crystals [Sarman, 1995]. In order to simulate liquid crystals, one also needs a Lagrangian constraint algorithm to make the angular velocity of the director a constant of motion. These methods give rise to non-Newtonian equations of motion, but one can show that the thermodynamic properties and transport coefficients are the same as the ones generated by conventional Newtonian equations. Our numerical results show that the cross-coupling coefficient between the temperature gradient and the director angular velocity for the molecules in figure 4.10 is finite but very small [Sarman, 2000]. This could be the reason why it is very hard to detect experimentally [Chandrasekhar, 1992]. More calculations are under way to study this cross coupling at other state points.

We finally note that both the evaluation of transport coefficients and the mapping of phase diagrams require very long simulation runs. Thus, it is necessary to use fast parallel machines in order to obtain results. The IBM SP is particularly useful for this purpose, because it is easy to convert serial codes to data parallel codes that parallelize very well.

We have derived novel Green-Kubo methods and NEMD simulation methods to evaluate cholesteric liquid crystals.

4.11 Wave Packet Dynamics Applied to X-Ray Raman Scattering

Paweł Sałek
Department of Physical Chemistry, KTH

Vibrationally resolved spectra of resonant X-ray Raman scattering (RXS) is a topic of intense current interest due to insights that such data provide into the underlying dynamics of RXS and interatomic interaction. During the last decade, our knowledge of the role of the electron-nuclear degrees of freedom on the formation of the RXS spectral profile increased essentially due to the discovery of a set of new effects [Nordgren, 1997, Mårtensson *et al.*, 1997, Svensson

Figure 4.10. (a) The molecular model for molecules that form cholesteric liquid crystals. The molecules are composed of a linear string of six interaction sites consisting of oblate Gay-Berne ellipsoids. The symmetry axes of the ellipsoids are perpendicular to the line joining their centers of mass. The angle between the axis vectors of two consecutive ellipsoids is constant and equal to 7.5°. Consequently, the molecules are rigid bodies. The axis parallel to the line joining the centers of mass is denoted by $\hat{w}_i$, which becomes the twist axis. The other two axes of the principal coordinate system are denoted by $\hat{u}_i$ and $\hat{v}_i$. The symmetry axis of interaction site α of molecule i is denoted by $\hat{u}_{i\alpha}$. (b) Planar projection of the molecule perpendicular to the $\hat{w}_i$-axis. The angles between the $\hat{u}_{i\alpha}$-axes have been exaggerated for the sake of clarity.
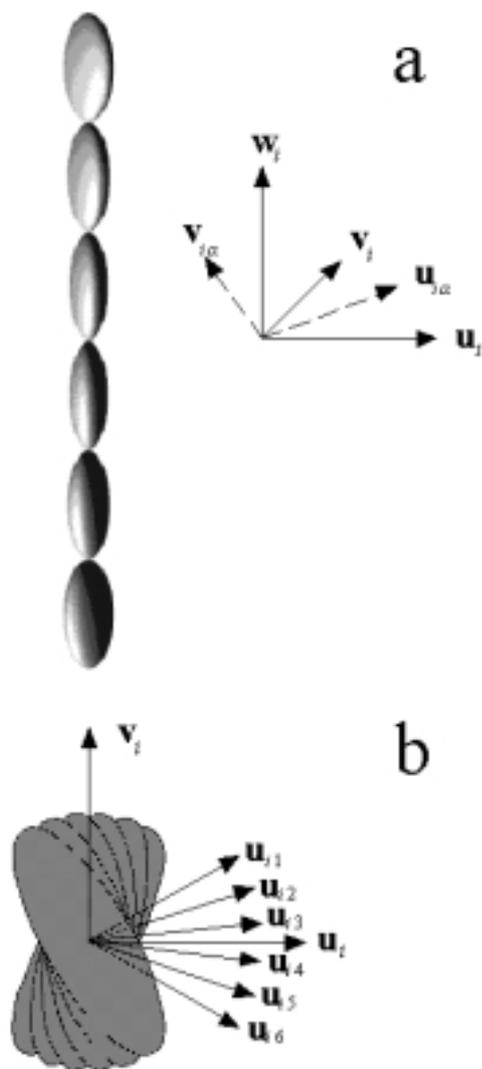
and Ausmees, 1997, Crasemann, 1998, Gel'mukhanov and Ågren, 1999].

We have developed in our group the RXS theory and the computational methods for calculating an RXS cross section. On this foundation, we have written a program meant originally for an ordinary workstation, and we subsequently parallelized and ported it to the massively parallel IBM SP at PDC. The program is able to perform computations for 1D systems, bound as well as dissociative. The 2D version is presently in an advanced test phase.

The developed code serves several purposes.

- We have been able to understand better the X-ray Raman scattering process and the meaning of different parameters governing this process, particularly for dissociative systems. Specifically, we have been able to confirm earlier analytical predictions [Gel'mukhanov and Ågren, 1996] concerning detuning of the excitation frequency from the resonance. In particular, large detuning supresses the atomic feature in the spectrum (see figure 5.10 on page 65).

We have been able to confirm earlier analytical predictions.

- We tested the validity of diverse approximation in the RXS theory; we have for instance discovered that although the Franck-Condon approximation works as expected for the excitation process, the molecular geometry dependence of decay transition moments often cannot be neglected. The abnormal spectrum flattening [Piancastelli *et al.*, 2000] for N_2 is an example of such a process.

- We have predicted new effects like the so-called atomic hole spectral feature, very recently observed experimentally [Feifel and *et al.*, 2000].

The developed program uses the MPI parallel library for communication. Because we succeeded in developing an algorithm that minimizes the inter-process communication in terms of both frequency and message size, the message-passing approach turned out to be sufficiently efficient.

The IBM SP has been used for the production calculations. We have also used the experimental PC cluster for code development and algorithm testing due to lower load on this machine and shorter time between job submission and execution. The short

waiting time—at most, a few hours—has been important for us because it shortens the development cycle.

The production calculations were submitted via the queue system. We usually used between 10 and 40 processors for a single job. The parallel facilities shortened the computations' wall-clock time from weeks to days. This made it possible to verify different hypotheses faster and to provide more accurate feedback to our research collaborators.

5 Color Plates
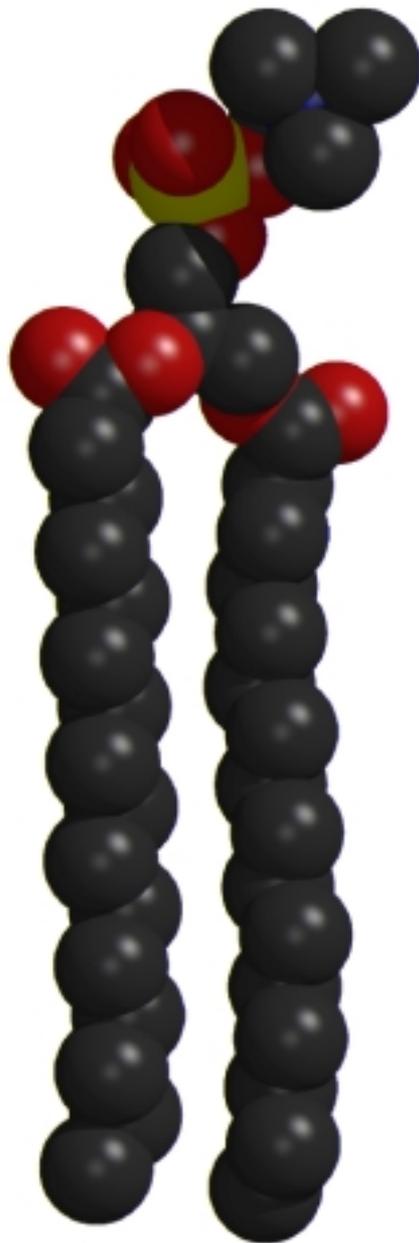
Figure 5.1. A single molecule of DPPC (dipalmitoylphosphatidyl-choline). The two "legs" consist of hydrophobic atoms and point inward to the center of the membrane. The "head" part is a dipole in contact with the water outside. (See Section 3.2 on page 14.)
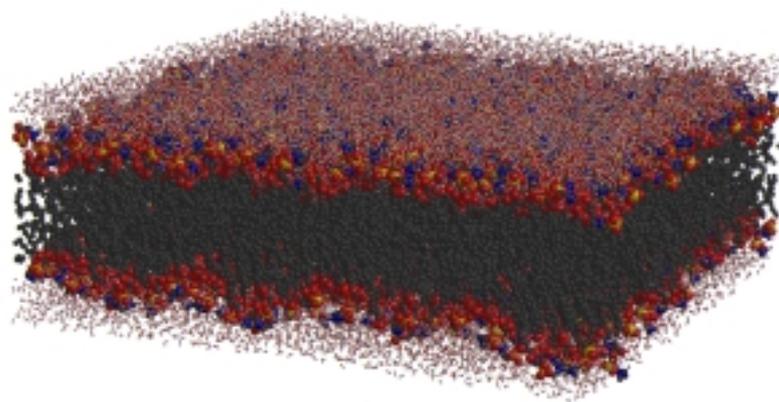
Figure 5.2. A DPPC membrane patch sized 16×16 nm. This system consists of 121,856 atoms including water and is the largest membrane simulation performed to date. (See Section 3.2 on page 14.)
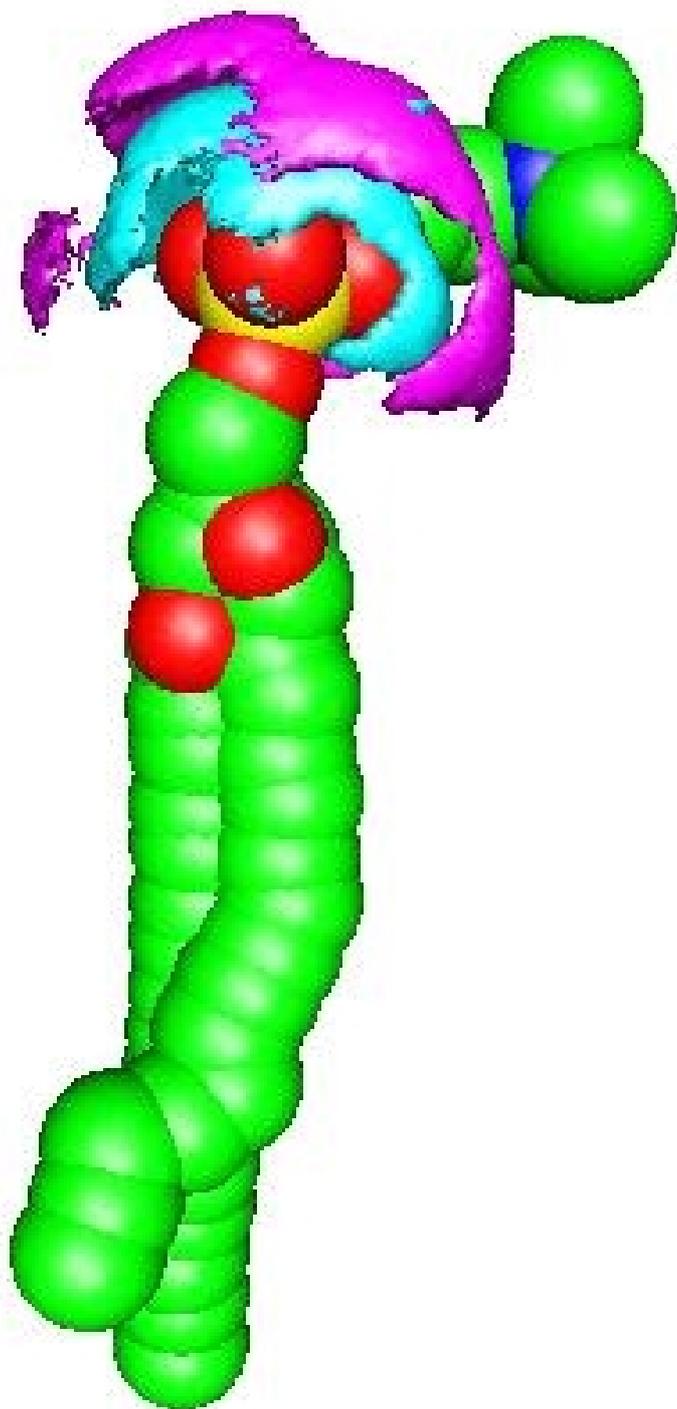
Figure 5.3. The spatial distribution function of water oxygen (red) and hydrogen (blue) around the head group of a lipid molecule. The isosurfaces are drawn at level 5. (See Section 3.3 on page 17.)

Figure 5.4. Protons on the clean mica surface hydroxylated the surface, preferably the AlO$_4$ tetrahedra. In first-principles molecular dynamics simulations of the wet surface, there was a balance between proton solvation in water and surface hydroxyl groups and continuous proton transfer occurred. (See Section 4.1 on page 27.)
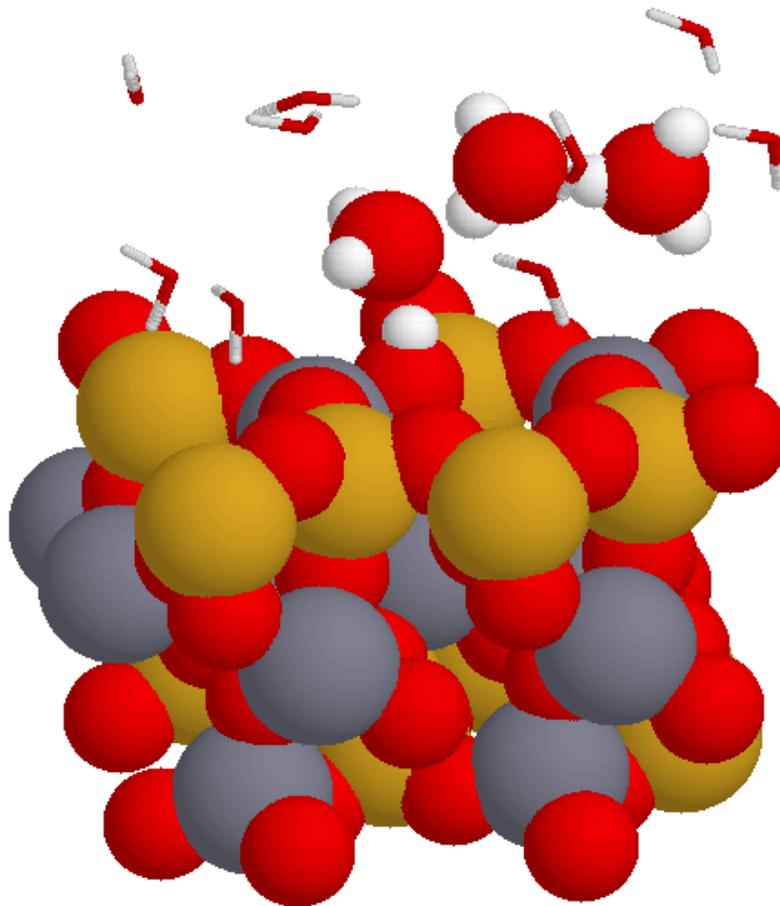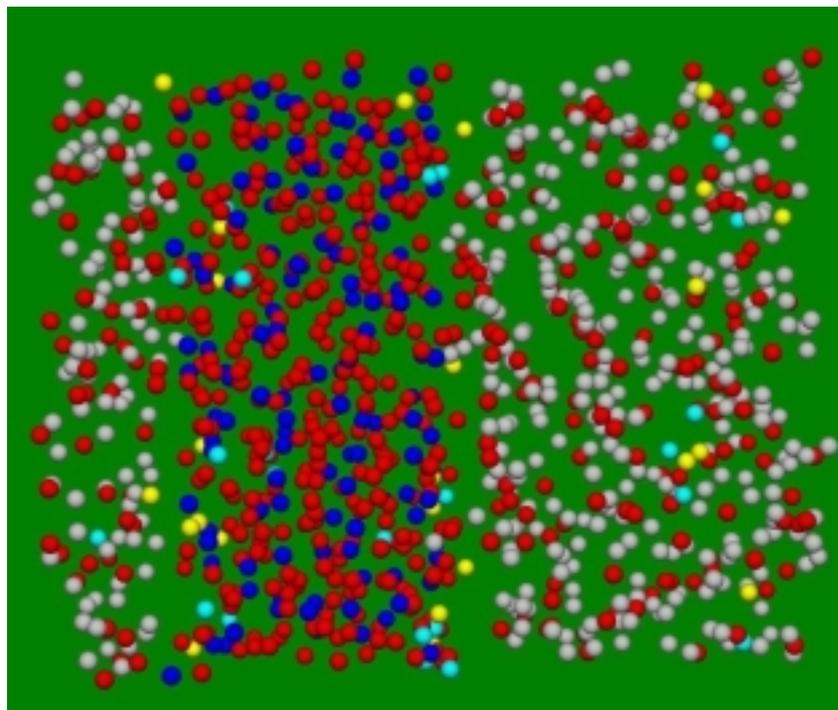
Figure 5.5. A typical snapshot of the simulated model during the final "sampled" stages of the simulation. (See Section 4.3 on page 33.)
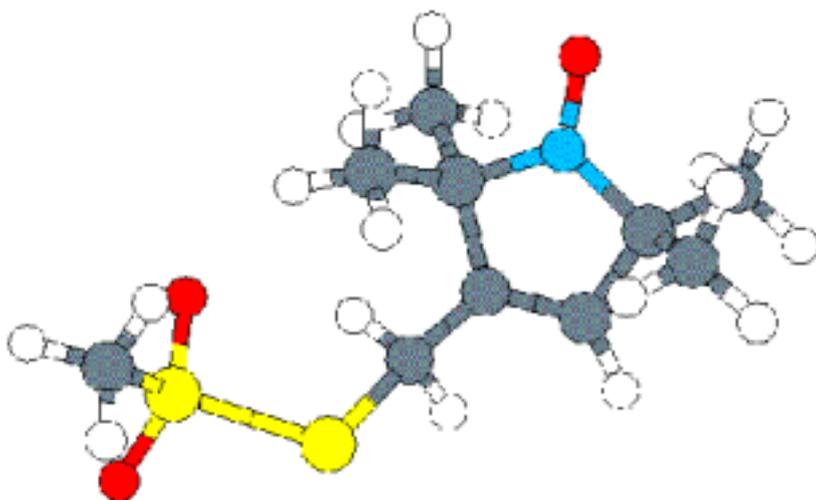
Figure 5.6. (1-oxyl-2,2,5,5-tetramethylpyrroline-3-methyl) methanethiosulfonate spin label (MTSSL). (See Section 4.4 on page 35.)

Figure 5.7. A comparison of the optimised structure of $Cu(imidazole)_2(SCH_3)(S(CH_3)_2)+$ and the crystal structure of plastocyanin (shaded). (See Section 4.9 on page 47.)
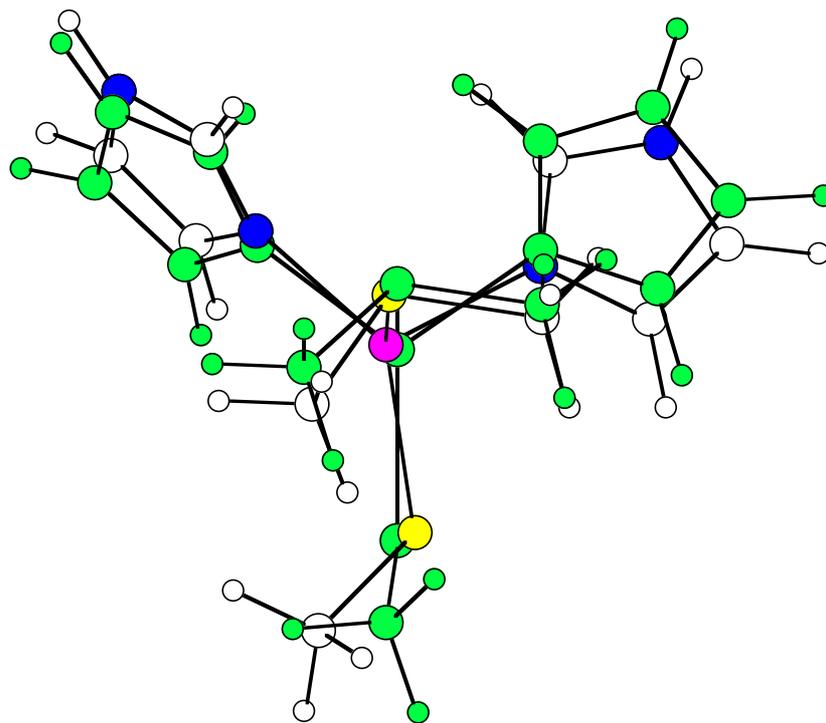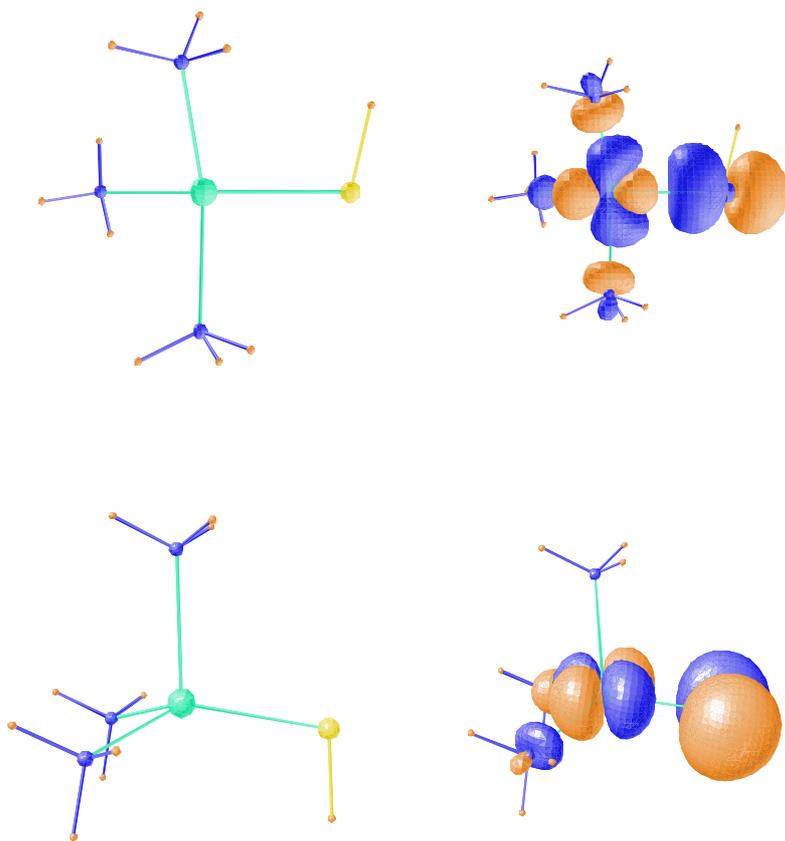
Figure 5.8. The singly occupied orbital of the tetragonal (a) and trigonal (b) $Cu(SH)(NH_3)_3+$ complex1. (See Section 4.9 on page 47.)

Figure 5.9. The optimised structures of the O$_2$ and CO complexes of iron porphine with imidazole groups as an axial ligand as well as a model of the distal histidine group5. (See Section 4.9 on page 47.)
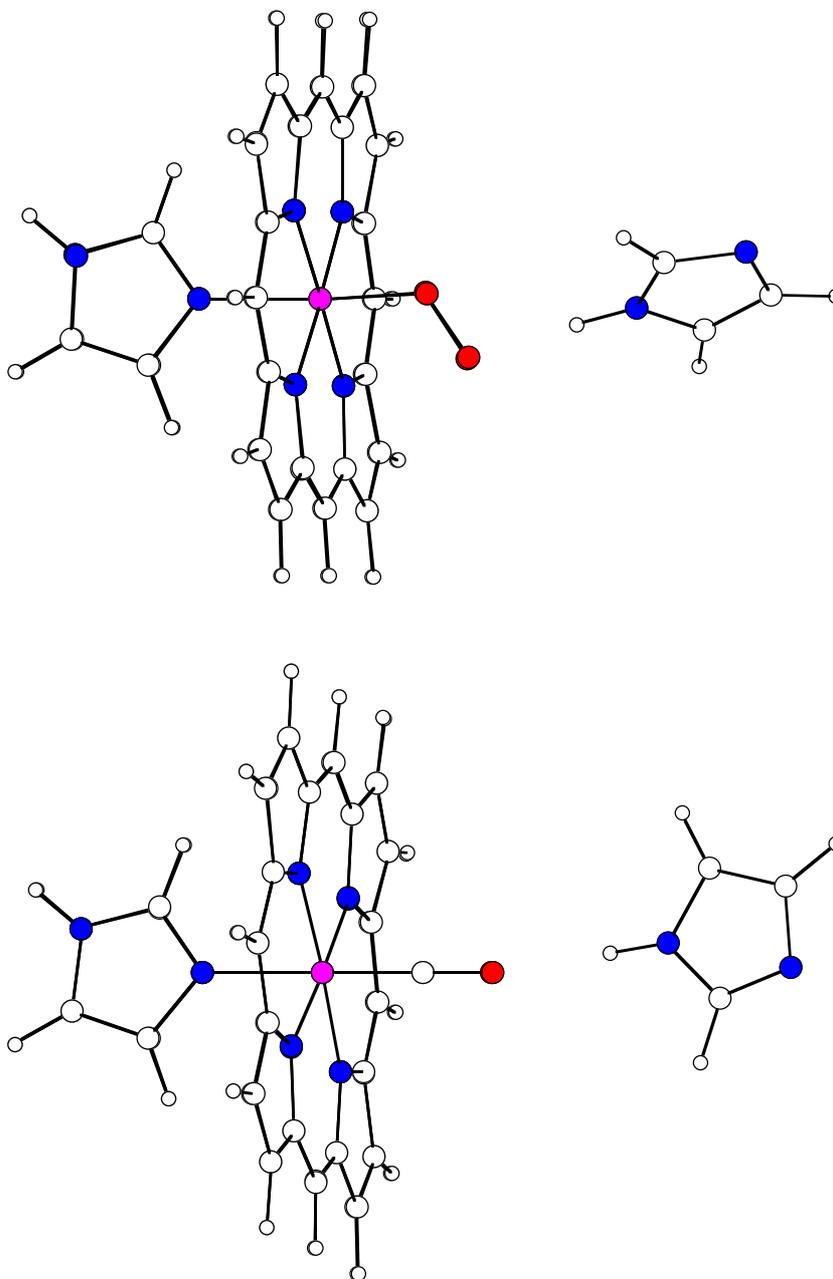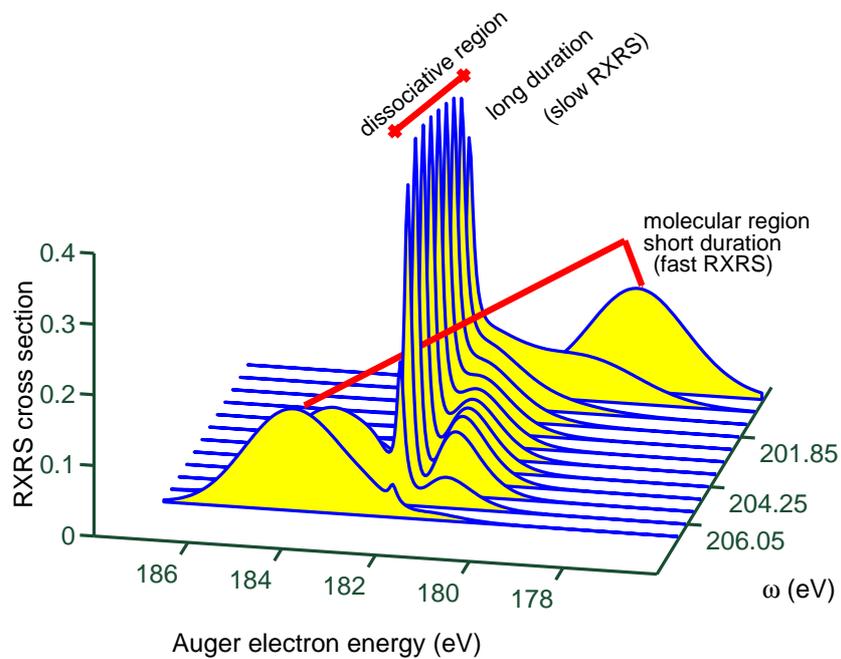
Figure 5.10. The figure shows the X-ray Raman scattering cross section of HCl corresponding to the decay to $^2\Sigma^-$ final state, with respect to the excitation frequency ω and emitted Auger electron energy E. The atomic peak at constant position of 182eV is clearly seen. (See Section 4.11 on page 53.)
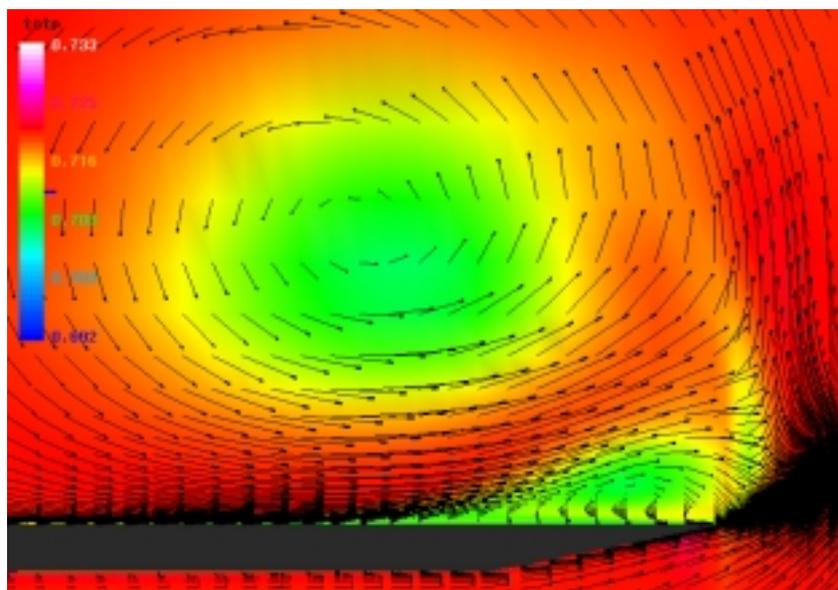
Figure 5.11. Crossflow over a single-bevel delta-wing model. (See Section 6.1 on page 75.)

Figure 5.12. Computed lift coefficients compared with experimental data ($M_{\mathrm{inf}} = 0.1615, Re_c = 1.97 \times 10^6$). (See Section 6.1 on page 75.)
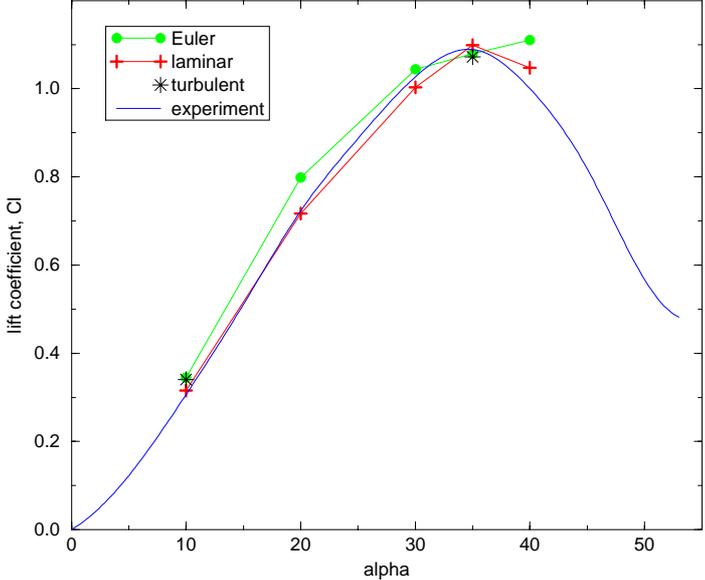
Figure 5.13. Vortex breakdown over a double-bevel delta-wing model, turbulent computation ($\alpha = 35$ deg, $M_{\mathrm{inf}} = 0.1615, Re_c = 1.97 \times 10^6$). (See Section 6.1 on page 75.)
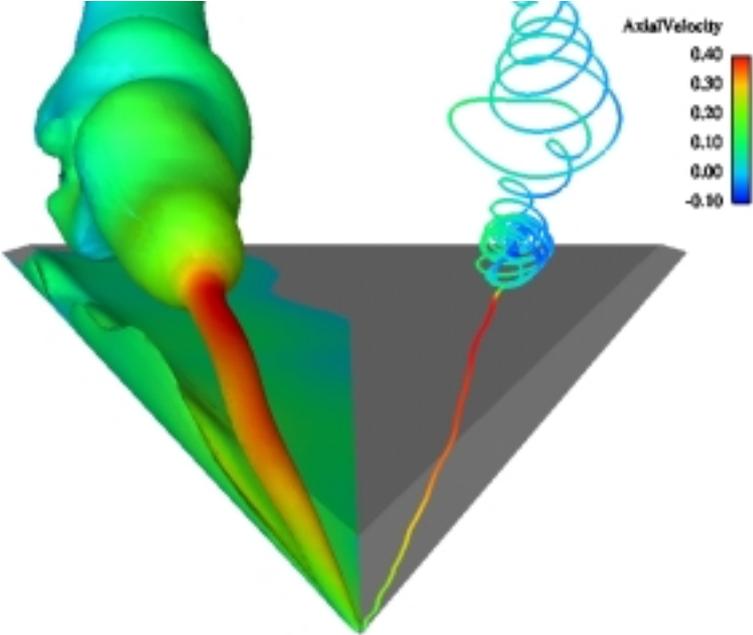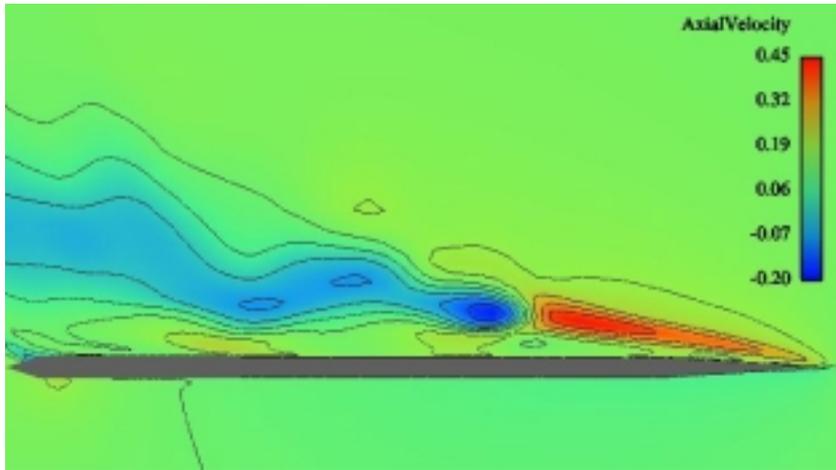
Figure 5.14. Contours of the axial component of the velocity in a plane through the burst at 35 deg incidence. (See Section 6.1 on page 75.)
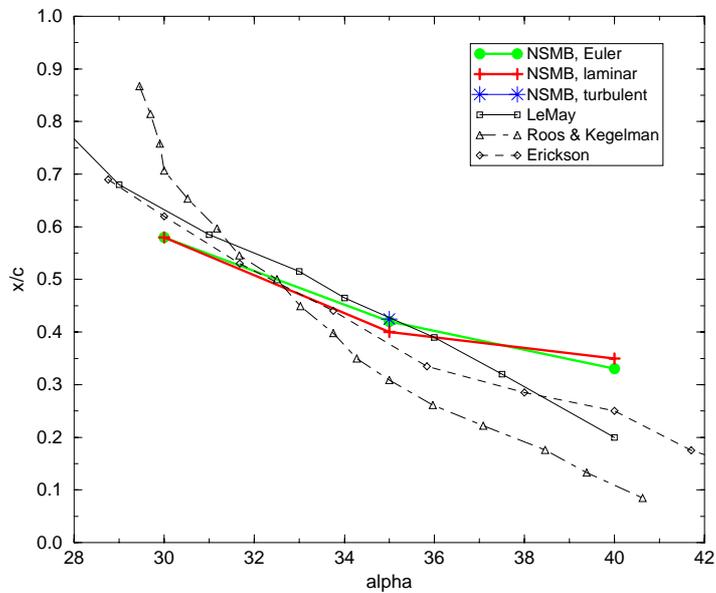
Figure 5.15. Computed breakdown locations compared with experimental data. (See Section 6.1 on page 75.)

Figure 5.16. A grid generated with ICEM CFD Hexa for the wing-body model (coarse mesh). (See Section 6.1 on page 75.)
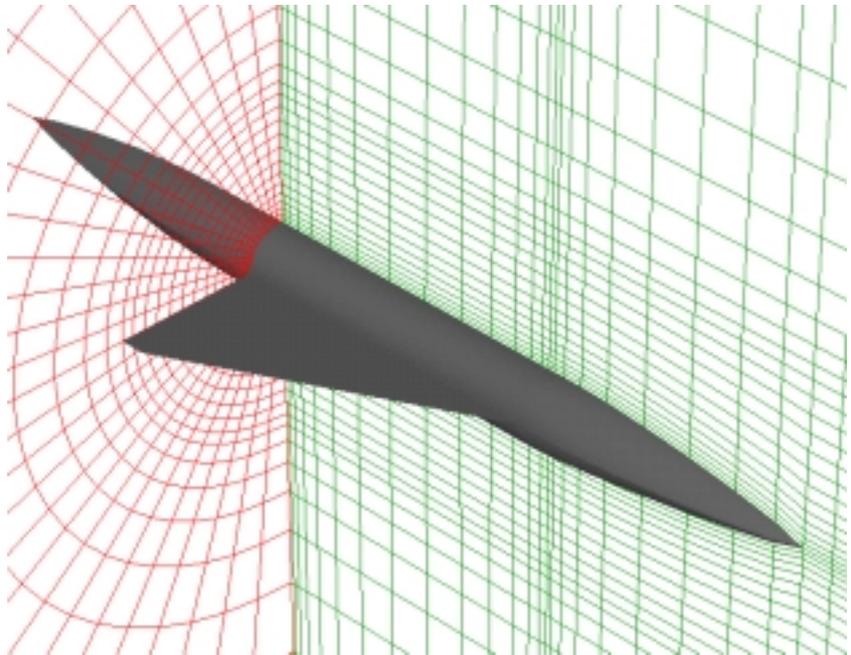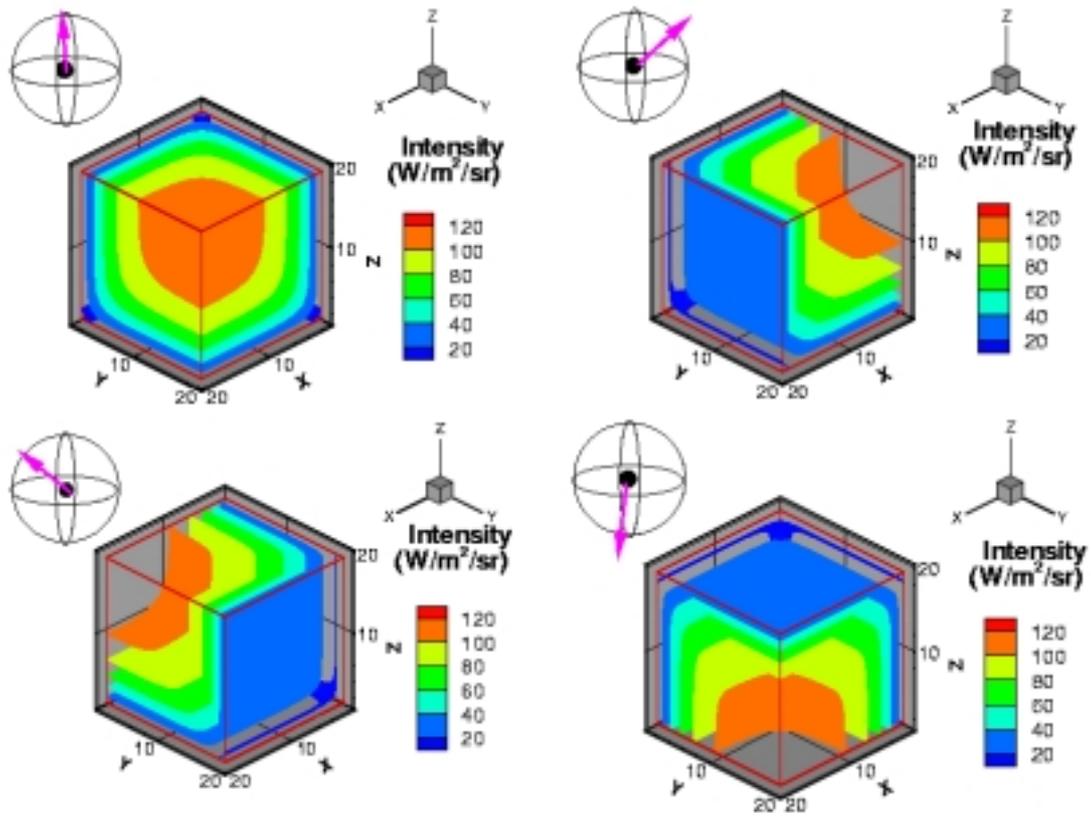
Figure 5.17. Radiative intensity for different directions inside a cube with uniform temperature of 300 K, black cold walls (0 K), and an absorption coefficient of 0.1 (See Section 6.5 on page 91.)
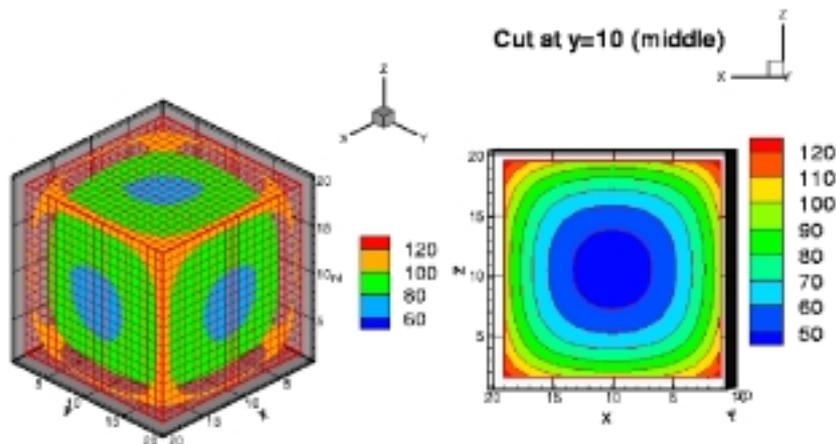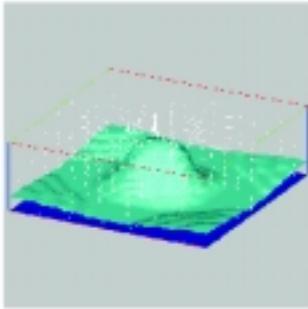
Figure 5.18. Computation of the divergence of the heat flux for a cube with uniform temperature of 300 K, black cold walls (0 K), and an absorption coefficient of 0.1 (See Section 6.5 on page 91.)
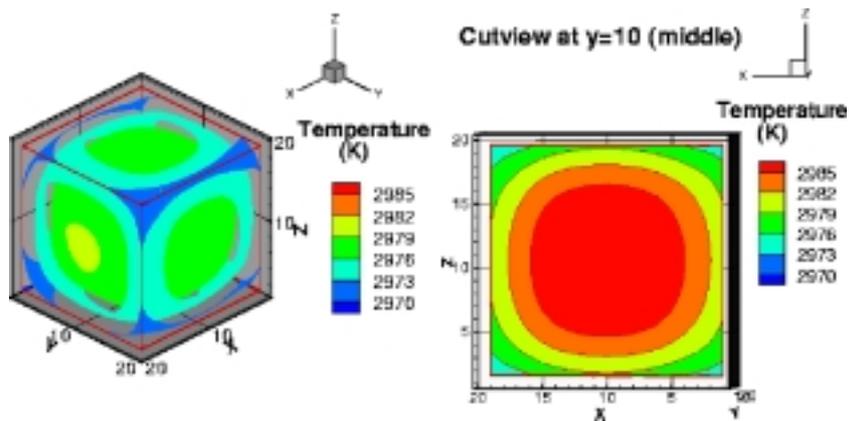
Figure 5.19. Influence of the radiative heat transfer on the temperature of a cube at an initial temperature of 3000 K. (See Section 6.5 on page 91.)
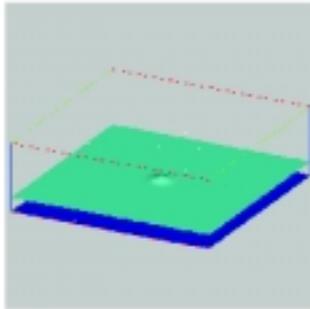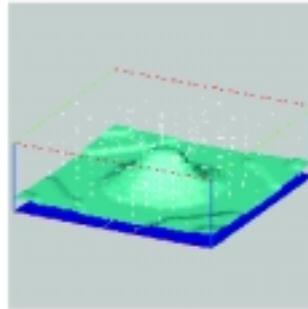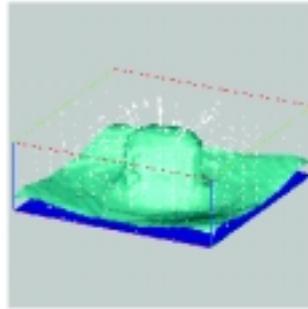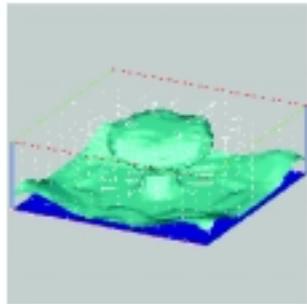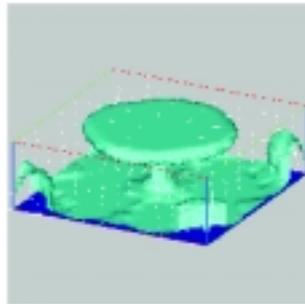
Figure 5.20. 3D view of a sediment/salt interface and flow patterns (arrows) at times: initial (A), 2.7 My (B), 3.0 My (C), 3.3 My (D), 3.9 My (E), and 5.5 My (F). (See Section 6.7 on page 106.)

A

B

C

D

E

F

Figure 5.21. a: 1-blade passage mesh (2 blocks). Single/multiple blade passage multi-block H-type meshes for the NASA Rotor 67. (See Section 8.3 on page 115.)
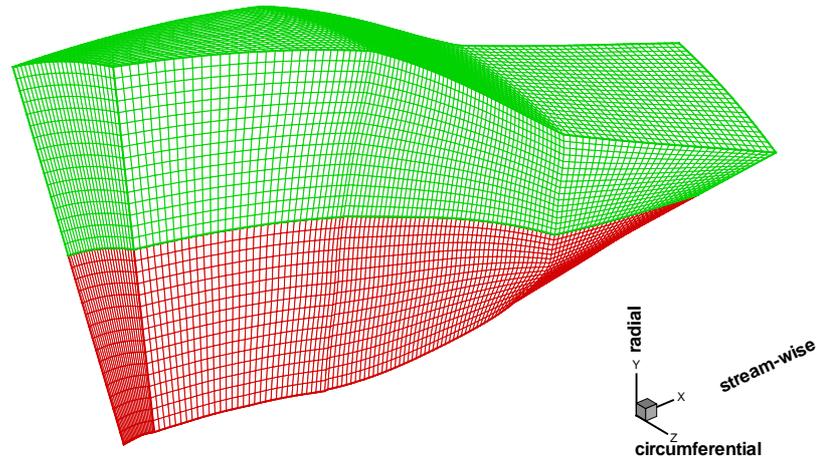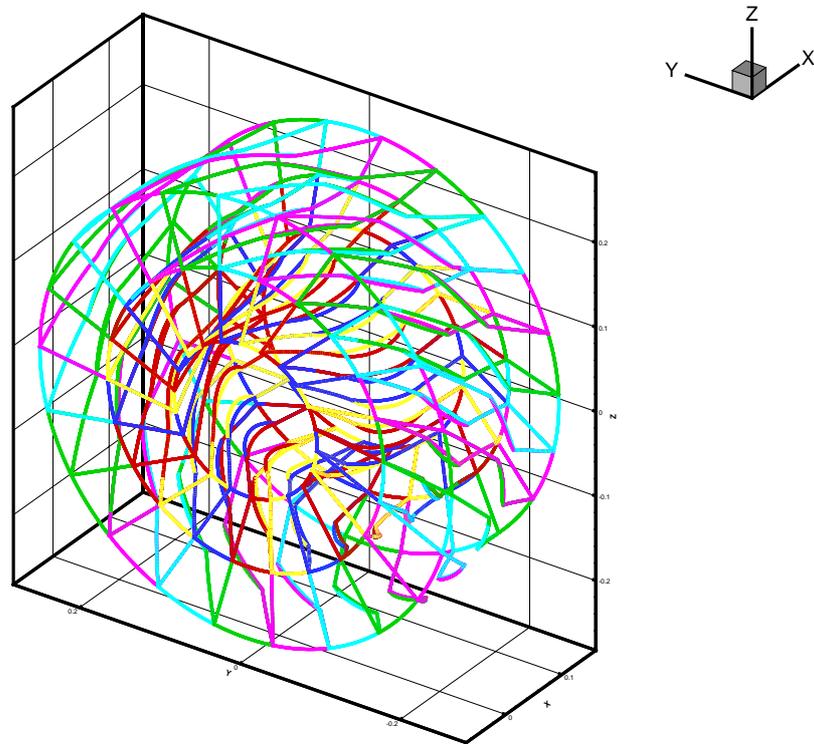

Figure 5.22. b: 22-blade passage mesh (44 blocks, 2,113,100 nodes). Single/multiple blade passage multi-block H-type meshes for the NASA Rotor 67. (See Section 8.3 on page 115.)
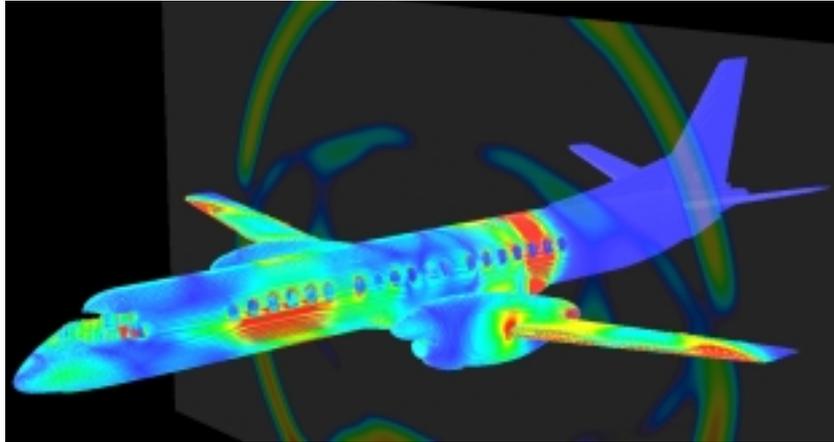
Figure 5.23. The surface currents on the Saab 2000 aircraft 125 ns (1500 time steps) after a lightning strike on the nose. Also shown is the magnitude of the magnetic field on a cutting plane across the wings perpendicular to the fuselage. (See Section 8.5 on page 119.)
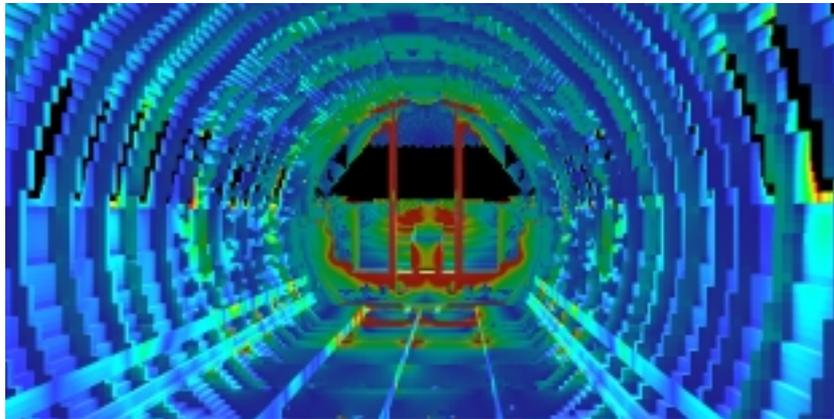

Figure 5.24. The interior of the Saab 2000 aircraft. Surface currents are shown at the same time as in figure 5. The view is from the center of the aircraft towards the cockpit. High surface currents are seen on the door pillar and the sill. To prevent cables from picking up high induced currents, one must know the field picture inside the aircraft so that proper countermeasures can be taken. (See Section 8.5 on page 119.)

Figure 5.25. Results from the base case (REF) scenario. (See Section 8.9 on page 132.)
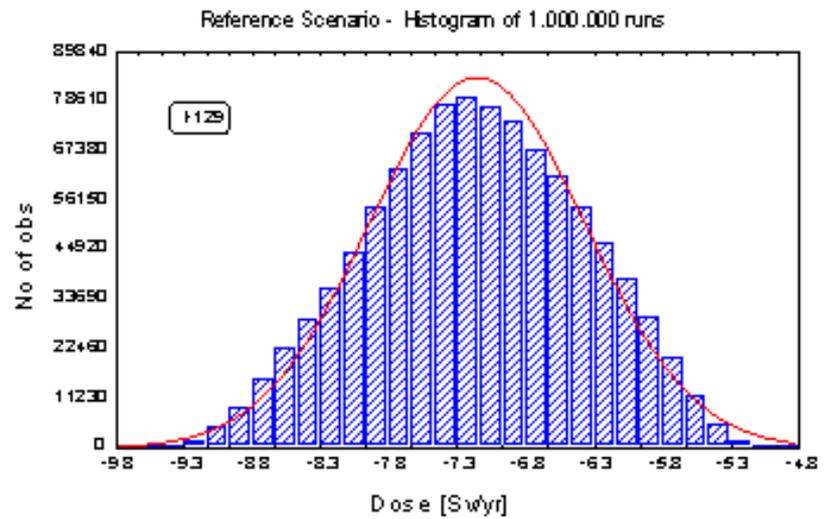

**Figure 5.26.** AFM topographical image of a photoresist sample on silicon. The feature was about $10 \times 10 \times 3\,\mu$m, and the surface roughness was imprinted with e-lithography at NPL, UK. On the right is a side view of the same sample. The color bar shows the heights in nm. The topography of this sample was used as input data for light-scattering simulations on the Fujitsu VX/3. (See Section 8.10 on page 133.)
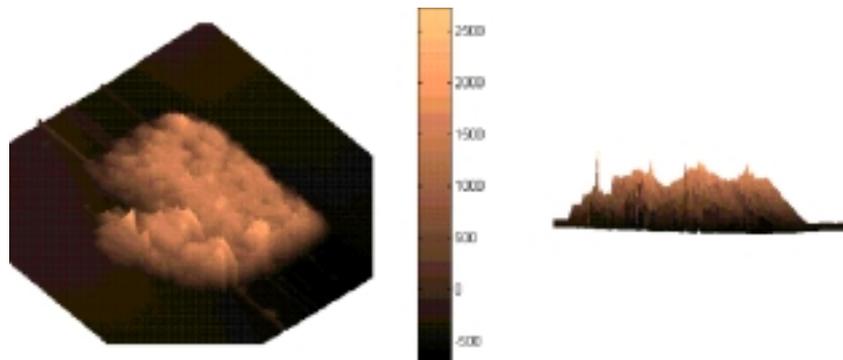
6 Computational Fluid Dynamics

6.1 Aerodynamics of Delta Wings at High Angle of Attack

Stefan Görtz, Arthur Rizzi
Department of Aeronautical Engineering, KTH

In the project described here, the aerodynamics of delta wings at high angle of attack were investigated numerically. At moderate to high angles of attack, delta wings benefit from the lift-enhancing effects of the vortices generated by the roll-up of the shear layer emanating from the wing's leading edges. These vortices induce additional velocities on the suction surface of the wing providing lift and maneuverability well beyond what would be expected if the flow remained attached.

The generally very stable and lift-enhancing leading-edge vortices may burst at very high angle of attack, affecting the aerodynamic characteristics of the wing by reducing the magnitude of the vortex suction peak and increasing its width. Vortex burst or breakdown is associated with a rapid deceleration of the highly organized vortex core and a sudden expansion of the core into bubbles or spirals along the core axis.

This project investigates if the aerodynamic characteristics of such flow fields, in general, and especially if the phenomenon of vortex breakdown can be modeled accurately enough for practical use in the Navier-Stokes Multi Block (NSMB) simulation code. In particluar, we seek to determine if, due to inclusion of the secondary vortex effects, the predictions made by Navier-Stokes solutions are qualitatively and quantitatively more accurate than Euler solutions. Initially, only stand-alone delta-wing planforms were investigated, that is, no fuselage was modeled. More recently a generic delta-wing/body model was simulated. The ultimate goal of the project is to compute a full fighter-type configuration numerically.

We seek to determine if the predictions made by Navier-Stokes solutions are qualitatively and quantitatively more accurate than Euler solutions.

Computational Method

The serial version of the Navier-Stokes Multi Block (NSMB) code [Vos *et al.*, 1998] was used on PDC's Fujitsu VX/3 throughout this numerical study. In NSMB, the cell-centered finite volume method using block-structured grids is employed to discretize the Navier-Stokes equations. The inviscid flux vectors at cell faces are approximated using Jameson's central scheme or the second- and third-order Total Variation Diminishing (TVD) version of Roe's upwind scheme applying the Monotone Upwind Scheme for Conservation Laws (MUSCL) extrapolation. The viscous fluxes are calculated at the surface center using the gradient theorem on a shifted control volume.

The resulting system of equations is integrated in time using either the explicit Runge-Kutta scheme or the implicit Lower-Upper Symmetric Gauss-Seidel (LU-SGS) scheme. Various turbulence models of different complexity are available in NSMB. In this project the algebraic model of Baldwin-Lomax, the one-equation model by Spalart and Allmaras, and the two-equation model by Chien and Hoffman were used.

Discussion of Selected Results

The numerical study of 70° sharp-edged delta wings [Görtz, 1998] demonstrated that the basic features of the vortical flow can be simulated accurately from a qualitative point of view. Figure 5.11 shows the solution computed for a single-bevel delta-wing model at 25° angle of attack in a plane perpendicular to the freestream direction. One can clearly identify leading edge separation, the primary vortex (circular green-blue region), crossflow (vector arrows), secondary separation, flow reversal, and a secondary vortex.

The quantitative accuracy of the modeling was judged on four specific criteria, compared when possible with experimental measurements:

The quantitative accuracy of the modeling was judged on four specific criteria, compared when possible with experimental measurements.

1. variation of the integrated aerodynamic coefficients with angle of attack,

2. flow topology over the delta wing including surface pressure,

3. axial position of the vortex breakdown over the wing, and

4. the axial velocity profile along the axis of the vortex core.

A major objective of the comparison is to assess the relative influence of factors effecting the accuracy. Physical aspects include the thickness and camber of the wing, the Reynolds number of the flow, and laminar-turbulent flow; modeling aspects include the topology of the mesh, the number of grid points, the spatial discretization scheme, and the turbulence model. Such an assessment in its entirety involves a very comprehensive comparison, and is well beyond the scope of this paper. Here we focus on a few selected results that illustrate the main effects that we have observed so far. Additional results are found in the corresponding references.

The integrated lift coefficients are plotted for a double-bevel delta-wing model in figure 5.12 and compared with wind-tunnel measurements for the same geometry and flow conditions. The laminar lift coefficients are in best agreement with the experimental data. The Euler values are generally too high, that is, the Euler equations overestimate lift. At 10° angle of attack the turbulent computations using the Baldwin-Lomax model overestimate lift by 11 %. The corresponding values are 3 % for the laminar case and 12 % for the Euler case. The turbulence model by Spalart and Allmaras underestimates the lift coefficient by 1.5 % at 35° incidence. Other research [Weber and *et al.*, 1998] found as well that 0-equation turbulence models overestimate lift, whereas the Spalart-Allmaras model underestimates the experimental values. The Euler equations are not capable of predicting maximum lift. The inviscid lift coefficient rather continues to increase even after stall, whereas stall is predicted by the laminar computations. This is a very important finding, because the prediction of stall is crucial in determining the characteristics of delta-wing aircraft at high angles of attack. It is remarkable that the difference between the computed laminar and the experimental maximum lift coefficient is less than 1 %.

Furthermore, it was found that both Euler and Navier-Stokes equations are capable of predicting the phenomenon of vortex breakdown. Figure 5.13 shows the 3D-view of breakdown for a turbulent computation of a double-bevel delta-wing model at 35° angle of attack using the 1-equation turbulence model by Spalart and Allmaras. A freestream Mach number of $M = 0.1615$ and a Reynolds number (based on the root chord length) of $Re_c = 1.97e6$ were specified. The left side of the picture shows an isosurface of

Euler and Navier-Stokes equations are capable of predicting the phenomenon of vortex breakdown.

total pressure colored in magnitude of axial velocity. The feeding shear layer can be seen to emanate from the leading edge. The primary vortex itself emanates from the apex of the wing. It curves slightly inboard when intercepting the flat upper surface but curves back further downstream.

The fluid entrained in the core accelerates gradually along the core until the magnitude of the axial velocity reaches a value of about Mach 0.4, that is, about 2.5 times the freestream velocity. Notice the following expansion of the core and the preceding deceleration of the axial fluid. On the right side of the figure, the streamline identifies the vortex core filament that begins to spiral around its own axis after breakdown. The computed vortex core line features a kink at the location of breakdown, a behavior that was also found in experimantal investigations. A recirculation zone is seen downstream of the breakdown point. The spiraling nature of the core behind the recirculation zone suggests that a bubble-type of breakdown with a "spiraling tail" has been predicted.

The axial component of velocity in a plane through the burst vortex at 35° incidence is shown in figure 5.14. The axial velocity component along the vortex core axis begins with freestream velocity and then accelerates over the apex and along the core as the vortex develops. It continues to increase up to some distance before breakdown. A position is eventually reached where the velocity does not increase further, but reaches some maximum, remaining at that magnitude for some distance, until decelerating abruptly over a distance in the order of the core diameter.

The breakdown location was seen to be independent of physical modeling (see figure 5.15). The breakdown position appeared to depend on the different numerical schemes—Roe's upwind scheme predicted a more upstream burst position than the central scheme. Viscous effects, such as secondary separation, were seen in the Navier-Stokes computations but not in the Euler computations. Vortex trajectories showed good agreement with experimental data in the spanwise direction, but the vortex axis was seen to be located too high above the wing. Furthermore, the suction peak on the wing's surface was seen to be too low.

A follow-up study [Görtz *et al.*, 1999] revealed that details of the flow, such as the axial component of velocity of the fluid entrained in the vortex core or the surface pressure distribution, are very

sensitive to mesh topology and mesh fineness at the apex and the leading edges. This result raised the question of how an "optimum grid" should look. Due to a lack of meaningful experimental data at that time, it could not be determined what kind of velocity profile was representing the experimental flow conditions.

In order to clarify these open questions, two further numerical studies were initiated. The first [de Try, 1999] demonstrated that better agreement with the experimental data can be achieved for the pressure suction peak when the wind tunnel walls are modeled. However, the wind tunnel walls appeared not to have any significant influence on the location of the vortex core axis in the direction normal to the wing's surface.

The second study [Malmlöf, 2000] investigated the effect of mesh topology, block layout, and mesh singularities on convergence rate, surface pressure distribution, and axial velocity profile. When avoiding a polar singular line in the computational mesh at the apex by modeling a so-called "TV-screen" block, the convergence rate was seen to improve. The best agreement between experimental and computed surface pressure distribution was achieved on an embedded conical (EC) grid with the drawback that the axial velocity profile was inaccurate. The supposedly correct velocity profile was computed only on one out of seven different meshes featuring an HH-type topology with refined apex and leading edges. The leading-edge geometry was seen to have a minor effect on the pressure distribution, the aerodynamic coefficients, the breakdown location, and the maximum axial velocity on the vortex core axis, whereas it proved to have no influence on the type of axial velocity profile.

Recently, a simple wind-tunnel wing-body configuration was modeled and meshed using the commercial mesh generator ICEM CFD Hexa, which is available on PDC's computers. This model is used in the wind-tunnel lab of the aerodynamics class at the Department of Aeronautics at KTH to demonstrate the aerodynamic characteristics of delta-wing/body configurations at low Mach numbers and high angle of attack. The model consists of a cylindrical body with a von Karman nose and a tapered tail. The original wing-tunnel model has a symmetrical wing profile. Here, the wing was modeled without thickness because of the insignificant influence of the wing thickness on the aerodynamics at high angle of attack.

In the process of generating the mesh, special attention was paid to avoid singular lines and skewed cells at the wing apex, and to assure that the mesh lines are orthogonal to the wing surface. For the Navier-Stokes computations a large number of grid points were placed in the viscous layer near the solid surfaces in order to resolve these flow regions properly. An adequate density of grid points was placed in regions where large gradients are expected, that is, at the leading edge of the wing, from which the free shear layer emanates. The resulting 20-block mesh is shown in the symmetry plane and in the clip-plane at the trailing edge in figure 5.16. Early results computed on this mesh show excellent agreement with experimental data for all integrated aerodynamic coefficients. Further studies have to show if this mesh also solves the problems encountered on the previously generated meshes with singularities and skewed cells.

Further studies have to show if this mesh also solves the problems encountered on the previously generated meshes.

Outlook

Parallel to the ongoing work on finding an "optimum mesh," work at the Department of Aeronautics at KTH will focus on further investigating the influence of numerical parameters on the solution. Once these parameters have been identified, delta wings in pitching motion will be simulated in order to simulate time-dependent phenomena such as hysteresis, wing rock, *etc.*

Recently, NSMB has been extended to handle patched grids. Using patched grids, grid points can be clustered in regions of interests. This possibility will be used to refine the wing-body grid in the vortical flow regions. For cases featuring vortex breakdown, the grid will be refined near the point of breakdown in order to resolve the small-scale details of the flow.

Finally, a complete fighter-type configuration will be simulated at high angle of attack.

6.2 Catalytic Combustion of Gasified Biomass in Gas Turbines

Juergen Jacoby
Department of Energy Technology, KTH

Gasified biomass has become an attractive fuel source for energy production during the last decades as it has approximately no net contribution of carbon dioxide to the earth atmosphere. Catalytic
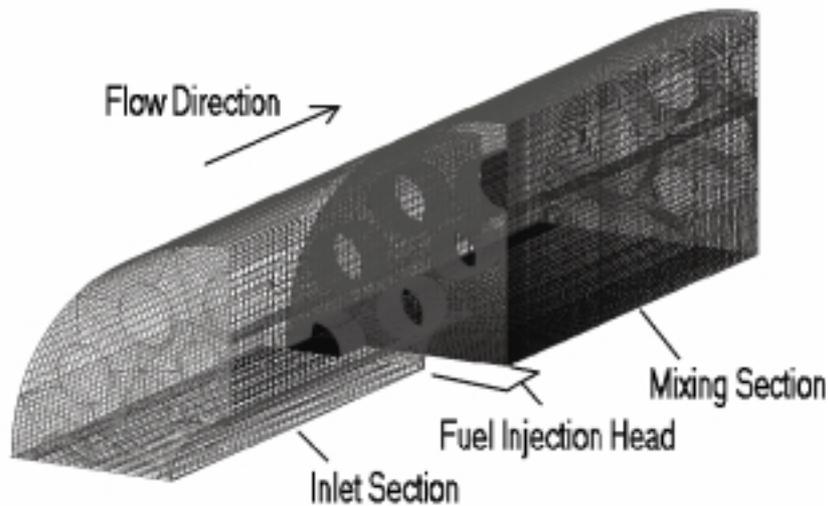
combustion, on the other hand, has the potential of reducing combustion emission drastically. A combination of these two features clearly shows advantages. Catalytic combustion reduces the activation temperature, hence formation of thermal nitrogen oxide can be completely avoided. Fuel-bound nitrogen oxide and unburned hydrocarbons in the exhaust gases are only present at ultra-low levels. However, catalytic combustion of gasified biomass is still in the very beginning of development and needs further investigation in the future.

A cold flow test rig has been designed and constructed to investigate and optimize the velocity flow field and the mixing process of fuel and air. Results obtained from this test rig are implemented into the design of a combustion test facility.

The cold flow test facility allows velocity field measurements in the mixing section upstream from the catalytic section. Static pressure taps monitor the pressure drops.

The cold flow test facility allows velocity field measurements in the mixing section upstream from the catalytic section.

The flow field in the mixing zone has also been studied numerically. These calculations show agreements in the expansion of a recirculation zone downstream from the fuel injection. 3D steady-state calculations were performed using the k-ε turbulence model. The mesh for these calculations is shown in figure 6.1.

Numerical investigations were performed to investigate the risk of auto-ignition inside the fuel injection geometry and to have numerical data for comparison with experimental results. Struc-

Figure 6.2. A mesh of one air passage of the fuel injection.
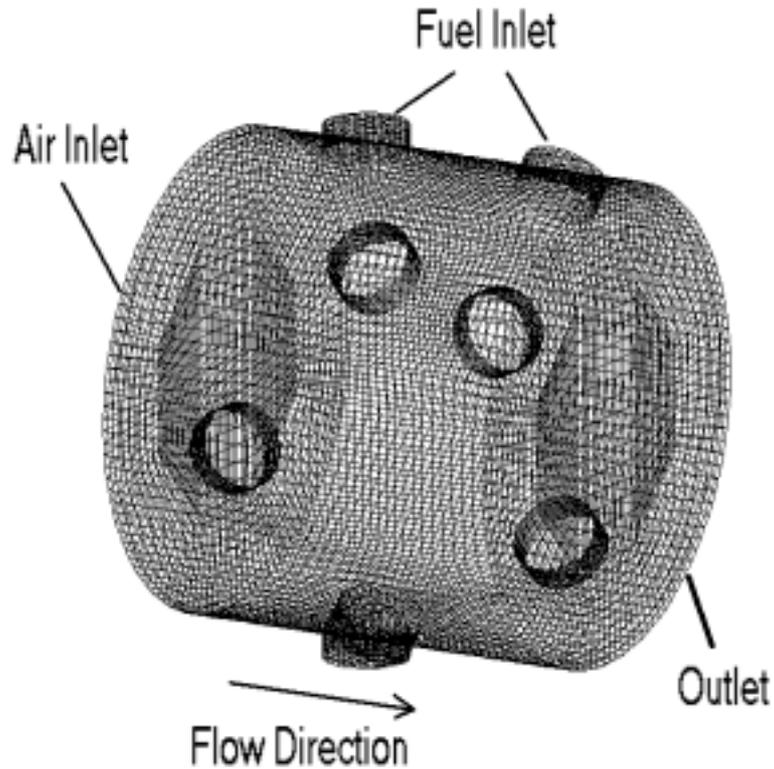
tured, body-fitted grids were set up. Turbulence was modeled using the k-ε turbulence model. The mesh for these calculations is shown in figure 6.2. Steady-state, incompressible and isothermal 3D calculations were carried out for the non-reacting flow. A seven-step kinetic reaction scheme for turbulent hydrogen combustion has been applied for investigating auto-ignition in the reactive flow. These calculations show no ignition phenomena.

The Kallsup system at PDC has been used for these investigations; it is the only system with the commercial CFD solver CFX 4.1 installed. Kallsup was solely used for solving the problem. Pre- and post-processing was always done on different machines. The typical work procedure is given below:

- Define the geometry using the CFX 4 pre-processor on a DEC Alpha.

- Edit the source code using the CFX 4 editor or any other editor; done on a PC or on a DEC Alpha.

- Transfer all necessary files to Kallsup.

- Run the CFX 4.1 flow solver, usually in batch mode by submitting jobs to NQS.

- Transfer output files to a PC and convert to the Windows NT format.

- Visualize the results using a post-processor running under Windows NT.

Because a Windows NT license for CFX 4.2 is now available at the Department of Heat and Power Technology, calculations are preferably performed on a PC. This has the advantage of saving time by eliminating the need for file transfers to and from the Kallsup system, simplifying correcting mistakes in the source code and avoiding the need for re-submission to NQS, and eliminating the need for converting the CRAY binary format. Furthermore, an on-line display of the quality of the solution is only possible if the solver is running in the CFX environment, which is not the case on Kallsup. However, as two users share one license, it can happen that a long calculation (> 15 hours) is submitted to Kallsup in order not to block the license for the second user. Differences between the CFX versions 4.1 and 4.2 do limit this dual resource use, however.

6.3 Hammershock Calculations in the Air Intake of JAS 39 Gripen, Using Dual Time Stepping

Anders Ytterström
Department of Numerical Analysis and Computer Science, KTH
Emil Axelson
Saab, Linköping

Introduction

Time-accurate calculations are of great importance, because many flow problems are of a time-dependent nature. The largest problem with time-accurate calculations is the very large computation time for realistic cases.

Explicit Runge-Kutta time stepping, using global time steps, is the traditional method for time-accurate calculations. The global time step usually becomes very small, due to stability restrictions,

because the global time step is chosen as the smallest local time step in the total mesh. Larger time steps can be used with an implicit time-stepping scheme, which has a much larger stability region, compared to the explicit Runge-Kutta scheme. However, solving the system of equations resulting from a truly implicit scheme is usually very demanding regarding both CPU time and memory requirements.

The dual time-stepping method, suggested by Jameson [Jameson, 1991], uses existing algorithms in Navier-Stokes solvers, including convergence rate acceleration methods like local time steps, multigrid, *etc.*, to solve the system of equations resulting from an implicit formulation of the Navier-Stokes equations.

The NSMB *Code*

Numerical Scheme

The NSMB code solves the Navier-Stokes equations on multi-block structured grids. The Navier-Stokes equations are discretized using either a second-order central scheme or an upwind scheme with TVD-limiters, both using cell-centered finite-volume formulation. The equations are integrated in time using either explicit Runge-Kutta time stepping, or the implicit LU-SGS scheme [Yoon and Jameson, 1986, Klopfer and Yoon, 1993, Weber, 1996].

Dual Time Stepping

The idea behind the dual time-stepping technique is to have an outer time-stepping loop for a real-time–accurate time step using a fully implicit scheme, and also to have an inner time-stepping loop, with a fictitious time step, to solve the system at each real time step. Local time steps, multigrid, and other techniques for acceleration of convergence can be used in the inner loop to converge the solution to a steady state within each real time step. This implementation follows the technique presented by Jameson [Jameson, 1991].

The Navier-Stokes equations are given in the following discrete form as a set of ordinary differential equations:

$$\frac{d}{dt}\left(VW\right) + R\left(W\right) = 0, \tag{6.1}$$

where V = cell volume and W = state vector.

If equation (6.1) is approximated with an implicit Backward Difference Formula (BDF) of second-order accuracy, it becomes:

$$\frac{3}{2\Delta t}\left[V^{n+1}W^{n+1}\right] - \frac{2}{\Delta t}\left[V^{n}W^{n}\right] +$$
$$\frac{1}{2\Delta t}\left[V^{n-1}W^{n-1}\right] + R\left(W^{n+1}\right) = 0 \qquad (6.2)$$

A modified residual, $R^{*}\left(W\right)$, is defined using the above discretization in time, as

$$R^{*}\left(W\right) = \frac{3}{2\Delta t}\left[V^{n+1}W\right] - \frac{2}{\Delta t}\left[V^{n}W^{n}\right] +$$
$$\frac{1}{2\Delta t}\left[V^{n-1}W^{n-1}\right] + R\left(W\right) \qquad (6.3)$$

and the system to solve is $R^{*}\left(W\right) = 0$.

A new system of ordinary differential equations, similar to Equation (6.1), is formulated using the modified residual and in a fictitious time, t^{*}:

$$\frac{d}{dt^{*}}\left(VW\right) + R^{*}\left(W\right) = 0 \qquad (6.4)$$

Equation (6.4) is marched to steady state in the fictitious time t^{*}, using any convergence-acceleration method implemented in the flow solver, with the slightly modified residual in Equation (6.3).

Inviscid Hammershock Calculation of a Full 3D Air Intake

Hammershock is a phenomenon occurring in air intakes when the engine is stalling. This results in a sudden pressure rise at the engine entrance, which results in a sharp pressure rise and sometimes even a shock moving in the upstream direction through the intake duct. It occurs usually for certain, low, throttle settings at supersonic speeds. The pressure rise could be as high as 3 times the static pressure achieved in the steady-state case, which is often the design load in an air intake duct. It can also give a large pressure rise at other parts of the aircraft immediately in front of the intake when the shock comes out of the duct.

Mesh and Flowcase Description

Viscosity is considered to have only a minor impact on the flow and is far too expensive for a time-accurate calculation of a complex

Figure 6.3. Pressure as a function of time in different points in the intake duct of JAS 39 Gripen.

Timedependent static pressure in intake duct of JAS 39 Gripen, L=6.8 m

A time-accurate calculation is performed using a time-dependent static pressure, at the intake outflow, simulating an engine stall.
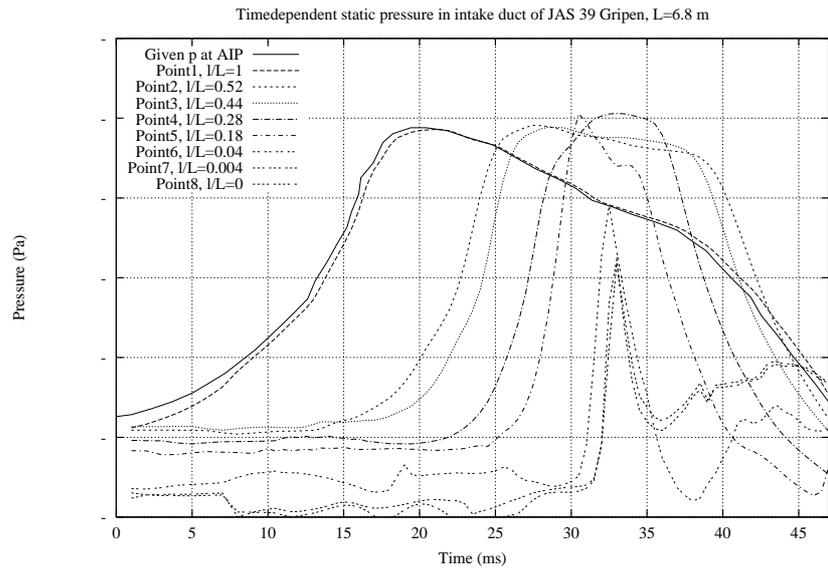
3D geometry as the JAS 39 Gripen. There are 83 blocks in the mesh with a total of 1,707,938 cells. The complexity of the mesh and geometry gives very small cells in some regions, which will result in very small Δt for the Runge-Kutta time stepping.

First, a steady-state solution is obtained using a constant static pressure as the intake duct outflow condition. Then, a time-accurate calculation is performed using a time-dependent static pressure, at the intake outflow, simulating an engine stall. The pressure pulse shown as a solid line in figure 6.3 resembles the behavior of the static pressure when the engine stalls.

When the CFL number is set to be 1.0, the explicit Runge-Kutta scheme gives a time step of $\Delta t = 10^{-10}$ s, which means that a total simulated time of 0.047 s would take 470 million time steps. On an eight–R8000-processor SGI Power Challenge, this would demand 685 CPU years.

For the dual time stepping, $\Delta t = 10^{-5}$ s was considered to give an accurate enough result.

Time-Accurate Calculation

Each outer time step demanded an average of about 30 internal iterations, ranging from 10 to 200, to reach 2 decades of convergence, which means that 0.047 s of simulated time would demand
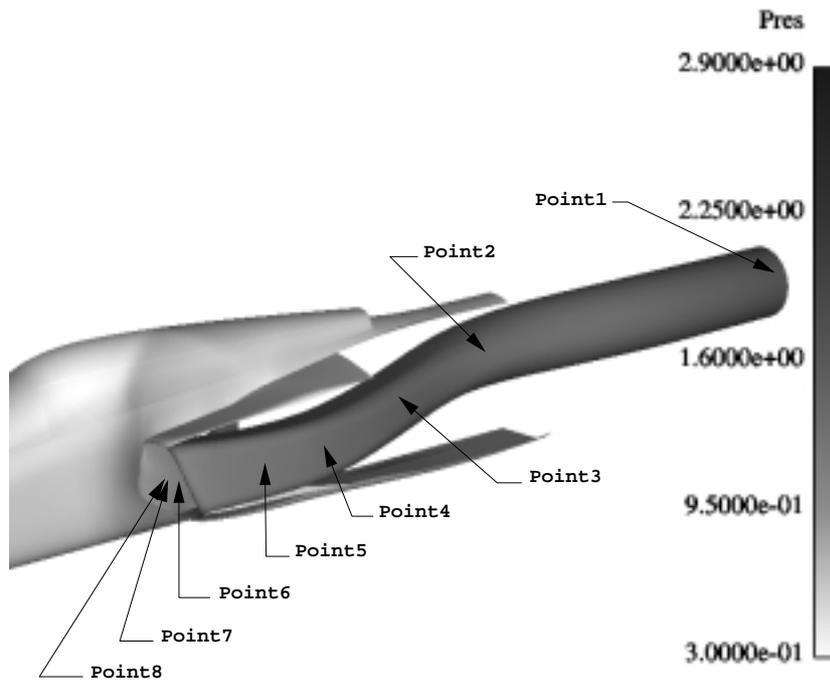
Figure 6.4. Locations of the points used in previous figure in the intake duct.

76 days of CPU time. Even if the CPU time is reduced by more than 3,000 times, compared to the classical Runge-Kutta scheme, it still takes more than 2.5 months of CPU time on an eight–R8000-processor SGI Power Challenge.

Most of the time-accurate calculations were performed on 1 processor of a Fujitsu VX/3 at PDC, KTH, which reduced the cputime to about two weeks for a simulated time of 0.047 s.

Results

Figure 6.3 shows the pressure as a function of time at different points in the intake duct. An overview picture of the point locations can be seen in figure 6.4. The slope of the pressure rise increases as the hammershock travels towards the duct entrance. Maximum relative increase in static pressure is achieved in point 4 (l/L=0.28), where the static pressure is close to 2.5 times higher than the steady-state condition for this case.

6.4 Large Eddy Simulations of the Flow around an Airfoil

Simon Dahlström, Lars Davidson
Department of Thermo and Fluid Dynamics, CTH

Introduction

This work is part of the ongoing Brite-Euram project called LES-FOIL (Large Eddy Simulations of Flows around Airfoils). This project is coordinated by Chalmers University of Technology (CTH), see `http://www.tfd.chalmers.se/~lada/projects/lesfoil/proright.html`. One of the main objectives of the project is to demonstrate the feasibility of LES for simple 2D airfoils. The test case chosen is the flow around the Aerospatiale A-airfoil where the angle of attack equals 13.3° and the chord Reynolds number is 2.1×10^6.

One of the main objectives of the project is to demonstrate the feasibility of LES for simple 2D airfoils.

This is a challenging case for LES because of the high Reynolds number and also because of the different flow situations around the airfoil, including transition from the laminar flow near the leading egde and separation near the trailing edge. Even at the (from an aeronautical point of view) low Reynolds number, a wall-resolved LES is too expensive. The use of approximate boundary conditions in the near wall region is necessary, and a good method of prescribing and controlling the transition is needed.

Method

The code that is used is a finite volume Navier-Stokes solver called CALC-BFC [Davidson and Farhanieh, 1992]. The solver is based on structured grids and the use of curvi-linear boundary fitted coordinates. Also, the grid arrangement is colocated; and for the pressure-velocity coupling the PISO algorithm is used together with the Rhie and Chow interpolation method [Rhie and Chow, 1983]. The code is parallelized for 3D flows using block decomposition and the message-passing systems PVM [Nilsson, 1997, Nilsson and Davidson, 1998] and MPI. As a subgrid scale model (SGS model), the Smagorinsky model is used; and the time step is set to 3×10^{-4} time units giving a maximum CFL number of 1.3, where the time unit is based on the chord and the free stream velocity. For the advancement in time, the Crank-Nicolson scheme is used, and the momentum equations are discretized in space using second-order difference schemes.

Number of processors	8	16	32
Sun, PVM, socket based	48s	38s	36s
Sun, PVM, shared memory based	24s	(12s)	(6s)
Sun, MPI	24s	-	-
IBM SP, PVM	12s	-	-
IBM SP, MPI	-	5.4s	2.8s

Table 6.1. Elapsed time per time step.

Spatial Discretization Schemes

When the momentum equations are discretized in space using the central difference scheme (CDS), many non-physical oscillations are present, all over the computational domain. This is not surprising, because the scheme is known to produce wiggles or odd-even oscillations when the resolution is too poor. In order to suppress the non-physical oscillations upstream of the airfoil and upstream of the transition region, a bounded second-order upwind scheme is applied in this region. In the transition region, the upwind scheme is gradually replaced with the central difference scheme; and when the central difference scheme is fully active, the flow becomes turbulent. In this way the transition is prescribed by the upwinding. The stabilized field upstream of the airfoil also has an effect on the computational domain downstream of the transition region. As an additional result, the non-physical, odd-even oscillations are dampened in the area where the central difference scheme is applied. Moreover, the maximum CFL-number decreases from 1.3 to 0.6, compared to when the central difference scheme is used and the global iterations per time step decrease from 3 to 2.

The upwind scheme is gradually replaced with the central difference scheme; and when the central difference scheme is fully active, the flow becomes turbulent.

Speedup Results

The initial computations were done on a C-grid consisting of $320 \times 64 \times 31$ cells (= 701316 computational nodes) on a 64-processor Sun Enterprise 10000 at CTH and on the IBM SP at PDC at KTH. Table 6.1 shows the elapsed time per time step.

The computational domain is decomposed into 8, 16, and 32 subdomains. The number of global iterations does not seem to differ between these block decompositions. Two different versions of the message-passing library PVM are available on Sun platforms: a shared-memory–based PVM and a socket-based PVM. When 8

processors are used, the shared-memory–based PVM is twice as fast as the socket-based PVM. The simulation of one time unit ($T = c/U_\infty$) requires about 180 CPU hours. The solution is advanced about one time unit per day. The IBM SP is faster. The simulation of one time unit requires about 90 CPU hours. With MPI and 32 processors, the solution is advanced 8 time units per day. On this computer, an approximately linear speed-up is obtained between 8 and 32 processors.
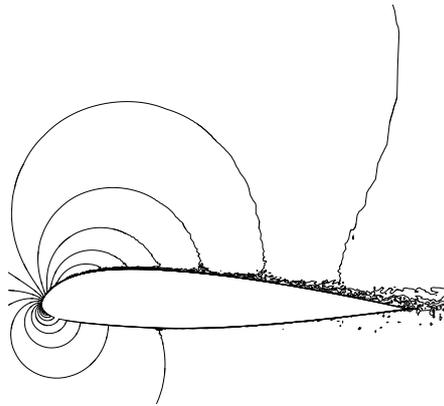
Insufficient Resolution

Although the non-physical oscillations are suppressed and dampened upstream and downstream of the transition region, respectively, the present grid is far too coarse to allow for a useful LES. The poor resolution just downstream of the transition region makes the transition process unnatural, and none of the present computations capture the separation region close to the trailing edge. A new mesh has been generated. The mesh consists of 720×65 nodes, more than twice as many nodes in the i-direction (the direction around the airfoil in the C-mesh). The resolution on the suction side of the airfoil is now reasonably good in the streamwise direction. In the wall-normal direction, the distance from the wall to the first node y^+ is less than 40, and wall-functions based on an instantaneous log-law have been used. The extension in the spanwise direction is divided into 32 cells, which results in a mesh that consists of approximately 1,600,000 computational nodes.

Results and Future Work

The computations on the new mesh are run on the IBM SP at KTH, initially on 32 processors. A contour plot of the instantaneous resolved velocities in the chord-direction is shown in figure 6.5. The elapsed time per time step is $6\,s$, and the solution is advanced more than 4 time units per day. The finer resolution and the wall-functions do improve the results, but the transition and separation processes are still difficult to capture. The resolution has to be finer in the wall-normal direction, especially in the separation region where the very thin separation bubble has to be resolved. Also, the transition process and the behavior of the SGS model and the CDS in that region need further examination.

6.5 Modeling Radiative Heat Transfer in a CFD Code for General 3D Geometries

Thomas Badinand[1]
Department of Heat and Power Technology, KTH

Introduction

Radiative heat transfer is the transport of heat by electromagnetic waves, as opposed to molecular contact in convection. Since it is proportional to the fourth power of the temperature, it is important when high temperatures are encountered, as in combustion, nuclear reaction, and space reentry vehicles.

For jet engines, radiative heat transfer is important in the heating of walls in combustion chambers and in the prediction of the flame temperature. Also, the radiative field of the exit nozzle is a target for weapons. In this case, thermal radiation is important in predicting the right temperature in combustors (and then to select an appropriate material) and in decreasing the emission of NO_x, which is a strong function of the flame temperature. Finally, prediction of the radiative field at the exit of an aircraft is vital for its survivability.

This project's aim is to develop a model into an existing CFD

---

code (VOLSOL, developed by Volvo Aero Corporation) to model radiative heat transfer for gray gases for general 3D geometries. The coupling with flow calculations will be done so that the influence of radiation on the flow field can be studied. As a second step, the model will be extended to non-gray gases whose properties vary with wavelength. This should lead to the computation of the spectral radiation field at the exit of a jet engine.

This should lead to the computation of the spectral radiation field at the exit of a jet engine.

Approach Used

The computation of radiative heat transfer is based on the radiative transfer equation (RTE), which states the conservation of energy applied to a monochromatic pencil (bundle) of radiation propagating in an emitting, absorbing, and scattering medium. The primitive variable of the equation is the radiative intensity, which is the energy flow per unit solid angle per unit area normal to the direction considered. It is a function of five/six variables: three for position, two for direction, and eventually one for the wavelength. This makes the resolution of the RTE a real challenge. To couple this calculation with a flow solver, the divergence of the radiative heat flux appears as a source/sink term in the energy equations.

A recent way of solving the RTE is the finite volume method. It is based on the discretization of the RTE in space and direction. This means that a mesh is created for the space domain, and all directions are classified in a finite number of solid angles, fixed in space. In each volume, all variables are considered constant and uniform, and for each solid angle, the directional part of the intensity is considered constant and uniform. This method allows the use of the same spatial mesh for flow calculations and radiative calculations, which enables a coupling of the two. This method has been applied to axi-symmetric geometries using PDC resources and presented by Eklund, Badinand, and Fransson [Eklund *et al.*, 1988].

Results Obtained

The first step of the project, computing radiation for gray gases, has been implemented inside the code and coupled to it. The geometry used was a cube of $20 \times 20 \times 20$ cells (see figure 6.6), and three in the polar direction and five in the azimuthal direction.
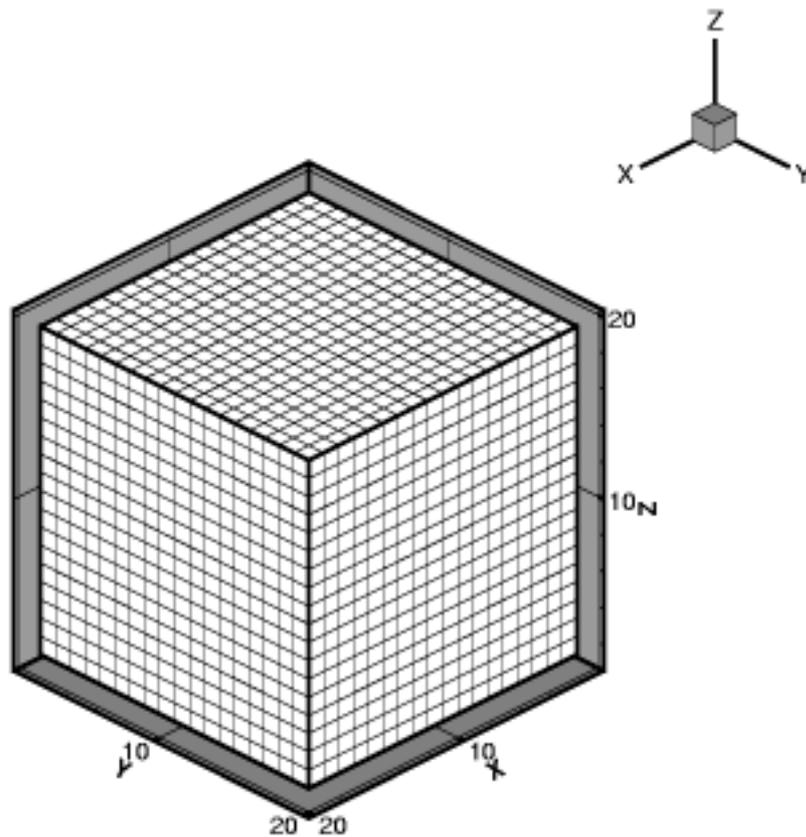
Figure 6.6. A mesh used for a 3D cube consisting of $20 \times 20 \times 20$ nodes.

The boundaries were cold black walls $(0\,\mathrm{K})$, and the medium had a uniform temperature of $300\,\mathrm{K}$. The intensity obtained for different directions is presented in figure 5 on page 69. Figure 5 on page 70 presents the computation of the divergence of the heat flux, which is a source term in the energy equation. Finally, by coupling with the flow calculations, the temperature in the medium is changed due to radiative heat transfer. Figure 5 on page 70 presents the temperature obtained after seven iterations, the temperature in the medium being at an initial temperature of $3000\,\mathrm{K}$.

Need for HPC Resources

The computation took $1.57\,\mathrm{s}$ on one node of an IBM SP for the radiation model. Typical 3D meshes consist of around 500,000 nodes, and would need 5×10 directions resulting in 25,000,000 variables. Moreover, for non-gray gases, the intensity should be

computed for each spectral band. This kind of computation would be impossible on regular computers due to the computational and memory requirements.

6.6 Sensitivity to Physical and Numerical Modeling in Navier-Stokes Simulations

Ubaldo Cella
Aerospace Department, Politecnico di Milano
Arthur Rizzi
Department of Aeronautical Engineering, KTH

Abstract

The NSMB code (Navier-Stokes Multi-Block) solves the fully coupled system of equations simultaneously using a cell-centered finite-volume approach. This note assesses the sensitivity to some turbulence models and numerical schemes implemented in NSMB when computing two test cases in standard mode, that is, without tuning the code to these two cases. The cases are

1. subsonic flow around the MS(1)-0313 airfoil, and

2. transonic flow around the ONERA M6 wing, using various combinations of models (algebraic Baldwin-Lomax or Granville, one-equation Spalart-Allmaras or the two-equation $k - \epsilon$ model of Chien) together with a numerical scheme of either the second-order central or third-order Roe upwind type.

Introduction

The NSMB code (Navier-Stokes Multi-Block) is a solver using a cell-centered finite-volume approach [Vos *et al.*, 1998]. Previous calculations tested the ability of NSMB to predict the evolution of flow around complex geometry, ranging from a two-element aerofoil [Vos *et al.*, 1998] to a wing-fuselage-pylon-nacelle (AS28G) configuration [Gacherieu and Weber, 1998]. The aim of this work is to investigate the performance of several physical-model/difference-scheme configurations of the code by evaluating and comparing their ability to predict various aerodynamic phenomena, (shock-wake structure, flow separation, airfoil stall), as measured against the available experimental data. Two specific test cases have been investigated in this paper:

- The 2D subsonic flow around a NASA Medium Speed aerofoil MS(1)-0313. The drag polar as well as the $Cl - \alpha$ and $Cm - \alpha$ curves computed with different models are compared with the experimental data available for this tested configuration [McGhee and Beasley, 1979]. The aerofoil is used in the Saab 340 and Saab 2000 aircraft.

- The 3D transonic flow around the ONERA M6 wing. Wind tunnel data from this wing [Schmitt and Charpin, 1979] have constituted a knowledge-base for both computer program assessment and for understanding various flow phenomena like shock wave/boundary layer interaction or flow separation [Vatsa, 1987] [Muller and Rizzi, 1990] at high Reynolds number.

Several Navier-Stokes calculations have been performed for each test case. Different turbulence models have been applied together with the central and upwind numerical schemes: algebraic models (Baldwin-Lomax [Baldwin and Lomax, 1978] and Granville models), a one-equation Spalart-Allmaras model, and a two-equation $k - \epsilon$ model of Chien [Cella, 1998]. Turbulence models can be categorized depending on the number of differential equations needed in addition to the Reynolds Averaged Navier-Stokes equations and the Boussinesq hypothesis [Tulapurkara, 1997].

Different turbulence models have been applied together with the central and upwind numerical schemes.

The algebraic turbulence models neglect the turbulent kinetic energy terms and provide very simple and robust models whose implementation is easy, but of limited accuracy. The one-equation turbulence model solves a transport equation for the eddy viscosity. The transport equations for the density, momentum, and energy are the same as for the algebraic turbulence model [Spalart and Allmaras, 1992]. The $k - \epsilon$ model requires the solution of transport equations for the turbulent kinetic energy k and the turbulent dissipation ϵ. The model is typically a "low Reynolds number" model and solves an equation for the isotropic component of the turbulent dissipation.

For the spatial discretization of the system of equations, NSMB uses either the central or an upwind type of numerical scheme to calculate the inviscid flux terms, but it uses only the central for the viscous flux terms [Vos and *et al.*, 1998]. This code is homogeneous in the sense that the same spatial scheme is applied to both the mean-flow and turbulent transport equations, and it is fully coupled in the sense that the time integration scheme

advances the complete system at each time step. In contrast to this, so-called segregated solvers apply different spatial schemes to the different equations and they might advance the mean-flow in time while holding the turbulent transport frozen, or vice-versa— all for the purpose of increasing robustness of convergence.

NASA MS(1)-0313 Airfoil

This aerofoil has been optimized for a high maximum lift coefficient in turbulent flow. This provides good climbing and landing performance, although the drag at higher speed is quite high due to the limited extent of laminar flow. The aerofoil is designed for a $Cl_{cruise} = 0.3$, $Re = 14 \times 10^6$, and $Mach = 0.72$. For practical reasons the trailing edge thickness is finite, being $0.66\,\%$ of the chord. The experimental data come from the tests performed in the Low Turbulence Pressure Tunnel (LTPT) at NASA (Langley) in 1979 by R. McGhee [McGhee and Beasley, 1979]. The configuration analyzed in this paper is $Re = 6 \times 10^6$ and $M_\infty = 0.15$. The transition point was fixed on both lower and upper surface at $7.5\,\%$ of the chord as for the experimental configuration.

Computational Domain

The grid (figure 6.7) used is a C-Mesh generated at Saab using the ICEM CFD grid generator MULCAD. The total number of nodes is 52,425. The number of cells across the blunt trailing edge thickness is 40. The distance from the wall to the first cell center is set to satisfy at least $y^+ \leq 2$, and there are approximately 20–30 gridpoints within $y^+ < 100$. The farfield boundaries are placed 10 chord away from the nose of the aerofoil.

Physical and Numerical Models Tested

Table 6.2 summarizes the turbulence models and the numerical schemes that were used in the calculations.

Solutions were obtained from initial conditions from either the free stream values or the converged solution at another value of α.

The last column in the table shows the range of incidence angles for which the computation converged using standard parameters for the implicit LU-SGS [Yoon and Jameson, 1986] (Lower-Upper Symmetric Gauss-Seidel) time stepping. All solutions were obtained from initial conditions from either the free stream values or the converged solution at another value of α. The one-equation
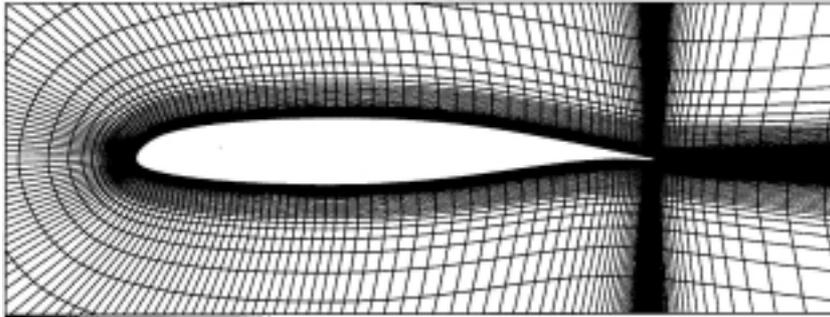
Figure 6.7. The MS(1)-0313 computational domain.

Block number	Block size (cells)
1	$44 \times 56 \times 2$
2	$184 \times 56 \times 2$
3	$96 \times 44 \times 2$

Turbulence model	Numerical scheme	Solution obtained(α)
Baldwin-Lomax	Central	$-2.9°$, $5°$, $11°$, $14°$, $16°$
	Upwind third-ord. Roe's	$-2.9°$, $5°$, $11°$, $14°$
Granville	Central	$-2.9°$, $5°$, $11°$, $14°$, $16°$, $16.5°$, $17°$
	Upwind third-ord. Roe's	$-2.9°$, $5°$, $11°$, $14°$
Spalart-Allmaras	Central	$-2.9°$, $5°$, $11°$, $14°$, $16°$, $16.5°$
model of Chien	Central	$5°$
	Upwind third-ord. Roe's	$5°$

Table 6.2. NSMB model-scheme configurations analyzed and range of solutions obtained.

Central scheme alpha=16

- 1 eq. Spalart-Allmaras   -- 0 eq. Baldwin-Lomax   .- 0 eq. Granville
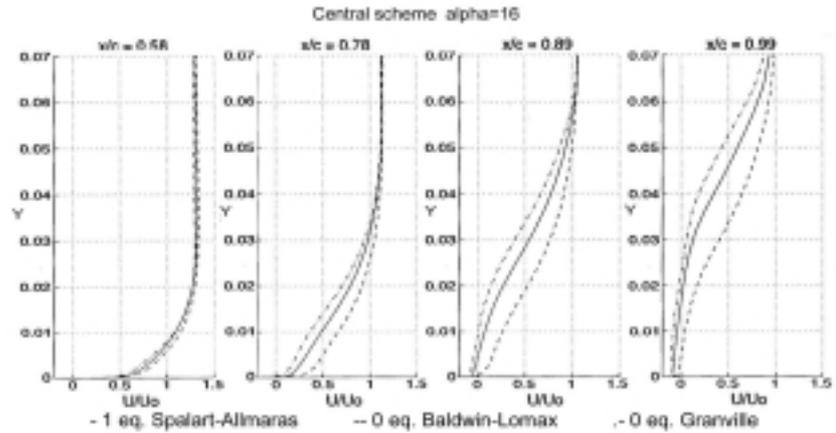
Spalart-Allmaras model using the central scheme showed the best convergence behavior. All of the solutions needed a very large number of iterations to converge to a residual lower than 10^{-3} (order of 60,000 iterations for the central scheme and 30,000 for the upwind).

Analysis of Solutions

Central scheme. The central scheme is the only configuration able to predict the stall of the airfoil. A low residual has been reached in almost all the calculations (order of 10^{-4}). At $\alpha = 11°$, the differences between the turbulence models begin to be evident. The Granville model predicted a much softer stall behavior than the Baldwin-Lomax one, which predicted a very sudden stall. This is due to a different behavior of the flow in the boundary layer. Figure 6.8 shows the influence of turbulence models on the velocity profile in the boundary layer. The Baldwin-Lomax model predicted the highest velocity profile. The flow separates later, and the stall is sudden. The Granville, and in particular the Spalart-Allmaras model, showed a good prediction of the influence of the viscous effect on the shape of the $Cl - \alpha$ curve. All the models underestimated the Cl_{max} and the $\alpha_{Cl_{max}}$. The 0-equation Baldwin-Lomax model predicted the highest Cl_{max}, but like the other models, converged only at $\alpha = 16°$. In none of the cases has it been possible to compute values after the stall (as seen in the experiment).

Third-order Roe upwind scheme. The upwind scheme failed remarkably in predicting the Cl_{max} and the stall behavior in both the 0-equation models. All the coefficients from this solution differ completely from the experimental results. This is due to an anomalous pressure distribution prediction close to the nose of the aerofoil. It is a little better in the drag coefficient estimation than the central scheme for low angles of attack. Figure 6.9 compares the solutions obtained with the two numerical schemes.

ONERA M6 Wing

Even if the experimental data available for this wing are not complete, they have been taken as a reference for comparing turbulence models and numerical schemes in a number of Navier-Stokes codes. The surface pressure on the M6 Wing was measured in the ONERA S2MA wind tunnel [Schmitt and Charpin, 1979]. Extensive pressure distribution data for several spanwise stations were measured over a wide range of Mach numbers and angles of attack, but no aerodynamic coefficients were reported. Information on the boundary layer has been found [Schmitt *et al.*, 1983], where three velocity profiles for three points of the wing were taken to be compared with our solutions.

Extensive pressure distribution data for several spanwise stations were measured over a wide range of Mach numbers and angles of attack.

The configuration analyzed in this paper is a transonic flow at the following conditions: $Re = 11.72 \times 10^6$, $M_\infty = 0.84$, and $\alpha = 3.06°$. The experimental Reynolds number is referenced to the mean aerodynamic chord of the wing. In the NSMB input file the Reynolds number per meter is required. The value used in the computation was $Re = 17.49 \times 10^6$, referenced to a mean aerodynamic chord of 0.67 m (slightly larger than the wind tunnel model, because the profile was extended to close it with a sharp trailing edge).

Computational Domain

The grid used was a four-block mesh designed at Saab using the ICEM CFD/CAE MULCAD grid generator. Figure 6.10 shows the dimensions of the mesh and blocks. The highest average value of y^+ is 3.02, and the total number of cells is 706,560.

Figure 6.9. Comparison of the solutions: $C_l - \alpha$ curve and drag polar.

Central scheme

-- Experimental
o 0 eq. Baldwin-Lomax
x 0 eq. Granville
+ 1 eq. Spalart-Allmaras

0 equation Granville

-- Experimental
o Central scheme
+ Upwind 3rd ord. Roe's scheme
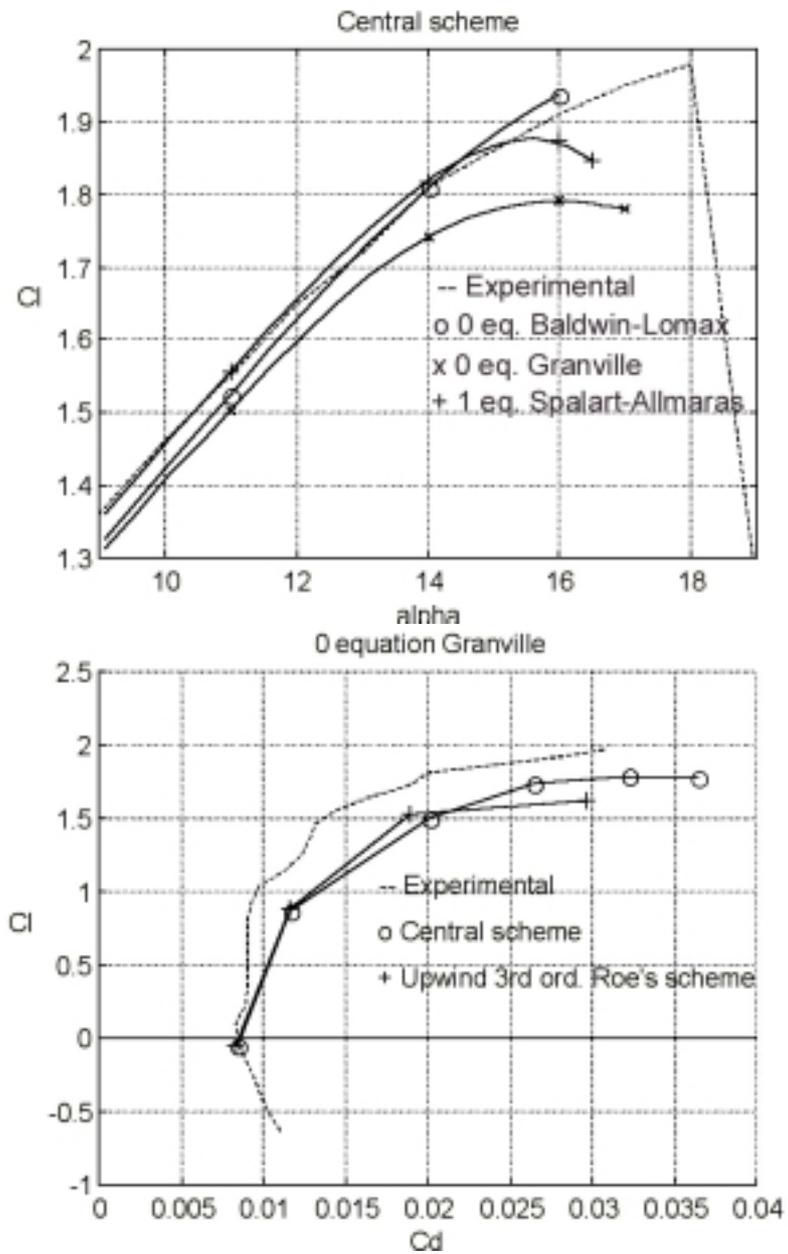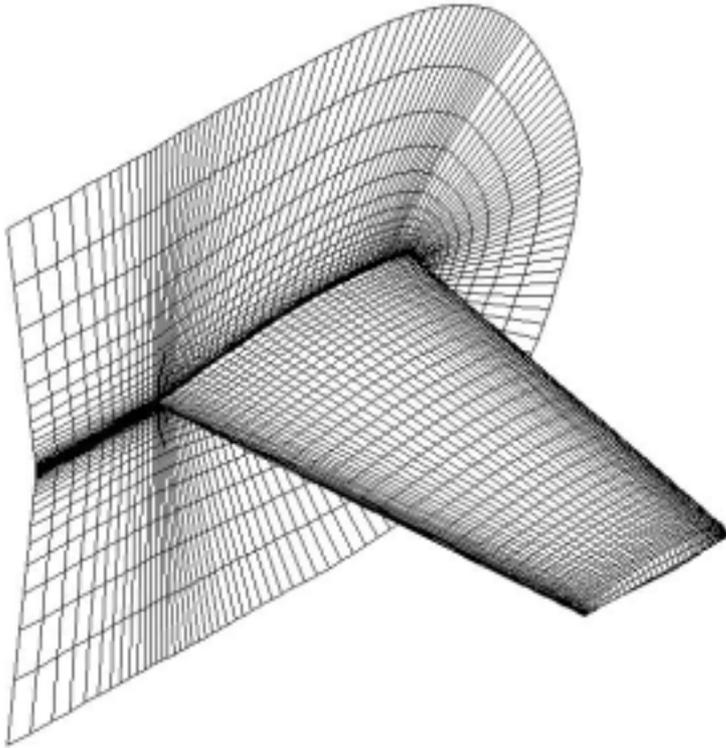
Wing planform	Swept back
Aspect ratio	3.8
Leading edge sweep	30°
Trailing edge sweep	15.8°
Taper ratio	0.562
Mean aerod. chord	$c = 0.64607$ m
Semispan	$b = 1.1963$ m

Block number	Block size (cells)
1	$60 \times 64 \times 60$
2	$32 \times 64 \times 60$
3	$60 \times 64 \times 60$
4	$32 \times 64 \times 60$

Table 6.3. M6 Wing: NSMB model-scheme configurations analyzed and aerodynamic coefficients predicted.

Turbulence model	Numerical scheme	Cl	Cm	Cd
0-equation Baldwin-Lomax	Upwind 3rd-ord. Roe's	0.2664	-0.1892	0.0170
0-equation Granville	Upwind 3rd-ord. Roe's	0.2629	-0.1854	0.0167
1-equation Spalart-Allmaras	Central	0.2610	-0.1844	0.0180
2-equation Chien	Upwind 3rd-ord. Roe's	0.2504	-0.1734	0.0182
	Central	0.2500	-0.1720	0.0179

Physical and Numerical Models Tested

The turbulence models tested in this 3D case are the same as those tested in the NASA MS(1)-0313 aerofoil case. The flow was assumed to be fully turbulent for all cases. For the 0-equation algebraic turbulence models, the upwind third-order Roe's scheme was used. A central scheme calculation was performed with the one-equation Spalart-Allmaras turbulence model. For the two-equation model of Chien, both the central and the upwind numerical scheme calculation were performed in order to have a direct comparison of the influence of the numerical scheme on the solution. The configurations studied are summarized in Table 6.3, together with the comparison of the aerodynamic coefficients predicted.

In all cases the implicit LU-SGS time integration was performed with atandard parameters. Both the two algebraic turbulence models analysed gave a very robust and fast convergence. A residual of order of 10^{-4} was easily reached already after 2,000 iterations by the Granville model, slightly less than for the Baldwin-Lomax. A residual smaller than 10^{-3} could not be reached, however, with the one-equation Spalart-Allmaras and the two-equation central scheme. Robustness with the two-equation model of Chien could be obtained only keeping the CFL number constant at 5 during all the iterations with either of the two numerical schemes

employed.

Analysis of Solutions

Comparison of the solution for the pressure coefficient distribution was done for seven stations from the root to the tip of the wing. The isobars reflect the expansion and subsequent pressure increase near the leading edge as well as the compression region over the whole wing. This results in the familiar λ pattern of the two shocks coalescing outward near the tip (figure 6.11). This λ shock is formed when a double shock on the inboard stations merges into a single (much stronger) shock towards the outward station on the wing. Thus, much stronger gradients are present in the spanwise direction under supercritical conditions.

The shock-wave/boundary-layer interaction is rather weak and not strong enough to induce separation. All the models predicted a similar pressure distribution. This is because there is no separation and no adverse gradient of any real magnitude. Algebraic models are as capable of predicting a realistic solution under these conditions as the two-equation model. A small difference is visible when comparing the solution obtained using the central scheme with the solution obtained using the upwind scheme. Better resolution of the λ shock structure is performed by the upwind third-order Roe's scheme, especially near the shock junction zone.

All the models predict quite a realistic location of the two shock waves until the middle of the wing. A small underestimation of their location occurs moving closer to the tip. The real shocks coalesced farther outboard, and the merged line toward the tip is closer to the trailing edge than the one predicted by the computed solutions. This is probably due to a too-coarse clustering of the cells in the boundary layer and not to the turbulence model. The anomalous pressure distribution on the last section of the wing is due to a non-faithful reproduction of the tip geometry by the mesh. Only two lines of cells were used in this zone. The upwind scheme needs much more CPU time than the central scheme for each iteration (about $110\,\%$ more), but needs less than half the iterations to converge to a constant value of the coefficients.

All the models predict quite a realistic location of the two shock waves until the middle of the wing.

Figure 6.11. M6 wing: chordwise pressure coefficients, 2-eq. model of Chien and third-order upwind scheme compared with experiment

Section 1 y/b =0.20

Section 2 y/b = 0.44

Section 3 y/b = 0.65

Section 4 y/b = 0.80

Section 5 y/b = 0.90

2 eq. model of Chien upwind third ord. Roe's scheme

o Experimental   x NSMB

Section 6 y/b = 0.95

Section 7 y/b = 0.99
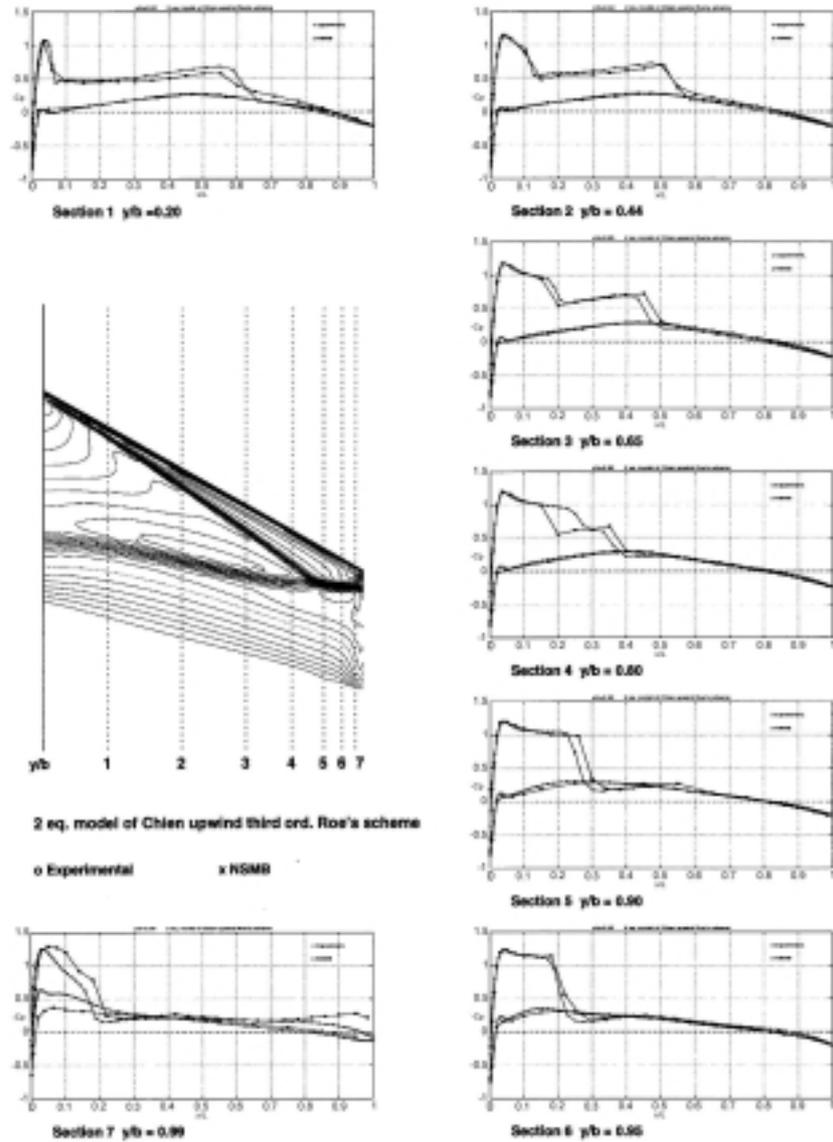
Conclusions

Study of the 3D transonic wing case together with the high-lift airfoil case, suggest the following comments about the turbulence models and the numerical schemes to be used for such types of flows.

- *Turbulence model*: The calculations performed for the wing showed that in a complete attached flow without adverse pressure gradient, the algebraic models have the same order of accuracy as the one-equation or two-equation turbulence models, which are less robust and expensive in terms of CPU time. Both the 0-equation models showed a valuable ability to predict the shock wave structure along the entire wing.

  In the 2D case, the Granville model showed good quality in predicting the characteristic curves of the aerofoil, even if in the case analyzed its convergence robustness was not so good. Both the algebraic models, however, failed remarkably in predicting the eddy viscosity distribution in the wake of the aerofoil.

  The one-equation Spalart-Allmaras model showed the best overall performance in all conditions, even if it was not possible to perform an upwind calculation with it in any of the cases. With the two-equation model, it was not possible to perform a high-lift calculation. A comparison of the accuracy of its solution was therefore not possible. For these cases, we believe that a segregated solver approach could boost robustness. In particular, applying a first-order upwind scheme to the turbulent transport equations has been suggested as a possible remedy in the future.

  Applying a first-order upwind scheme to the turbulent transport equations has been suggested as a possible remedy in the future.

- *Numerical scheme*: In the 2D calculations, the upwind, third-order Roe's scheme gave a more accurate prediction of the shock wave structure on the wing and a better estimation of the drag coefficient for low angles of attack than the central scheme. On the other hand it is not as robust for the cases of higher angle of attack.

  The central scheme showed good robustness and more realistic solutions when the flow conditions are such that the calculations have difficulties to converge (mainly high alpha). On the other hand it needs an accurate control of the artificial viscosity in order to have a comparable accuracy to the upwind calculation in the cases that are simpler to converge (mainly low alpha).

A broad guideline for the choice of a turbulence model and a numerical scheme to confront such flowfields suggests using the algebraic models in absence of adverse pressure gradients (employing the upwind scheme if stable for the configuration analyzed,) and the one-equation model in the presence of separation or complex geometry. The low stability of the two-equation models leads us to judge the one-equation model as a better candidate for a more robust solution to a complex-flow problem.

Acknowledgments

6.7 3D Numerical Modeling of Diapirism in the Earth's Crust

Alik Ismail-Zadeh
International Institute of Earthquake Prediction Theory and
Mathematical Geophysics, Russian Academy of Sciences, Russia
Igor Tsepelev
Institute of Mathematics and Mechanics, Ural Branch,
Russian Academy of Sciences, Russia
Christopher Talbot
Institute of Earth Sciences, Uppsala University
Per Öster
Center for Parallel Computers, KTH

The diapirism is a well-known geological process occurring in the Earth's crust. Understanding the geometries, kinematics, and dynamics of the diapirs is very useful to geoscientists, especially in studying crustal deformations. Although the patterns of diapirs are very complex, the basic physical phenomena of diapirs can easily be explained by the gravitational instability of a lighter layer underlying a denser one. If the interface between the two layers is disturbed, the underlying low-density rocks will move upward due to density inversion [Ismail-Zadeh and Naimark, 1996]. The growth rate of this perturbation depends on the density and viscosity contrasts, the thickness of the two media, and the boundary

conditions.

Numerical simulation of 3D time-dependent viscous flows is a field of geological fluid dynamics that requires large amounts of computational power to generate results for realistic models in acceptable time. We use a parallel solver for 3D modeling of slow viscous movements induced by gravitational instability of light layer (salt) overlain by denser ductile sediments.

Mathematically the problem is described by the Stokes' equations and transfer equations for density and viscosity. Our numerical technique is based on representing the vector potential components of the velocity (ψ_i) as weighted sums of tricubic splines defined on small supports and on the Galerkin method to obtain the unknown weights. The density (ρ) and viscosity (μ) are represented as weighted sums of trilinear functions defined on small supports. The density and viscosity transfer equations reduce to two sets of ordinary differential equations (SODE) for the weights in the density and viscosity representations, respectively. The vector potential enters the right sides of these equations solved by a fourth-order Runge-Kutta method. At each time step we solve the set of linear algebraic equations (SLAE) for weights in the vector potential representation. The result includes time-dependent velocity, density, and viscosity in the model region.

Our parallel algorithm simultaneously solves the SLAE and SODE. We typically use 16 processors of the IBM SP for our studies. The model box is $l_1 = 12$ km long, $l_2 = 12$ km wide, and $l_3 = 4$ km deep. This box is divided into $25 \times 25 \times 25$ rectangular elements.

The density ρ is represented on a $73 \times 73 \times 73$ grid, 3 times denser than a grid of supports used for representing μ and ψ_i. The total execution time for 1 time step on 16 processors is about 30 minutes.

We consider a 2-layered system at time $t = 0$: a salt layer 800 m thick at the bottom of the model is covered by sediments 3.2 km thick. The interface between salt and sediment overburden is initially perturbed by a peak of the function:

$$x_3 = 0.2 + 0.05 \, exp[-30(x_1 - x_1^0)^2 - 30(x_2 - x_2^0)^2],$$

where $x_1^0 = 0.5l_1$ and $x_2^0 = 0.5l_2$. The viscosities and densities are 10^{20} Pa s and 2.3×10^3 kg m^{-3} for the sediments and 10^{18} Pa s and 2.2×10^3 kg m^{-3} for salt. The time step Δt is defined so that a maximum displacement of mass point does not exceed a sufficient

Numerical simulation of 3D time-dependent viscous flows requires large amounts of computational power to generate results for realistic models in acceptable time.

small parameter h, that is, $\Delta t = h/u_{max}$, where u_{max} is a value of maximum velocity.

Figure 5.20 on page 71 shows the evolution of a diapir evolved from the initial perturbation in 5.5 million years (My), where the salt pillow matures into upbuilding diapir. Each panel of the figure presents a sediment/salt interface and velocity field in the model box. The shape of the salt diapir in the center of the model region closely agrees with classical cases of the Rayleigh-Taylor instability with high viscosity contrasts and a thin lower layer.

Previous research [Ismail-Zadeh *et al.*, 1998] suggested a 3D numerical approach for solving the problem, which represented all unknowns by tricubic splines. Symmetry properties of the model region, governing equations and boundary conditions relative to planes $x_i = l_i/2$ ($i = 1, 2, 3$) were used to reduce computation time. While the latter method was more accurate, much more computer capacity was needed. The new method simplifies the computations, but it also increases errors. To limit the errors, we use a grid for the density field that is denser than those for the viscosity and velocity fields.

Our parallel algorithm solves the systems both of linear algebraic and of ordinary differential equations.

Our parallel algorithm solves the systems both of linear algebraic and of ordinary differential equations. The main part of the computations is the solution of the linear system, which is solved using a direct method. Our current implementation has limited scalability beyond 16 processors due to communication issues, which we are addressing at this time.

7 Computer Engineering

7.1 Investigations of Distributed Shared Memory Software

Mats Brorsson
Department of Information Technology, Lund University

Parallel programs are generally hard to develop and the hitherto standard programming model using message passing is not making it easier. Small-scale symmetric multiprocessors (SMPs) can be programmed using shared memory as a communication paradigm; OpenMP has emerged as a new standard for parallel programming using shared memory and also for large-scale parallel computers supporting shared memory in hardware. Because a shared memory programming model is generally regarded as a more intuitive way to create parallel programs, this trend has a potential to increase the use of parallel computers.

At the same time, SMP clusters have appeared as a cost-effective alternative to large multicomputers. Because such systems do not support a shared memory image, it has to be implemented through a software layer usually referred to as a software distributed shared memory (DSM) system. Such systems have been around for some time now, and they can deliver reasonable performance for some classes of applications.

The goal of our research is to investigate performance-enhancing techniques of software DSM systems for SMP clusters interconnected with a high-performance interconnection network.

During 1998, we performed two studies in this area [Karlsson and Brorsson, 1998, Rodman and Brorsson, 1998]. In the first, we investigated a technique to predict communication so that data is pushed to its destination before it is requested. This reduces effectively the number of messages and has been shown to improve performance significantly for some applications. In the second study, we have integrated message-passing primitives in the shared memory programming model to study the effects on programming effort. We have found that for some applications, very small changes in the application source code can lead to significant performance improvement—approaching a pure message-passing

The goal of our research is to investigate performance-enhancing techniques of software DSM systems for SMP clusters interconnected with a high-performance interconnection network.

program, which is much more difficult to develop in the first place.

For both of the studies above we have used the IBM SP at PDC at KTH in Stockholm. This system is especially well suited for this research because it is a controlled environment, which makes it easy to do performance measurements. The system resembles a network of workstations (or SMPs with the SMP nodes) with a high-performance interconnection network. In addition to the two research studies mentioned above, we are also using the IBM SP system for a research implementation of OpenMP for networks of workstations.

8 Physics

8.1 *Ab Initio* Calculations of Phonon Dispersions in Transition Metals

Kristin Einarsdotter, Mathias Ekman, Göran Grimvall
Department of Theoretical Physics, KTH

Dynamical instabilities or anomalous softening in lattice vibrations of metals are of considerable interest. We have used a linear response method within the density functional theory (DFT) to calculate phonon dispersions for several transition metals in different structures. Not many calculations of phonon dispersion curves exist using this state-of-the-art technique. Published results, including our paper [Einarsdotter *et al.*, 1997], show that the method has a very high level of reliability.

In one project the calculated dispersion curves for bcc and fcc W and Re were used to study the thermodynamic and dynamic stability the disordered Re_xW_{1-x} system. Tungsten is dynamically stable in the bcc structure and unstable in the fcc structure. The opposite is true for rhenium. Most of the phonon instabilities in fcc W and bcc Re can be connected with a distortion of the crystal leading to a another more stable high-symmetry structure. In the alloy, the stability of the two phases as a function of the concentration x was determined. From the dispersion relations, the vibrational free energy was also calculated and included in the analysis of the thermodynamic stability of the bcc and fcc disordered phases. The vibrational contribution to the total free energy is often neglected in *ab initio* calculations because it is difficult to obtain the phonon frequencies. However, the few existing studies (including our own) show that the vibrational free energy is important when comparing the stability between competing structures.

The vibrational free energy is important when comparing the stability between competing structures.

Another study involves elements that exhibit a low-temperature close-packed phase and a high-temperature bcc phase. Measured phonon dispersions for these elements in the bcc phase are dominated by low-energy phonon modes interpreted as phase transition precursors. The stabilization mechanism for the high-temperature phase has been discussed, particularly since it was discovered that two high-symmetry phonons were dynamically unstable at low

temperatures. Until now, only high-symmetry phonons in these bcc metals have been studied by first principles. We have calculated the phonon dispersions for scandium, titanium, lanthanum, and hafnium, all of which have a close-packed ground state and transform to the bcc structure at high temperatures.

We have found that the instabilities are widely spread and extend far into the Brillouin zone. One unstable transverse branch in particular is interesting because experiments show no anomalous damping of this branch. The dispersion curves in the symmetry directions are very similar for all elements in this study except this branch, which is unstable for Ti, La, and Hf but stable for Sc.

Upon melting, silicon undergoes a semiconductor-to-metal transition. The difference in entropy between the solid phase and the liquid is unusually large, and reason for this has not yet been completely understood. By calculating the phonon dispersions for the ground state of Si and a suitable metallic solid phase, we will study the difference in vibrational entropy.

The linear response method avoids using supercells in phonon calculations, but is still time consuming and highly memory demanding. The computational programs used are of a highly parallel nature because the calculations are performed on a mesh of k-points where the result for every k-point is independent of the others. It is fair to say that the major part of our research performed during the last year would have been impossible without the use of the IBM SP Strindberg.

8.2 Electronic Structure Calculations for the Physics of Surfaces and Materials

Mats Persson
Department of Applied Physics, CTH and Göteborg University

Ongoing projects include surface reaction dynamics, atomic and molecular manipulation, molecular adsorption on stepped surfaces, interface energies, and electronic structure for bimetals.

This project primarily concerns first-principles electronic structure calculations of physical properties of surfaces and materials based on density functional theory (DFT). The overall goals are to develop a physical understanding on an atomistic scale of various materials and surface phenomena, and to predict physical properties for systems that have not yet been made. Ongoing projects include surface reaction dynamics, atomic and molecular manipulation, molecular adsorption on stepped surfaces, interface energies, and electronic structure for bimetals. Our progress and

results in these areas are detailed below, and we end with a short description of our computational method. People in our group who have been active in these projects during the year include graduate students Lennart Bengtsson, Jan Hartford, and Martin Hassel; and TMR postdoc Nicolas Lorente.

The recent developments of computational schemes, based on DFT, of reliable potential energy surfaces that can be used in dynamics calculations and of dynamical measurements (that go beyond structural and kinetic) enable us to begin to gain clear insight into mechanisms behind surface reactions. Our project of calculating various sections of the PES for Eley-Rideal and hot-atom reaction pathways of hydrogen atoms on a Cu(111) surface have now been completed [Strömquist *et al.*, 1998, Shalashilin *et al.*, 1998, Persson *et al.*, 1999]. Based on these results, we have constructed a model PES; we have succesfully used this model in reaction dynamics calculations in order to quantitatively understand observations from state-resolved molecular beam scattering experiments in terms of elementary reaction mechanisms.

Adsorption on stepped surfaces is a model for the study of the role of defects on surfaces in heterogenous catalysis. For instance, surface atoms at kink sites on stepped surfaces have low coordination and symmetry, and they can exhibit unusual properties. From an analysis of measured electron energy loss spectra by Andersson and coworkers, at Chalmers University of Technology/Göteborg University (CTH/Göteborg University) and from results of total energy calculations, we have been able to identify a novel 2D-like rotor state of H_2 adsorbed on a kink atom of a stepped Cu(510) surface [Svensson *et al.*, 1999, Bengtsson *et al.*, 2000]. These calculations have taken into consideration more than 1,000 configurations of the H_2 molecule on a 24-atom slab and could not have been performed without access to the IBM SP at PDC.

The scanning tunneling microscope (STM) has emerged as a unique tool for imaging and controlled modification of materials on the atomic scale. Recently, Ho and coworkers were able to demonstrate the principle of vibrational spectroscopy by the tip of the STM for acetylene molecules adsorbed on Cu [Stipe *et al.*, 1998].

We have developed a first-principles calculation method of single-molecule vibrational spectroscopy and microscopy by the scanning tunneling microscope. The method is based on density functional

theory and a many-body generalization of the Tersoff-Hamann theory. We apply our method to acetylene on copper. The calculated equilibrium geometry, vibrational modes, elastic and vibrationally inelastic intensities, and STM images are in good agreement with experimental data. We explain why only the carbon-hydrogen stretch modes are observed in terms of inelastic and elastic contributions to the tunneling conductance. The inelastic tunneling is found to be efficient and highly localized in space without any resonant interaction and is also found to be governed by a vibration-induced change in tunneling amplitude [Lorente and Persson, 1999].

Materials properties ultimately depend on the constituent atoms in a hierarchial manner, from the atomic up to the macroscopic scale. On the intermediate scale, interfaces are the key features for these properties. Interface energies are prohibitively difficult to establish by experimental means, and theory plays an important role. A common interface in alloyed steels is between Fe and VN. We have calculated interface energies between Fe and VN layers with N vacancies in a supercell geometry [Hartford, 2000]. The results point out features of the electron structure that make the formation of very small VN precipitates in Fe favorable.

Our main computational tool is the code DACAPO, which implements the plane-wave and pseudopotential method for the solution of the Kohn-Sham equations of DFT in a supercell geometry. This code was originally developed by Hammer and coworkers in Lyngby, Denmark. It has been parallelized over k-points, and optimized on the IBM SP by Bengtsson in our group. In one of our applications–which involves the calculation of the total energies of a large number of configurations–the code ran at 400 Mflop/s/node.

8.3 Forced Response Analysis and High Cycle Fatigue Prediction of Bladed-Disk Assemblies

François Moyroud, Sébastian Regard, Torsten H. Fransson
Department of Heat and Power Technology, KTH
Institut National des Sciences Appliquées
Georges Jacquet-Richardet
Laboratoire de Mécanique des Structures (LMSt),
Institut National des Sciences Appliquées
Gabor Csaba, Hans Mårtensson
Volvo Aero Corporation

Introduction

The high-performance bladed disks used in today's turbomachines must meet strict standards in terms of aeroelastic stability and resonant response level. Phenomena that can significantly affect both these areas are blade flutter, blade forced response, and bladed-disk mistuning [Srinivasan, 1997, Moyroud, 1997, Moyroud *et al.*, 1998].

Blade flutter is an aeroelastic instability caused by the fluid-structure interaction between the unsteady aerodynamic motion-dependent flow field and the vibratory motion of the bladed disk. Blade forced response is concerned with the response of a bladed disk to external forcing functions, mainly emanating from the unsteady aerodynamic interaction between fixed blade rows (stators) and moving blade rows (rotors). Excessive resonance response leads to high cycle fatigue problems when the structural material endurance is exceeded. Bladed-disk mistuning results from blade-to-blade variations in the geometric and structural properties of bladed disks that occur during the manufacturing process, and/or as a consequence of in-service wear. Mistuning can significantly affect the aeroelastic and resonant response of bladed disks.

Mistuning can significantly affect the aeroelastic and resonant response of bladed disks.

Approach

Prediction tools are developed and validated within this research project toward the following.

1. an accurate modeling of the 3D structural dynamic behavior of tuned and mistuned bladed disks

2. an accurate modeling of the unsteady turbomachinery flowfield by taking into account vibrating blades and relatively moving

blade rows

3. an accurate modeling of structural mistuning with specifically tailored reduction techniques

4. an accurate modeling of the interaction between the flow domain and the structural domain

A fluid-structure master program, STRUFLO, has been designed during this work to provide a number of interfaces between a set of existing flow and structural solvers, as well as fluid-structure aeroelastic analysis schemes [Jacquet-Richardet *et al.*, 1996, Jacquet-Richardet *et al.*, 1997, Ben, 1998, Moyroud, 1998c]. To predict the structural dynamics of tuned and mistuned bladed disks, the CORIODYN code is the main prediction tool currently used. (CORIODYN is a 3D finite-element structural solver developed at LMSt/INSAL, Villeurbanne, France for cyclic symmetric modal analyses of bladed disks.) To predict steady and unsteady flows around blade rows, the VOLSOL code is the main prediction tool currently used. (VOLSOL is a 3D multi-block finite volume Euler/Navier-Stokes solver developed at Volvo Aero Corporation, Trollhättan, Sweden.)

Need for HPC Resources

Within this project, the use of HPC facilities available at PDC is justified for several reasons.

In order to predict bladed disk mistuning, modal analyses of full assemblies is the only reliable approach for accurate predictions. This leads to computations on large finite-element models with typically 500,000–1,000,000 degrees of freedom. Efficient reduction techniques have been developed to reduce the computational cost of full assembly finite-element analyses. These reduced-order models have been implemented in CORIODYN and are documented [Moyroud and Jacquet-Richardet, 1997, Moyroud and Jacquet-Richardet, 1999a, Moyroud and Jacquet-Richardet, 1999b].

Considerable reductions are obtained in the number of equations to be solved, but a large amount of memory is still necessary to perform the reductions. A typical full assembly modal analysis of an industrial bladed disk requires 1–2 Gbyte of memory. To further reduce the computational cost, vectorization is used to evaluate the reduced matrices from the parent finite-element matrices (mass, stiffness). The calculation of the reduced matrices for

Figure 8.1. Finite-element structural grid for the DCAHM1 fan rotor, 102,210 nodes.

2

R
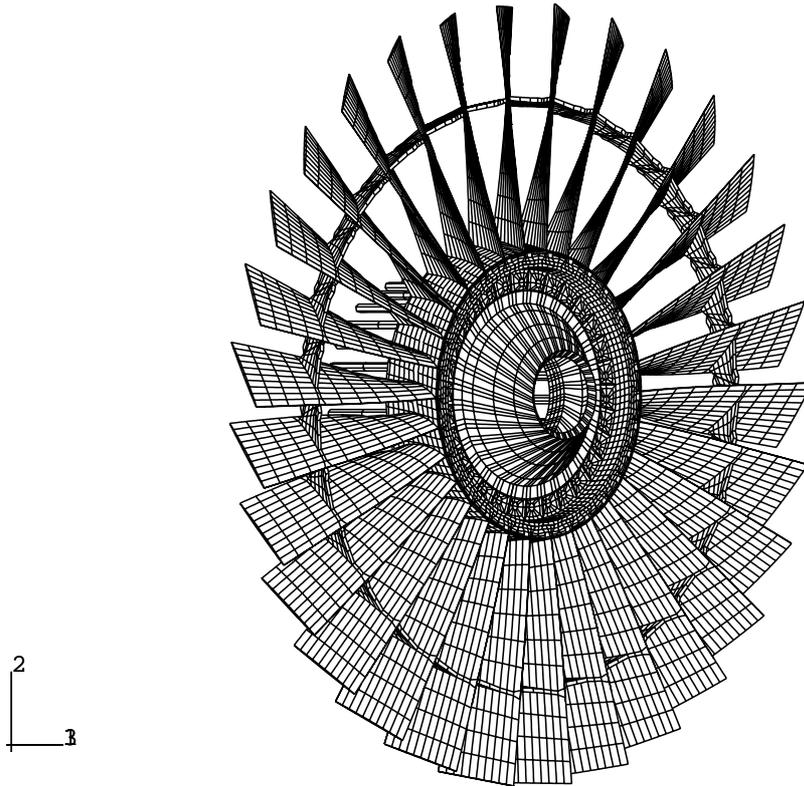
the industrial shrouded bladed disk shown in figure 8.1 on Kallsup (CRAY J90) takes about 800 CPU minutes without vectorization and 60 CPU minutes with vectorization. After the reduction is performed, the extraction of, for example, the first 250 modes takes a few CPU minutes. A number of results obtained with CORIODYN on Kallsup on simple geometries and an industrial bladed disk are documented [Moyroud and Jacquet-Richardet, 1999b].

Cyclic symmetric unsteady inviscid aerodynamic analyses of single-blade passages are feasible with single-processor resources, and considerable speed-ups are achieved with parallel processing. Parallel processing is currently the only way to perform full assembly unsteady inviscid aerodynamic analyses, due to the very large mesh sizes. The computational domain is decomposed according to the blade passages. The advantage of the blade passage decomposition is that the number of processors increases linearly with the number of blade passages while the required CPU time

remains constant. Full assembly unsteady aerodynamic analyses are feasible on the IBM SP, Strindberg [Moyroud, 1998b, Moyroud, 1998a]. A number of unsteady aerodynamic analyses of the NASA ROTOR 67 fan and the STCF4 transonic turbine have been run on Strindberg with the VOLSOL code. Figure 5.22 is a full assembly inviscid multi-block mesh for the NASA ROTOR 67 with 22 blade passages, 44 blocks, and more than 2,000,000 nodes. The VOLSOL job was run with 44 slave T-nodes and 1 master G-node requiring 50–70 wall CPU hours. 1.2 Gbyte are used on the master node. These preliminary tests clearly show that accurate flutter analyses of mistuned single-blade rows are feasible with a nonlinear unsteady flow solver such as VOLSOL. This is a key issue for the project.

8.4 Influence of $pp\pi$ Ions on Pion Absorption in H_2

Svante Jonsell, Piotr Froelich
Department of Quantum Chemistry, Uppsala University
Janne Wallenius
Department of Nuclear and Reactor Physics, KTH

The present investigation focuses on the role of three-body $pp\pi$ resonances formed when pionic hydrogen atoms $p\pi$ collide with H_2 molecules.

The fate of the pions entering hydrogen is of importance for precision spectroscopy experiments, and/or experiments studying the strong-force aspects of the nuclear pion absorption by the hydrogen nuclei. Our research addresses questions of interest for the new generation of experiments determining the strong-force shift and width of the $1s$ energy level of the $p\pi$ atom, and it concentrates on problems relevant to an experiment aiming at the determination of the mass difference between negative and neutral pions, $m_{\pi^-} - m_{\pi^0}$ [Crawford *et al.*, 1991].

The present investigation focuses on the role of three-body $pp\pi$ resonances formed when pionic hydrogen atoms $p\pi$ collide with H_2 molecules. We have calculated the energies and Coulombic life times of such resonances using a variational method in Jacobi co-

ordinates [Kamimura, 1988]. In order to calculate the Coulombic life times, we employed the method of complex scaling [Reinhardt, 1982]. The complex dilation operator is defined as

$$U(\theta)f(\mathbf{r}) = e^{3\theta/2}f(e^{\theta}\mathbf{r}). \tag{8.1}$$

The complex dilated Hamiltonian is then

$$H(\theta) = U(\theta)HU^{-1}(\theta) = e^{-2\theta}T + e^{-\theta}V. \tag{8.2}$$

The stationary solutions of the complex dilated eigenvalue problem correspond to the complex energies of the resonances. To assure θ independence of resonances (guaranteed by the exact theory), the eigenvalues of the concomitant matrix eigenvalue problem are stabilized with respect to the condition $\partial E/\partial\theta = 0$.

The dilation operation leaves the overlap matrix $\mathbf{S}$ unchanged. One can therefore reduce the generalized eigenvalue problem $\mathbf{H}(\theta)c^{\theta} = E^{\theta}\mathbf{S}c^{\theta}$ to a standard eigenvalue problem by a single Cholesky decomposition [Golub and Van Loan., 1989] of $\mathbf{S} = \mathbf{L}\mathbf{L}^{\mathrm{T}}$, where $\mathbf{L}$ is lower triangular, for all θ. The resulting eigenvalue problem

$$\mathbf{L}^{-1}\mathbf{H}(\theta)\left(\mathbf{L}^{\mathrm{T}}\right)^{-1}c^{\theta} = E^{\theta}c^{\theta} \tag{8.3}$$

is complex symmetric. This symmetry can be used by reducing $\mathbf{L}^{-1}\mathbf{H}(\theta)(\mathbf{L}^{\mathrm{T}})^{-1}$ to a tridiagonal matrix using the Lanczos method [Golub and Van Loan., 1989, Schneider and Freed, 1989]. We have also used reduction to a Hessenberg matrix by the Arnoldi method [Golub and Van Loan., 1989]. We found that the latter method, although more time consuming, was numerically more stable. Examples of paths in the complex plane for a $pp\pi$ resonance are given in figure 8.2.

All computations were performed on the Fujitsu VX/3 computer, Selma. A more complete presentation of the project is given in [Jonsell *et al.*, 1999].

8.5 Large-Scale FD-TD: A Billion Cells

Ulf Andersson, Gunnar Ledfelt
Parallel and Scientific Computing Institute, KTH

Introduction

We describe here a one-billion-cell FD-TD (Finite-Difference–Time-Domain) calculation on a Saab 2000 aircraft. We used a parallel

Figure 8.2. Scaling paths in the complex plane for a $pp\pi$ resonance. The numbers in the graph indicate the number of Gaussians used to calculate the different scaling paths. The markers show steps of 0.01 rad in the complex scaling parameter θ. The resonance is located at $E = -236.173 - 0.0013i$ eV.
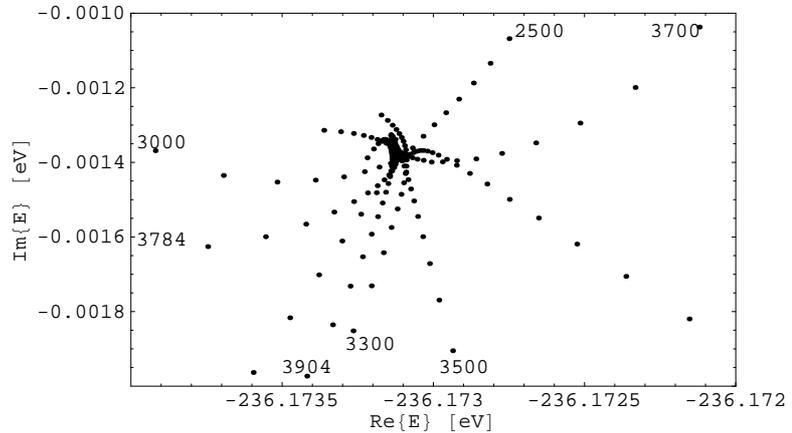
Maxwell solver that we have developed within the "Large Scale FD-TD" project of PSCI. (See http://www.nada.kth.se/~ulfa/CEM.html.) This calculation was presented at SuperComputing98 and at the Applied Computational Electromagnetic Society 99 Conference.

Physics

A lightning strike to an aircraft results in surface currents on the exterior of the fuselage that can be as high as 200,000 Amperes. Through the windows, the currents also leak into the aircraft, where they can induce high currents on wires. These induced currents might jeopardize or destroy electronic equipment, if the equipment is not designed to withstand these currents. If one could find the "hot spots" where the surface currents are high, one could try to avoid putting cables there. The lightning threat is growing more serious. Because aircraft are equipped with more and more electronic devices, and because every aircraft is struck by lightning on average once a year, there is a need to predict the electromagnetic environment of aircraft.

*Because aircraft are equipped
with more and more
electronic devices, and
because every aircraft is
struck by lightning on average
once a year, there is a need
to predict the electromagnetic
environment of aircraft.*

Method Used

The method used to solve the Maxwell equations is the Finite-Difference–Time Domain (FD-TD) method, which is a second-order leap-frog scheme using staggered grids. The object of interest

(in this case, the aircraft) is embedded in a Cartesian grid, and the object is modeled by approximating the geometry in a LEGO fashion. This staircasing of the object is one of the main drawbacks of the FD-TD method.

Geometry

The object in this calculation is the Saab 2000 aircraft, which is a commercial airliner for 50–60 passengers. A Cartesian description of the aircraft was created from a CAD description using CADFIX. A volume of approximately $30 \times 30 \times 15\,\mathrm{m}^3$ was divided into small cubes with sides of 2.5 cm. This discretization was performed by Ericsson Saab Avionics (ESB). The total number of surface elements is approximately one million. If a surface quad is to be treated as a perfect electric conductor, the four surrounding E-field components are set to zero in each time step. Hence, it is very easy to include complicated structures like an aircraft, when the Cartesian description is given.

Parameter Settings

The total number of cells is $1260 \times 1260 \times 635 = 1,008,126,000$, and the number of time steps is 2,500. The time step is $83.3\,\mathrm{ps}$ and is chosen such that it takes two time steps to propagate information perpendicular through one cell. Mur's first-order absorbing boundary condition is used to truncate the open problem. In this simulation, the excitation is performed by driving an electrical component in front of the nose by a Gaussian-shaped time-dependent function.

Parallel Computing

We need only six floating-point values per cell in this simulation (due to the homogeneous air surrounding the aircraft). Using 32-bit precision (four bytes) means that we need approximately 24 Gbyte of memory for a one-billion-cell simulation. Clearly, only a parallel computer can supply this. We used 125 nodes with 160 MHz RS/6000 processors of the IBM SP at PDC, KTH. The parallel implementation of the code uses the Message Passing Interface standard, and the computational domain was split into $5 \times 5 \times 5$ blocks, where each block was put on one processor. More details on the parallel implementation are available in [Andersson,

1998a] and [Andersson, 1998b].

Performance

The performance of the code is almost 25 Gflop/s for the total time-stepping procedure. This corresponds to 1.6 seconds per time step, for a total time of 66 minutes. Initialization takes roughly 9 minutes, and writing output during the time-stepping process takes approximately 4.5 seconds per output (the output in this case is surface currents and magnitude of the magnetic field on two slice planes). See figure 5 on page 73 and figure 5 on page 73.

8.6 Monte Carlo Simulations of Vortices in High-Temperature Superconductors

Jack Lidmar, Mats Wallin
Department of Theoretical Physics, KTH

When a type-II superconductor is placed in a magnetic field, it displays many unusual properties. The magnetic field will not penetrate the sample homogeneously as one might expect, but will instead be concentrated to small flux tubes called vortices. These line-like objects interact strongly with each other, and also with various types of imperfections in the material. Thes interactions offer the opportunity to investigate a variety of physical phenomena of great theoretical as well as experimental interest. The phase transition between the superconducting and the normal state is strongly affected by the motion of vortices. When a current is applied to a superconductor, a vortex will experience a Lorenz force. If the vortex is free to move in response to this force, a voltage will be induced according to Maxwell's equations, leading to dissipation and loss of superconductivity. By doing simulations of vortex systems, we can calculate several quantities of direct experimental interest, for example, the resistivity and the nonlinear current-voltage characteristics.

In clean superconductors, the vortices will form a triangular Abrikosov vortex lattice. As the temperature is increased this can melt into a non-superconducting vortex line liquid. In Monte Carlo simulations (MC) of a model of interacting vortex lines, this melting transition is found to be a single first-order transition from the crystalline state to an entangled vortex liquid [Lidmar
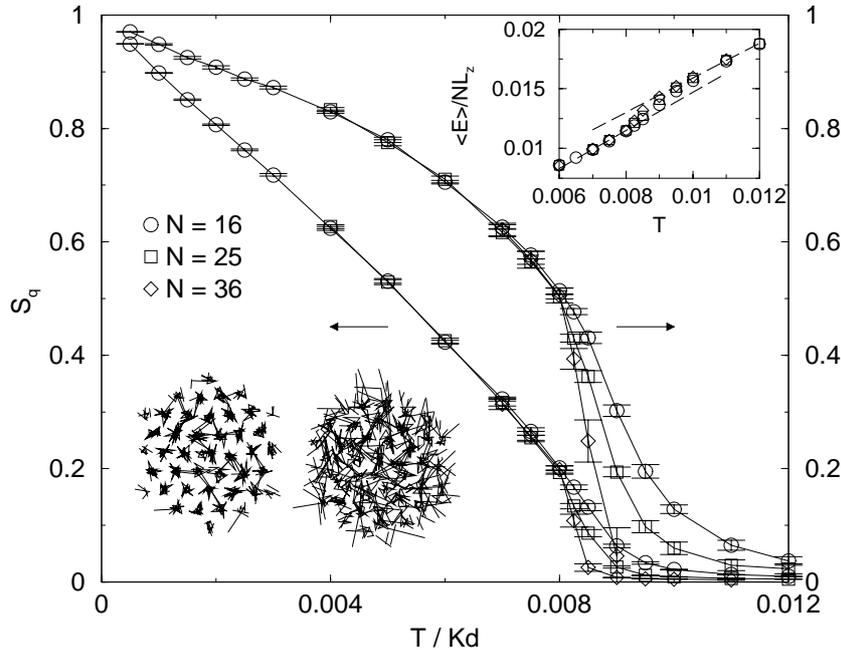
Figure 8.3. Structure function S_q (measuring lattice order) and helicity modulus Υ_z (measuring superconducting phase coherence along the magnetic field) as a function of temperature for different numbers of vortices N. The sharp drop in both quantities at $T_c \approx 0.008\,Kd$ indicates that the Abrikosov vortex lattice melts in a single first-order transition. The inset shows the jump in energy per vortex and layer at the transition. Also shown are two typical snapshots from the simulation.

and Wallin, 1999], with an entropy jump comparable to recent experiments (see figure 8.3).

The presence of material imperfections in superconductors, including point defects, columnar defects, twin boundaries, has important consequences and may lead to several new possible phases for the vortices. The transition temperature and the critical current of a superconductor can be significantly increased by pinning the vortices to these defects, thereby reducing their mobility. A way to enhance the pinning is by artificially introducing columnar defects into the material by heavy ion irradiation. Apart from the practical importance in applications this is also a theoretically very interesting problem, which has received considerable attention recently. At low temperatures, the vortices are localized at the columnar defects; and the system is in a glassy state (a Bose glass) characterized by an infinite tilt modulus, a highly nonlinear current-voltage characteristic, and a vanishing linear resistivity. As the temperature is raised, the vortices delocalize and the system turns into an entangled flux liquid.

We use Monte Carlo simulations of a model with columnar defects to study both the critical dynamics as well as the effect of

Figure 8.4. Monte Carlo results for the linear resistivity *vs.* system size L at the Bose glass transition in the directions parallel and perpendicular to the columnar defects. The power-law behavior at the transition allows the dynamical critical exponent to be estimated to $z \approx 4.6$.
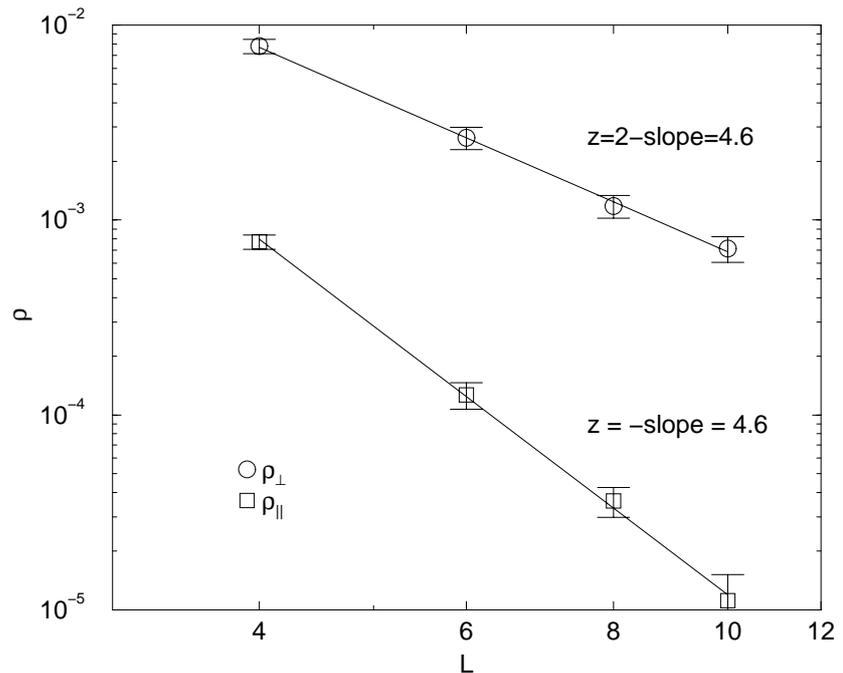
tilting the applied magnetic field with respect to the columns at the Bose glass transition. From finite size scaling of the linear resistivity (see figure 8.4) and from the non-linear I-V characteristics, we find the value $z \approx 4.6$ for the dynamic critical exponent.

The problems we study are ideally suited for the parallel computing resources at PDC. Our simulations, carried out on the IBM SP at PDC, are very computer intensive—especially the problems with disorder, because they involve extensive averaging both over vortex configurations and over different realizations of the quenched disorder. Our codes implement this averaging process by sampling disorder realizations independently on each node, leading to a very efficient parallelization. The success of these difficult computations depends crucially on the use of the supercomputer facilities at PDC.

8.7 Nuclear Spin Relaxation in Paramagnetic Complexes of $S = 1$: Comparison of Different Models

Tomas Nilsson, Jozef Kowalewski
Division of Physical Chemistry, Arrhenius Laboratory
Stockholm University

Nuclear magnetic relaxation dispersion (NMRD) profiles present the field-dependence of nuclear spin relaxation rates. NMRD is commonly used to investigate microscopic structural and dynamic properties in paramagnetic transition-metal complexes. We investigate the paramagnetic relaxation enhancement (PRE) of rapidly exchanging ligand protons (*e.g.*, in water molecules) in paramagnetic complexes of $S = 1$. Complexes of low symmetry cannot be handled by simple models, such as the commonly used Solomon-Bloembergen-Morgan (SBM) theories, because at low magnetic field a static zero-field splitting (ZFS) interaction is present.

A general theory that can handle these kinds of systems was developed by Kowalewski and coworkers in the early 1980s, and it is called the slow-motion theory [Nilsson *et al.*, 1998]. In the slow-motion theory we describe the electron spin relaxation by a transient ZFS, which is modulated by distortion of the hydration shell originating from solvent collisions. The whole theory is based on the Liouville superoperator formalism. All relevant interactions—such as the hyperfine interaction between the nuclear and electron spin, the static and transient ZFS interactions, the nuclear and electron spin Zeeman interactions, and in addition, classical degrees of freedom that describe the reorientation and distortion of the complex—are included in the Liouville superoperator.

The calculation of nuclear spin relaxation rates involves setting up a huge matrix (about $100,000 \times 100,000$ for $S = 1$) and then inverting it. The matrix is truncated at a certain size after convergence has been reached. This is checked by increasing the matrix until the difference between two consecutive values of the nuclear spin relaxation rate is as small as desired. The matrix is very large but sparse, and we only keep non-zero matrix elements. Furthermore, it is only a 3×3 fraction of the inverted matrix that we need to project out. The inversion of the matrix is performed by using the Lanczos algorithm.

The calculations are successfully performed on the Strindberg IBM SP parallel computer. One reason for using this facility is our need for a lot of computer memory (0.5–2 Gbyte of internal

memory), especially when we do the convergence tests. Second, the calculations are very time consuming. The present version of the parallelized Fortran code uses MPI and is optimized in both setting up the matrix and inverting it. Thus, in setting up the matrix, it is divided up into a large number of subsections so that each node has the same number of matrix elements to search for those which are non-zero. By setting up the matrix in this way we obtain about the same number of non-zero matrix elements for each node. This is required if we want the inversion routine to work evenly distributed between the nodes.

However, if we want to fit a model to experimental data, we would like to have a simpler model where we can obtain an NMRD profile very fast. There are other models that are fast and can handle low-symmetry complexes, such as the approach developed in Florence by Bertini and coworkers. In cooperation with the group in Florence, we have used the results from the slow-motion calculations, which can be considered as essentially exact within the number of terms included in the Liouville superoperator. We then compared these with the NMRD profiles of the Florence model [Bertini *et al.*, 1999]. The Florence model was modified to more accurately describe the electron spin relaxation.

In figure 8.5 we show the relative difference (in percent) in nuclear spin relaxation rate between the slow-motion model and the original (dotted lines) and modified (solid lines) version of the Florence model as a function of the magnitude of the transient ZFS (Δ_t). The curves have been calculated for a slowly reorienting complex with axial symmetry. The magnitude of the static ZFS, Δ_S, is $1\,\mathrm{cm}^{-1}$. Meaningful comparisons of NMRD profiles are confined to the region between the vertical dotted lines, where in a large part of the region the relative difference is less than $1\,\%$.

In figure 8.6 we present a set of NMRD profiles showing the good agreement between the slow-motion and the Florence models. The NMRD profiles were calculated for $\Delta_S = 1\,\mathrm{cm}^{-1}$, $\Delta_t = 0.1\,\mathrm{cm}^{-1}$, and for different angles θ, which defines the position of the nuclear spin relative the principal axis of the static ZFS tensor. The NMRD profile of the SBM theory is shown for comparison purposes, and it is evident that it agrees very poorly with the other models.

From the comparisons, we can conclude that the Florence model works very well in the limit of slow reorientation and moderately fast electron spin relaxation, and we can also conclude that the
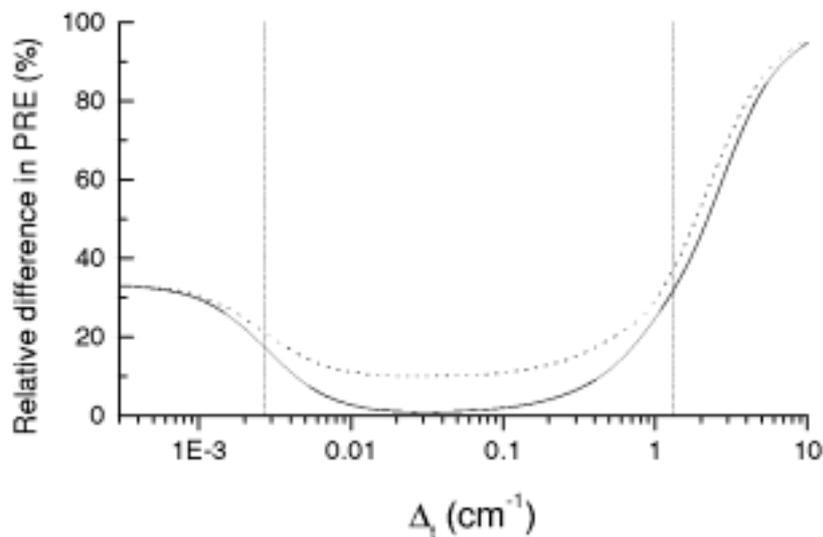
Figure 8.5. Relative difference in the nuclear spin relaxation rate as a function of the magnitude of the transient ZFS at the low-field limit (expressed as percentage) predicted by the slow-motion model and the modified (solid lines) and the original (dotted lines) version of the Florence model. The magnitude of the static ZFS, Δ_S, is $1\,\mathrm{cm}^{-1}$, and the reorientation correlation time, τ_R, is $1\,\mu$.
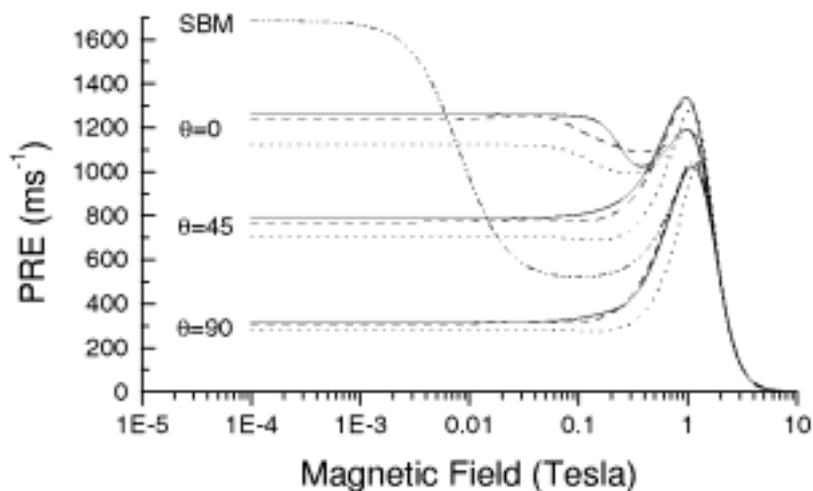
Figure 8.6. NMRD profiles for the $S = 1$ case, with $\Delta_t = 0.1\,\mathrm{cm}^{-1}$, $\Delta_S = 1\,\mathrm{cm}^{-1}$ (axial symmetry of static ZFS), for different θ angles. The same parameters are used in the slow-motion approach (solid lines) and in the Florence approach with the original (dotted lines) and the modified (dashed lines) version of the program. The curve corresponding to the SBM theory is also shown (dotted-dashed lines) for comparison purposes.

modification of the Florence model has improved the agreement with the slow-motion model.

8.8 Phase Diagram of the Quantum Anisotropic XY Spin Chain in a Random Field

Ausrius Juozapavičius, Sergio Caprara, Anders Rosengren
Department of Theoretical Physics, KTH

Non-commutativity of quantum spin operators leads to much more complicated effects induced by randomness than in classical mechanics, especially when the random noise is coupled not directly to the interactions of those spins, but rather is introduced as an external force. The properties of such random quantum systems are determined mostly by rare regions that have the opposite phase compared to the phase of the whole system.

These rare regions create the so-called Griffith's phases, where the zero-field susceptibility diverges in a wide region around the critical quantum order-disorder transition point, whereas it diverges only in one point for classical non-random systems. These same regions are responsible for the big differences between typical and average properties (*e.g.*, average correlation functions decay much more slowly than the typical ones) of the system. Despite the evident difficulties in analyzing such systems, D. S. Fisher obtained a lot of information for the simplest of random systems—the quantum Ising spin chain in a transverse random field using the Renormalization Group technique. However, there are still many unsolved problems even for this simple system, but they can be clarified using numerical methods.

We have studied a generalized XY spin chain—the so-called anisotropic XY spin-1/2 chain in a transverse random magnetic field, which becomes either the Ising spin chain (the factor of anisotropy γ is defined to be zero then) or the simple XY spin chain (γ=1). The model is defined by the Hamiltonian

$$\mathcal{H} = -J \sum_{i}^{N-1} S_i^x S_{i+1}^x - \gamma J \sum_{i}^{N-1} S_i^y S_{i+1}^y - \sum_{i}^{N} h_i S_i^z - h_x \sum_{i}^{N} S_i^x,$$

where N is the number of sites in the chain, $S^\alpha = \sigma^\alpha/2$, σ^α are Pauli matrices, J is the coupling constant, and h_x is a (small) uniform magnetic field that lifts the degeneracy of the system in our calculations. The on-site values $\{h_i\}$ of the random field are

uniformly distributed in the interval $-h_0 < h_i < h_0$. An increased amplitude h_0 of the random field decreases the magnetization $M = \langle S^x \rangle / N$, where S^x is the total x-spin operator of the system, and $\langle \cdot \rangle$ stands for the quantum expectation value in the ground state. Sufficiently big randomness destroys the order in the system, and one of the aims of our research was to calculate the phase diagram of this spin chain—to find the points $h_c = h_0(\gamma)$ where the spontaneous magnetization $M_0 \equiv M(h_x \to 0)$ goes to zero.

One of the aims of our research was to calculate the phase diagram of this spin chain.

The method we used in our calculations—the Density-Matrix Renormalization Group—was developed by S. R. White. Both the description of this method and some previously known results can be found either in the *PDC Progress Report 1997* or in [Juozapavičius *et al.*, 1999]. We are going to present here only some of the most important results.

The phase diagram is plotted in figure 8.7. The formulas in the figure caption let us interpret the behavior of the system using the language of spin wave theory. We see that quantum fluctuations lead to a renormalized effective Hamiltonian. The field S_i^x is renormalized as $\tilde{S}_i^x = (1 - \gamma^2)^\vartheta S_i^x$ at $h_0 = 0$. This in turn leads to an effective Ising-like model with renormalized coupling constant $J_\gamma = J(1 - \gamma^2)^{2\vartheta}$, and the increase in the strength of random field due to quantum fluctuations is entirely due to a reduction of the coupling constant, and the scaling law $\varrho = 2\vartheta$ holds.

Figure 8.8 shows the behavior of the spontaneous magnetization at criticality. The exponent β is equal to 0.38 (within the error bars) for any γ, which is compatible with the analytical results of D. S. Fisher. This is strong numerical evidence of universality.

As an independent check of the phase diagram, the energy gap between the ground state and the first excited state was calculated (figure 8.9). The gap becomes zero at criticality. Because the curves are exponentially flat near criticality, the critical points are much more accurately determined from the magnetization curves than from the gap data. However, when h_c is determined from magnetization data, the correspondingly rescaled gap data collapse near criticality on one curve, as shown in the inset of figure 8.9.

All these and some additional results (*e.g.*, the asymptotic behavior of two-point spin-spin correlation functions) provide clear numerical evidence that models with different values of the fac-

Figure 8.7. The triangles represent the critical points h_c obtained by DMRG calculations for different values of the factor of anisotropy γ. The solid line is the best fit of the form $h_c = h_c(0)(1 - \gamma^2)^\varrho$ with $\varrho = 0.52 \pm 0.01$. The system is in a ferromagnetic state below this line. The circles represent the dependence of the spontaneous magnetization on γ at $h_0 = 0$. Data are fitted by $M_0 = 0.5(1 - \gamma^2)^\vartheta$ with $\vartheta = 0.255^{+0.010}_{-0.005}$. The error bars that are smaller than the symbol size are not shown. The result of spin wave theory is also drawn (dashed line); it is quantitatively incorrect, but it is useful in qualitative arguments.
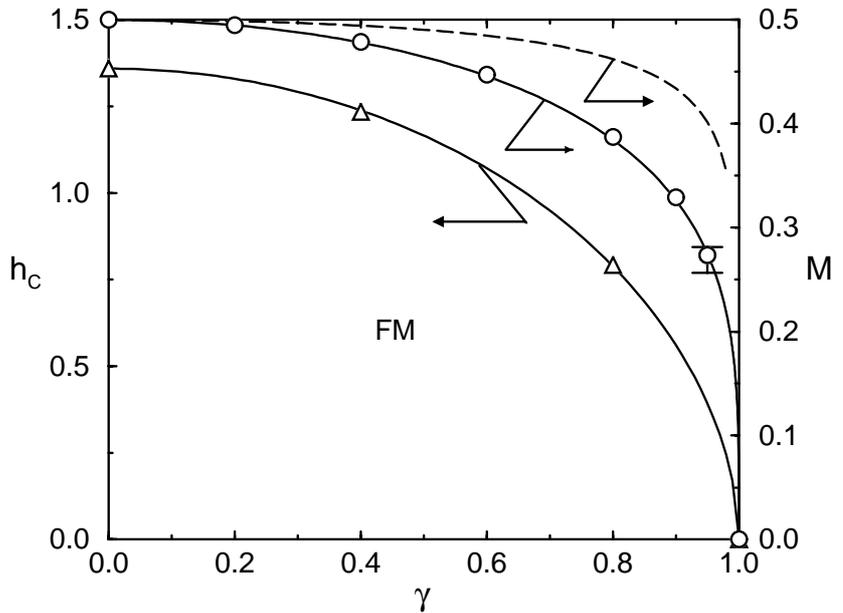
Figure 8.8. The dependence of the spontaneous magnetization on the strength of the random magnetic field h_0. The data points were fitted by the formula $M_0 = D \cdot (h_c - h_0)^\beta$.
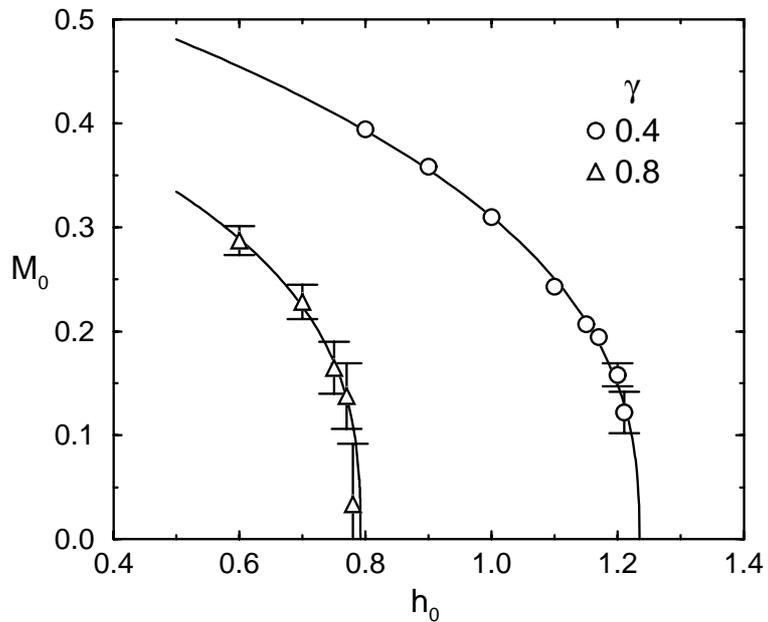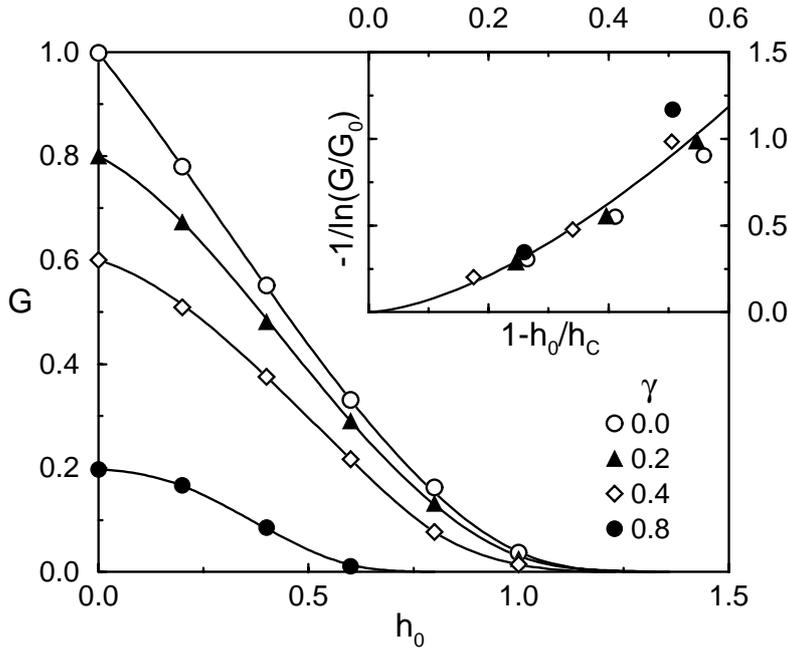
Figure 8.9. The dependence of the energy gap G on the strength of the random field h_0. System size is above 200 sites, $h_x = 0$. The average is performed over 500 realizations of the random field. The inset shows rescaled data, and the solid curve is $-1/\ln(G/G_0) = K(1 - h_0/h_c)^\lambda$ with $K = 2.6 \pm 0.4$ and $\lambda = 1.6 \pm 0.2$. G_0 denotes the gap in the absence of randomness.

tor of anisotropy $0 \leq \gamma < 1$ all belong to the same universality class as the spin-1/2 quantum Ising chain in a transverse random magnetic field.

Most of the calculations were performed on the IBM SP computer Strindberg. More than $10,000$ hours of computing time were used in total. The research would have been impossible without this computing power: even though one density-matrix renormalization-group iteration takes less than 10 seconds on one processor and it is possible to grow a spin chain of the desirable size (150 iterations) on almost any computer, it was necessary to make a huge number of such calculations for different realizations of the random field to obtain good statistics. The problem was purely statistical, and each of the field configurations being independent, so the parallelization of the problem was trivial. We ran the same program on all the processors we had, except that we gave a different seed for the random number generator. The algorithm was not very complicated, so the program was written in Fortran 77, which has the best performance for our problem. The

This research would have been impossible without the computing power available at PDC.

NAG library routines for matrix diagonalization were used[1].

8.9 PMCD: The Parallel Monte Carlo Driver in GESAMAC

António Pereira, Bruno Mendes
Fysikcentrum, Department of Physics, Stockholm University

The PMCD code is a parallel Monte Carlo Driver developed using the Strindberg parallel supercomputer at PDC [Mendes and Pereira, 1999]. This package was developed in the context of the European-funded project called GESAMAC [Eguilior and Prado, 1995].

GESAMAC's goal was to develop new tools for safety assessment of nuclear waste repositories.

GESAMAC's goal was to develop new conceptual and computational tools for safety assessment of final repositories for nuclear waste. Specifically, GESAMAC aims at tackling areas of uncertainty, and to develop some conceptual, methodological, and computational tools of potential use in actual safety analyses for radioactive waste disposal systems. Four partners with expertise in four different critical areas for safety assessment of nuclear waste repositories joined forces to achieve the objectives of the project:

- Geosphere Transport Modeling (CIEMAT-DIAE, Spain)

- Sensitivity Analysis (JRC-ISIS, EC)

- Model Uncertainty (University of Bath, UK)

- Parallel MC Driver (Dept. of Physics, University of Stockholm, Sweden)

GESAMAC offers a conceptual framework for accounting for all sources of uncertainty in the simulation of complex systems, like underground disposal systems.

Studies that assess the performance of underground radioactive waste disposal systems, which involve long time frames and the variability associated with natural open systems, are linked to different sources of uncertainties. GESAMAC offers a conceptual framework for accounting for all sources of uncertainty in the simulation of complex systems, like underground disposal systems. It considers the uncertainty in the following simulation components: past data, parameters, structure, scenarios, future observables, and predictions. This framework has been applied to a hypothetical nuclear disposal system with special emphasis on the geosphere

---

[1]This work was supported by NFR, the Swedish Natural Science Research Council.

subsystem and focused on scenario and parametric uncertainties. For stochastic simulation of the system, a parallel Monte Carlo driver (the PMCD code) has been developed and used to produce stochastic results of the performance of the system. Such results have been used for uncertainty and sensitivity analysis applying new quantitative methods developed through the project.

The PMCD software package uses MPI to allow parallel Monte Carlo simulations based on any serial code. The serial code can be any user-supplied code. The user has to specify the input variables of the code that will be sampled from certain probability distributions (pdfs), that is, which input variables will have their values changed from one Monte Carlo run to another. The user must also specify the total number of Monte Carlo runs to be performed. Finally, the user has to make some minor changes to the code in order to couple it to our software package.

The serial code used in GESAMAC was GTMCHEM [Eguilior and Prado, 1998]. It simulates migration of radionuclides in a porous media. The implementation of an effective load balancing in the PMCD code was very important, because the GTMCHEM code used for the simulations has different running times for different sets of input parameters. The difference in run times can be significant.

The project developed a framework where six different scenarios were simulated. Each scenario corresponds to different general conditions for the disposal site (different rock characteristics, different container performances, *etc.*). Uncertainty and sensitivity analyses were performed on the results from our probabilistic calculations. Figure 5.25 on page 74 shows some results obtained during the course of the project. For details on the project, the reader should consult [Draper *et al.*, 1998] and [Draper *et al.*, 1999] and references therein.

8.10 Scattering of Light by 2D Random Rough Surfaces

Teresita Quinteros
ACREO, Stockholm, Sweden
Brent Nebeker
School of Mechanical Engineering, Purdue University

The topography of a surface is characterized by the order of magnitude of the variations in height and length, quantified by its roughness and correlation length. The methods actually in use

We performed simulations of light scattering by 2D surfaces with roughness not negligible with respect to the wavelength of the incident light.

to calculate the light scattering by a rough surface are quite simple. They assume the correlation length is long compared with the heights, and hold just for the case in which the roughness is small in comparison with the wavelength. Think in two copies of the same surface profile. The amount of lateral shift between the two profiles is called lag length. The correlation length is the value of the lag length at which the autocovariance function drops to $\frac{1}{e}$.

For 1D surfaces, that is, those for which the topography varies only in one dimension over the surface, there are rigorous integral theories that can calculate light scattering by surfaces with shorter correlation length. These theories have not been developed yet for 2D surfaces with significant roughness. We performed simulations of light scattering by 2D surfaces with roughness not negligible with respect to the wavelength of the incident light. We used the discrete-dipole approximation (DDA) method [Draine, 1988, Draine and Goodman, 1993, Draine and Flatau, 1994] and performed calculations with the Fujitsu VX/3. Our method offers a long-awaited possibility of direct applicability in many different fields, such as paper optics, infrared systems, and perception of image quality.

The DDA was originally developed to study the scattering of light by particles in interstellar dust. The method is very suitable to study electromagnetic scattering by particles of irregular shape and by clusters of particles. We have previously applied DDA to the analysis of light scattering in the visible region, by clusters of many thousands of particles, simulating pigments in paper coatings [Quinteros and Bjuggren, 1998a, Quinteros and Bjuggren, 1998b].

A group at Arizona State University modified the DDA method to include the presence of a plane in the vicinity of the scattering feature. The new method was successfully applied to analyze the scattering by sub-micron particles on Si-buffers [Schmehl, 1994, Schmehl *et al.*, 1997]. We used this modified algorithm to demonstrate the applicability of the DDA method to the scattering of light by 2D surfaces [Quinteros *et al.*, 2000].

The DDA method divides the scattering feature into elementary volumes and associates each of them with an electric dipole, hence the name of the method. The optical properties of each elementary volume are input data to the calculations, and the permitivities of each dipole are set by global boundary conditions [Draine, 1988].
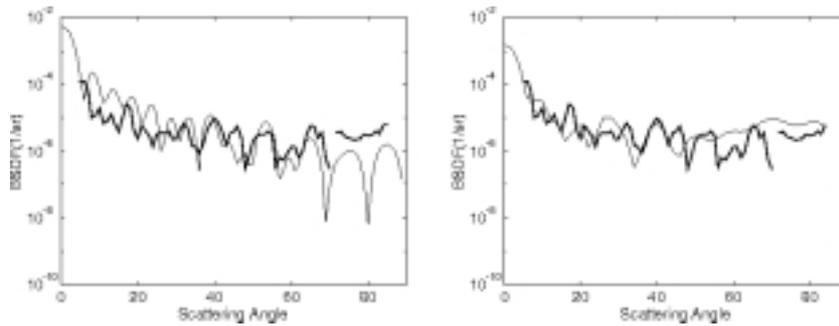
Figure 8.10. BSDF data in the scattering plane. The thick line is experimental data from the sample in figure 5.26 on page 74. The thin line is the calculated BSDF: left, from a photoresist rectangular parallelepiped $6.6 \times 6.6 \times 1.8\,\mu$m on Si; right, from a parallelepiped of the same size, with the surface roughness taken from the topographical data in figure 5.26 on page 74.

The scattered field is then calculated as the contribution to the far-field from each of the dipoles in the feature's volume. The nature of the method allows easy simulation of scattering from objects of irregular shapes, or from groups of objects of different optical properties.

Comparison with Experimental Data

We compared the result of calculations with measurements of angle-resolved scattering performed at ACREO, for the scattering of light of 633 nm wavelength by a sample consisting in a photoresist feature $10 \times 10 \times 3\,\mu$m on a Si-wafer (figure 5.26 on page 74). The surface of the photoresist was treated with e-lithography to imprint a significant rms roughness.

The thick line in figure 8.10 represents the measured in-plane bi-directional scattering distribution function (BSDF), which is a function proportional to the scattered intensity, as a function of the scattering angle. The thin line in figure 8.10 represents the results from calculations. The exact shape of the photoresist sample could not be simulated, because the sample size slightly exceeded the limits imposed by the calculation convergence demands (lattice constant and maximum allocable lattice). The calculation was made for a $6.6 \times 6.6 \times 1.8\,\mu$m photoresist rectangular parallelepiped on Si. This comparison of numerical results with measured data nevertheless illustrates well the potential of the method.

The left of figure 8.10 shows calculations from a parallelepiped with mathematically plane surfaces. The overall agreement is very good for scattering angles between $30°$ and $70°$. The calculated BSDF is underestimated for larger angles and overestimated for smaller angles. The position of peaks and valleys varies with

the size of the photoresist sample. For example, calculations performed for a $4 \times 4 \times 1.8\,\mu$m photoresist feature on Si showed better agreement with measurements for angles below 30°, and it underestimated the BSDF for larger angles. In all the cases, the BSDF for angles below 70° seems to be dominated by the overall size of the sample. The contribution from the surface roughness is a small perturbation to it, superimposed on the peak-and-valley structure of the curve for the scattering from the non-rough rectangular parallelepiped.

The right of figure 8.10 shows results from calculations for a parallelepiped of the same size as the one on the left, with a surface roughness taken from the topographical data in figure 5.26 on page 74. We find that the forward scattering is no longer overestimated as it was in the non-rough case. Instead, the contribution at larger angles (diffuse scattering) is larger.

The comparison of the data with numerical results calculated for smaller features shows an overall agreement. The calculation shows a very promising identification of the peak-and-valley structure corresponding to the overall shape of the photoresist feature without roughness, and the contribution from the surface's microroughness. Further work must be done to quantify the precision of the calculations. Nevertheless, the present results already exemplify the sensitivity of the method to simulate surface roughness effects in light scattering.

8.11 σ-phase: Analysis of Vibrational Properties

Sergei I. Simdyankin, Mikhail Dzugutov
Department of Numerical Analysis and Computer Science, KTH
Sergei N. Taraskin, Stephen R. Elliott
Department of Chemistry, University of Cambridge

The local atomic order in disordered condensed materials is well defined and governs many physical properties. Quite often, for a disordered material, it is possible to find a corresponding crystal with similar local and even intermediate-range order, which gives rise to similarities in many structural and dynamical features of these two solids. Such a crystal can be regarded as a reference crystalline structure (crystalline counterpart) for the corresponding disordered substance. In some cases, the reference structure can be uniquely defined.

The simplest examples are toy structural models with force-constant and/or mass disorder. In these toy models, the atoms occupy their equilibrium positions at the sites of a crystalline lattice (*e.g.*,, simple cubic), which can be considered a reference system. Another related example is a binary substitutional alloy for which the reference system is a periodic point lattice with one of the two atomic species placed at the lattice sites. The disorder in such models does not influence the equilibrium positions of the atoms arranged in an ideal crystalline lattice. This property makes possible the use of approximate analytical approaches to treat the vibrational properties of the models, provided that the vibrational properties of the counterpart crystal are known. In amorphous solids, or glasses, the atoms do not occupy the sites of a crystalline lattice, which results in positional disorder. For these materials, a choice for a reference structure becomes problematic. Good counterparts can usually be found among the crystalline polymorphs having the same (or similar) chemical composition as the corresponding glass.

In this study, the vibrational properties of a one-component σ-phase crystal (see figure 8.11),which is conjectured to be a good crystalline counterpart for a one-component glass with icosahedral local order (IC glass), were investigated numerically.

The σ-phase structure we used in our computations was obtained by means of a molecular dynamics simulation that used a pair potential favoring the icosahedral local order. The vibrational properties have been investigated by using both a normal-mode analysis and by computing the spectra of appropriate time-correlation functions.

First, we have shown that it is possible to construct a structural model of a one-component σ-phase by means of molecular dynamics simulations using an appropriate pair potential. This σ-phase structure is stable in a wide range of thermodynamical parameters. Our model of the σ-phase contains only one atomic component. This is important in understanding the role of the topological icosahedral order alone on the structural and dynamical properties, and it avoids the effects arising from the presence of different atomic species.

Second, we have investigated atomic vibrational dynamics, phonon dispersion curves (figure 8.12), and vibrational density of states (figure 8.13) of the σ-phase. In particular, we have found

The vibrational properties have been investigated by using both a normal-mode analysis and by computing the spectra of appropriate time-correlation functions.

Figure 8.11. Projection down the c-axis of the σ-phase structure: (a) $3^2, 4, 3, 4$ net (the numerical symbols are Schläfli symbols, specifying the number and sequence of various polygons around each vertex). The dashed square outlines a unit cell; (b) Atomic arrangement in one unit (cubic) cell. ◊: $z = 0$, ♦: $z = 0.5$, •: $z = 0.2499$. ×: $z = 0.2501$, ○: $z = 0.7499$, □: $z = 0.7501$, ◯: Z12 atoms, ☐: Z15 atoms. The rest of the atoms are Z14, Z denoting the coordination number (number of the nearest neighbors). Multiplying z by the proper c/a ratio gives a tetragonal unit cell with $a = 1$.

(a)

(b)
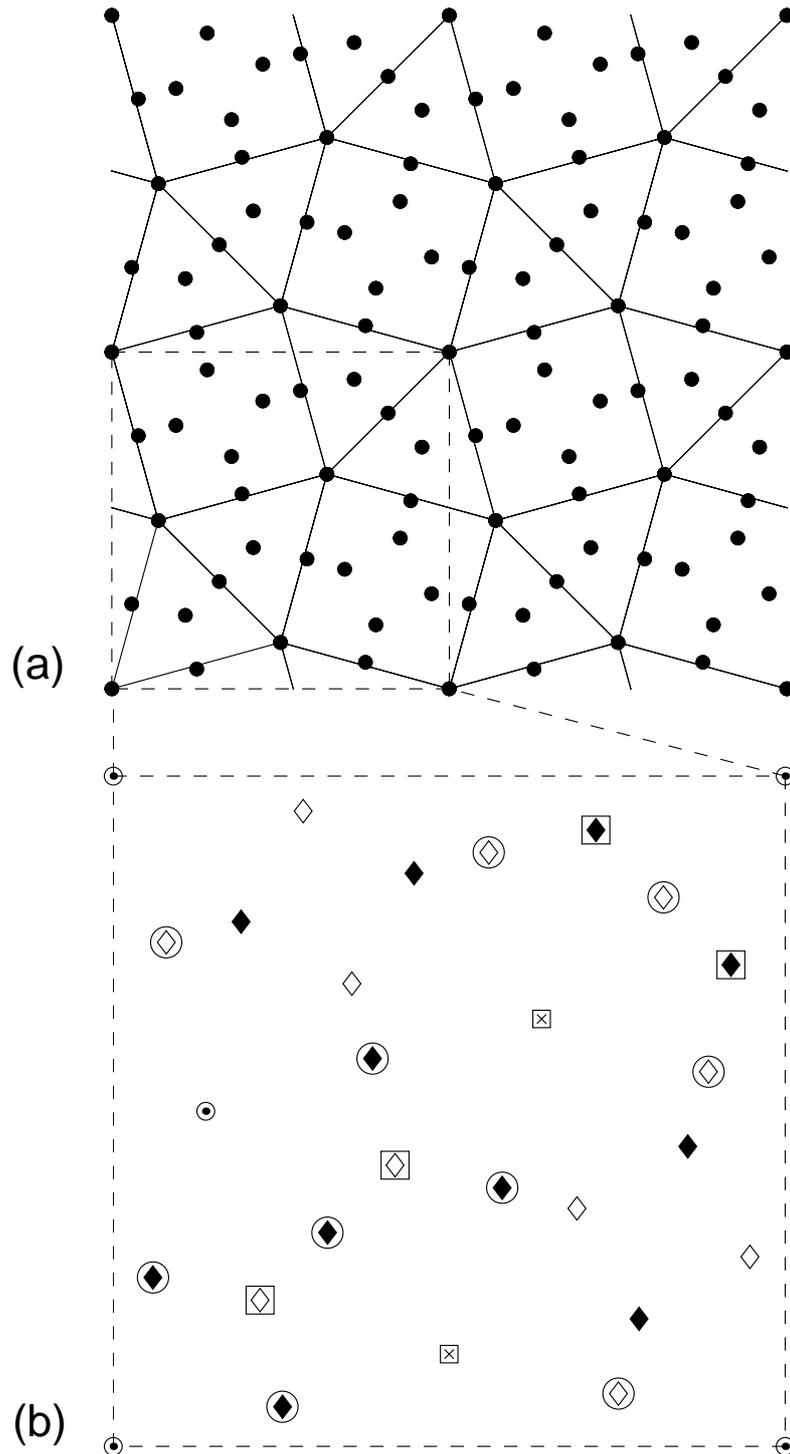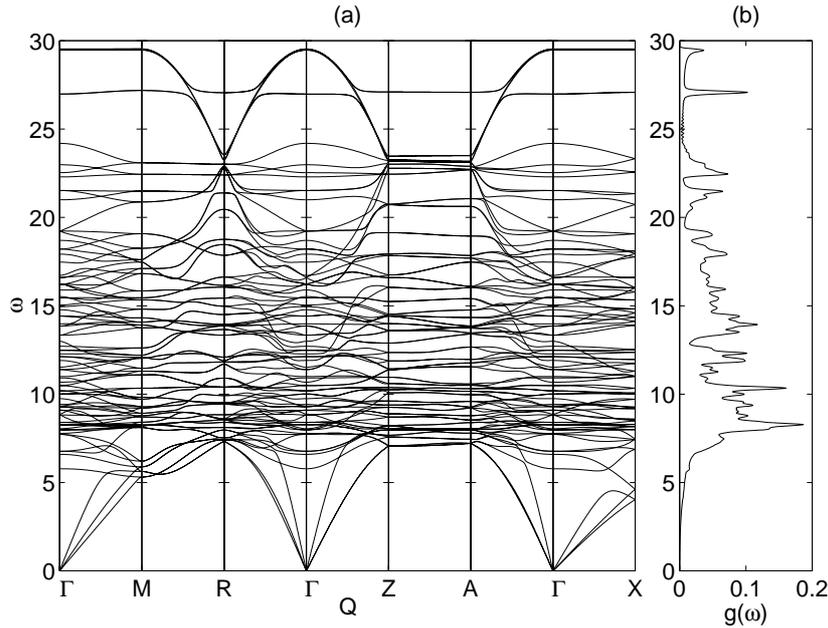
Figure 8.12. (a) phonon-dispersion relations and (b) vibrational density of states evaluated by a normal-mode analysis in the harmonic approximation. The symmetry points on the surface of the first Brillouin zone are $\Gamma = (0,0,0)$, $M = (\frac{\pi}{a}, \frac{\pi}{a}, 0)$, $R = (\frac{\pi}{a}, \frac{\pi}{a}, \frac{\pi}{c})$, $Z = (0, 0, \frac{\pi}{c})$, $A = (\frac{\pi}{a}, 0, \frac{\pi}{c})$, $X = (\frac{\pi}{a}, 0, 0)$.

the range of applicability of the harmonic approximation in a description of atomic dynamics. We have also demonstrated the existence of soft modes in the σ-phase, which leads to a structural phase transformation with increasing pressure.

Third, we have demonstrated that the σ-phase is a good crystalline counterpart of the IC glass. This study has been done on the basis of a comparative analysis of the vibrational dynamics (vibrational density of states). See figure 8.13.

We believe that the results for the vibrational properties of the σ-phase can be used in an analysis of the peculiar vibrational properties of the IC glass. We also believe that the computational data of the vibrational properties of the σ-phase can be of value for metallurgy, where this phase has received much detailed attention, chiefly because of the detrimental effect that the formation of this phase has on mechanical properties of certain steels.

The results presented here were obtained by using an efficient molecular dynamics code developed by the authors. The code is optimized for the use of RISC architectures. For system sizes of about twenty thousand particles, characteristic for this study, we use one SMP node on the IBM SP.

For details and a full list of references, see [Simdyankin *et al.*,

Figure 8.13. Vibrational densities of states calculated from the velocity autocorrelation function for the σ-phase structure and the corresponding glass at the reduced temperatures shown. Both results are obtained at the same density $\rho = 0.8771$.
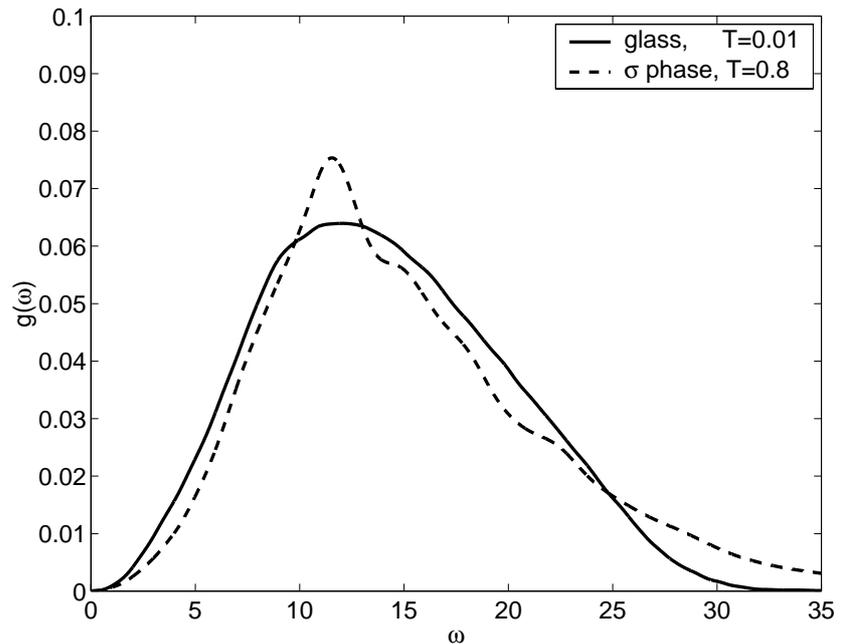
2000].

8.12 Two-Photon QED Corrections in Helium-Like Highly Charged Ions

Björn Åsén, Martin G. H. Gustavsson, Per Sunnergren,
Sten Salomonson
Department of Physics, CTH

The basic theory of electronic structure is quantum electrodynamics, QED, which describes how the electron field interacts with the electromagnetic field. The interest in QED applications to atomic systems, bound-state QED, has been enhanced significantly in recent years, mainly through the experimental success in producing and studying highly charged ions. These heavy few-electron systems are extremely relativistic and provide an excellent test of both relativity and QED in a region not previously carefully investigated.

The interest in QED applications to atomic systems, bound-state QED, has been enhanced significantly in recent years.

The interactions between the electrons are described as the exchange of photons. The coupling constant $\alpha \approx 1/137$, which is characteristic for the emission and the subsequent reabsorption

of a photon by the electrons, is small compared to unity. Because of this, it is appropriate to make an expansion of the total electromagnetic interaction in terms of the number of exchanged photons.

The electrons in an atom are propagating in the field from the nucleus, with charge number Z. For these systems it is sufficient to treat the nuclear field as a classical field. As a first step, we can approximate the nucleus as an infinitely heavy fixed particle in relation to the electron. We can then solve the Dirac equation for an electron in a static Coulomb field and consider the solutions as describing the electron field. The effect of nuclear recoil and other effects that are left out of this approximation can be treated separately, as small corrections.

The old methods of solving bound-state QED problems were mainly restricted to lighter systems, where it is appropriate to make an expansion of the interaction between the electron and the nucleus. The characteristic coupling constant of this expansion is $Z\alpha$, which tends to unity for heavy systems. To obtain sufficient accuracy in this high Z region, it is thus essential to treat most of the problems without using the $Z\alpha$ expansion. The problem is to give an adequate description of electrons moving in a strong nuclear field. This cannot be done strictly analytically; in combination with numerical techniques, however, we can obtain a rigorous calculation scheme. The development of finite basis-sets to construct the electron propagators has simplified the building scheme of bound-state QED calculations, and we can now evaluate many complicated processes in a more straightforward manner than we could before.

The one-photon exchange between the electrons is shown in figure 8.14. We have made substantial work on the corrections to this first-order effect, in the ground state of helium-like ions. These corrections come from the exchange of two photons between the electrons, or the so-called non-radiative effects (see figure 8.15 [a] and [b]), and the two-electron radiative effects (see figure 8.15 [c]–[f]).

We are now performing such QED calculations on excited states in helium-like systems. For heavy ions, the two-electron radiative effects are expected to provide significant contributions compared to the experimental accuracy. Even for medium-heavy elements, there are unexplained deviations between accurately measured

Figure 8.14. Feynman diagram representing the one-photon exchange process. The double lines denote an electron propagating in an atomic potential field, and the wavy line denotes a propagating photon.
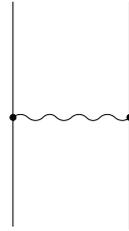
Figure 8.15. Feynman diagrams representing the two-photon contribution to the electron-electron interaction for helium-like ions. The first row—the "ladder" (a) and the "crossed-photon" (b) diagrams—represents the non-radiative effects, and the remaining diagrams represent the two-electron radiative effects.
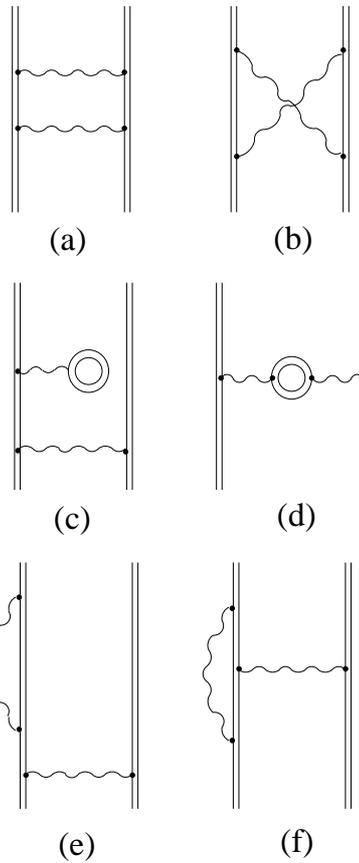
fine-structure splittings and corresponding calculations based on the $Z\alpha$ expansion method. We hope to be able to shed light on these discrepancies. The generalization to excited states is non-trivial and leads to new complications due to the retardation of the exchanged photon. One also has to be careful with new pole contributions. Another problem is the approximate degeneracy between, for example, $1s\,2p_{1/2}$ and $1s\,2p_{3/2}$, where $J = 1$, which is more accentuated for lighter elements. This problem is well known in many-body theory, where it is solved by using an extended model space. A similar approach probably has to be developed for evaluating the QED effects.

The calculations contain a number of multidimensional numerical integrations, which scale as N^5. The number of grid points (N) is typically equal to 300. We have now parallelized these integrations, using MPI programming. The programs have been executed on the IBM SP computer, and when this procedure is analyzed, it seems that we obtain an almost-linear net gain in speed.

In summary, MPI programming has worked out very well for our codes. Because our calculations are easily partitioned, without too much inter-node communication, we obtain good scalability with the number of nodes allocated.

8.13 Velocity Distributions of Fractured Random Media

Lena Frenje, Christopher Juhlin
Institute of Earth Sciences, Uppsala University

Summary

We are using the IBM SP to perform numerical modeling of seismic waves propagating through random media. Our recent research has been focused on the random models and the way we generate them, with the aim to find a better way to simulate heterogeneous rock. We show that velocity logs from fractured areas are better described using a lognormal distribution than a Gaussian one. Often a Gaussian distribution is assumed. Lognormal random models can be obtained easily from Gaussian models through a simple transformation, without losing properties such as fractal dimension and correlation length. Synthetic logs extracted from lognormal media compare well with real logs from fractured areas. We also give examples of synthetic VSP data produced with

We show that velocity logs from fractured areas are better described using a lognormal distribution than a Gaussian one.

3D finite difference modeling in lognormal media and their corresponding Gaussian media.

Introduction

Modeling seismic waves in random media is quite commonly used when studying a heterogeneous crust [Frankeland and Clayton, 1986, Frenje and Juhlin, 1998]. One approach for obtaining the parameters needed to generate the random medium is to extract them from borehole sonic logs [Holliger, 1996]. The random medium most often used is a self-similar medium that has a Gaussian velocity distribution and can be described by a von Karman correlation function [Goff and Jordan, 1988]. However, in some fractured areas this Gaussian distribution appears to be a poor assumption. We show that the velocity variations observed in many sonic logs are better described by a lognormal distribution than a Gaussian one. We also show how to generate lognormal media and that synthetic logs extracted from these models compare better with real logs.

Real Logs

In figure 8.16 the P-wave sonic log from three different boreholes in the Baltic Shield are shown. Below each log is the distribution of the velocity variations plotted, after a linear trend has been removed. The assumption that the distribution is Gaussian is clearly not the case for these logs, especially for the Gravberg sonic log (figure 8.16a). A lognormal distribution describes the variations better (figure 8.17). The Gravberg borehole penetrates mainly granitic rock that is highly fractured in the upper 1200 meters. Several authors [Moos and Zoback, 1983, Leary, 1991, Holliger, 1996] have pointed out that fracturing in crystaline rock will reduce the sonic velocities, not increase them, introducing a low velocity tail on the distribution. A normalized lognormal distribution can be described by

$$f(v) = \frac{1}{(C_v^2 + 1)(1 - \frac{C_v}{\sigma}v)} \exp\left[-\frac{\left(\ln\left(\frac{\sigma}{C_v} - v \right) - \bar{v}_{tmp} \right)^2}{2\sigma_{tmp}^2} \right], \quad (8.4)$$

where

$$\sigma_{tmp} = \sqrt{\ln\left(C_v^2 + 1\right)}, and \qquad (8.5)$$

$$\bar{v}_{tmp} = \ln\left(\frac{\sigma}{C_v}\right) - \frac{\sigma_{tmp}^2}{2} \qquad (8.6)$$

are fitted to the distribution in figure 8.17 by adjusting σ, the standard deviation, and C_v, a measure of the skewness of the distribution. A Gaussian distribution is also plotted, for comparison.

Synthetic Models and Comparison with Real Logs

To obtain a lognormal medium, we start by generating a Gaussian medium, v_{gauss}, with the desired properties (Hurst number, correlation length) and standard deviation, σ_{tmp}, according to equation 8.5. The lognormal medium, v_{ln}, is then obtained by

$$v_{ln} = \frac{\sigma}{C_v} - \exp\left[v_{gauss} + \bar{v}_{tmp}\right]. \qquad (8.7)$$

Figure 8.18 shows the Gravberg sonic log in comparison with synthetic logs extracted from a Gaussian and a lognormal random 2D model. The models have the same standard deviation. Inspection of their correlation functions and power spectra show that they have roughly the same properties regarding Hurst number and correlation length. It is clear that the lognormal log, with its dominance of low velocities, compares better with the Gravberg log than the Gaussian one.

Synthetic Seismograms

To investigate the significance of using a lognormal medium as compared to a Gaussian one, we have generated synthetic VSP seismograms using 3D finite difference modeling of the acoustic wave equation, for both a lognormal and a Gaussian medium with the same characteristics as the logs in figure 8.18. The result of the modeling is plotted in figure 8.19, with no processing applied to the data. Both cases show a distinct first arrival followed by scattered energy, but the lognormal model appears to produce somewhat more scattering than the Gaussian one. However, to be able to quantify the differences a more thorough investigation needs to be done.

Figure 8.16. P-wave sonic logs from (a) the Gravberg-1 borehole in Siljan, Central Sweden, (b) the Olkiluoto-KR4 orehole in northern Finland, (c) the KAS02 borehole in Äspö, southeastern Sweden and their respective velocity distributions, after removal of a linear trend.
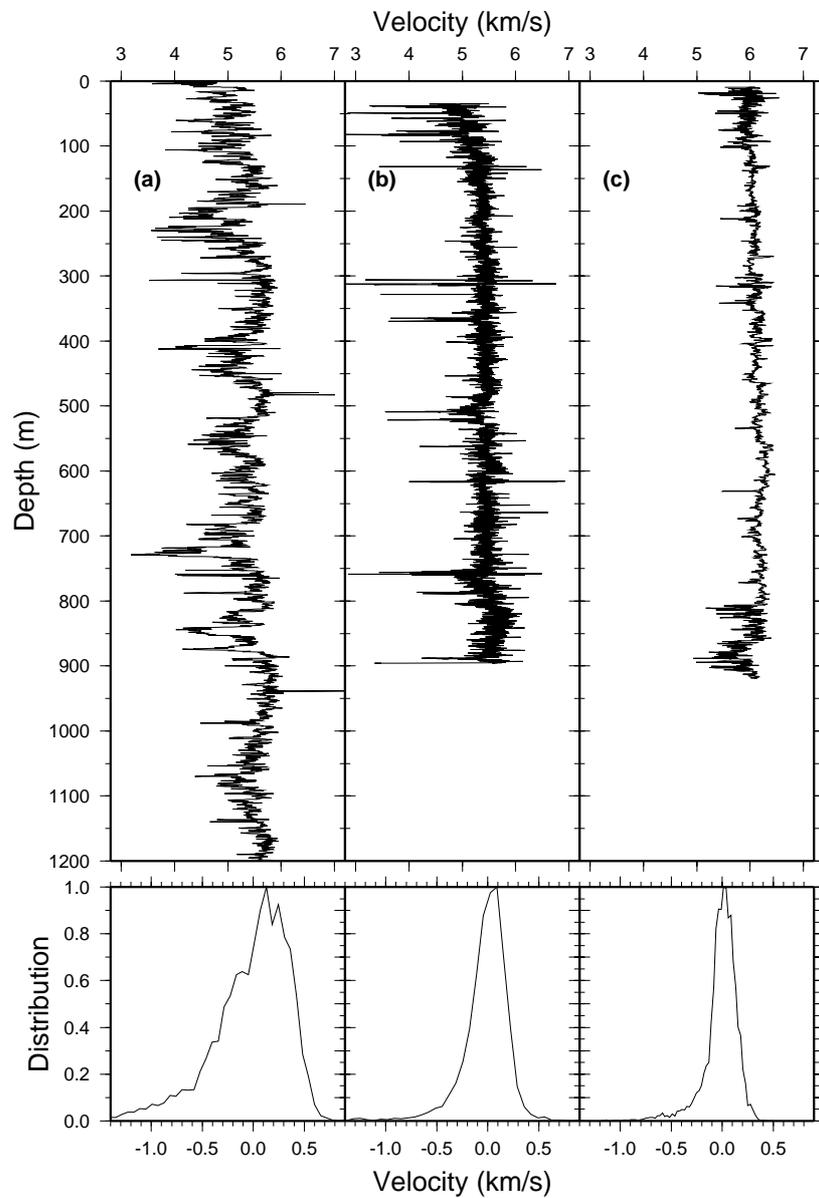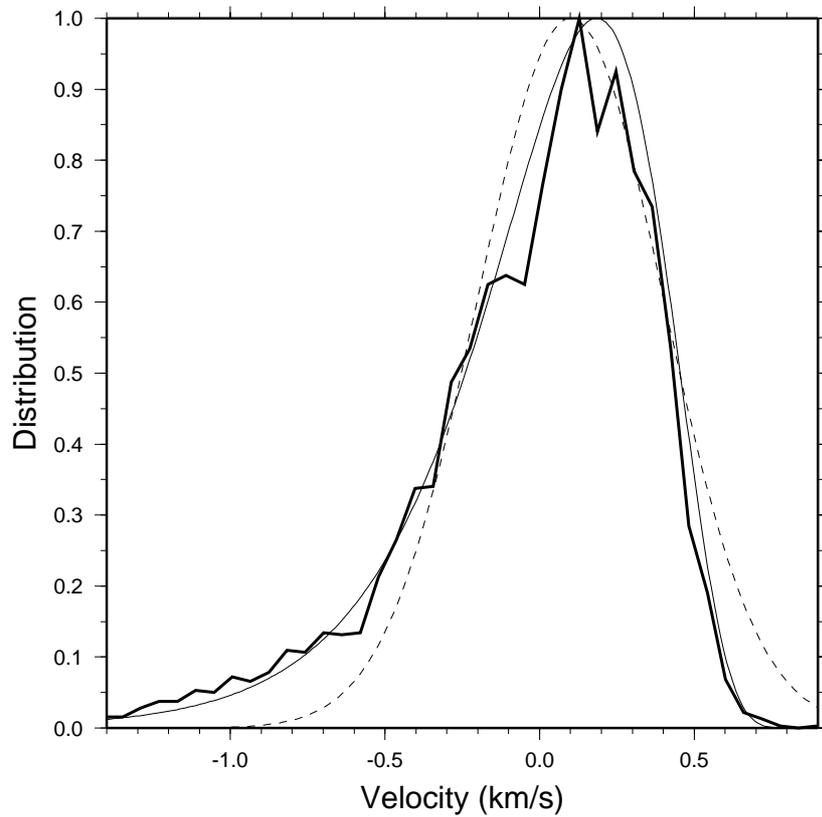
Figure 8.17. Velocity distribution in the upper 1200 m of the Gravberg-1 borehole fitted to a log-normal distribution (solid line) and Gaussian distribution (dashed line).

Figure 8.18. Comparison of synthetic logs extracted from (a) a Gaussian medium and (b) a log-normal medium. Both media have a standard deviation of $370\,\mathrm{m/s}$, a Hurst number of 0.18, and $45\,\mathrm{m}$ correlation length: values obtained from analysis of the Gravberg-1 sonic log (c).
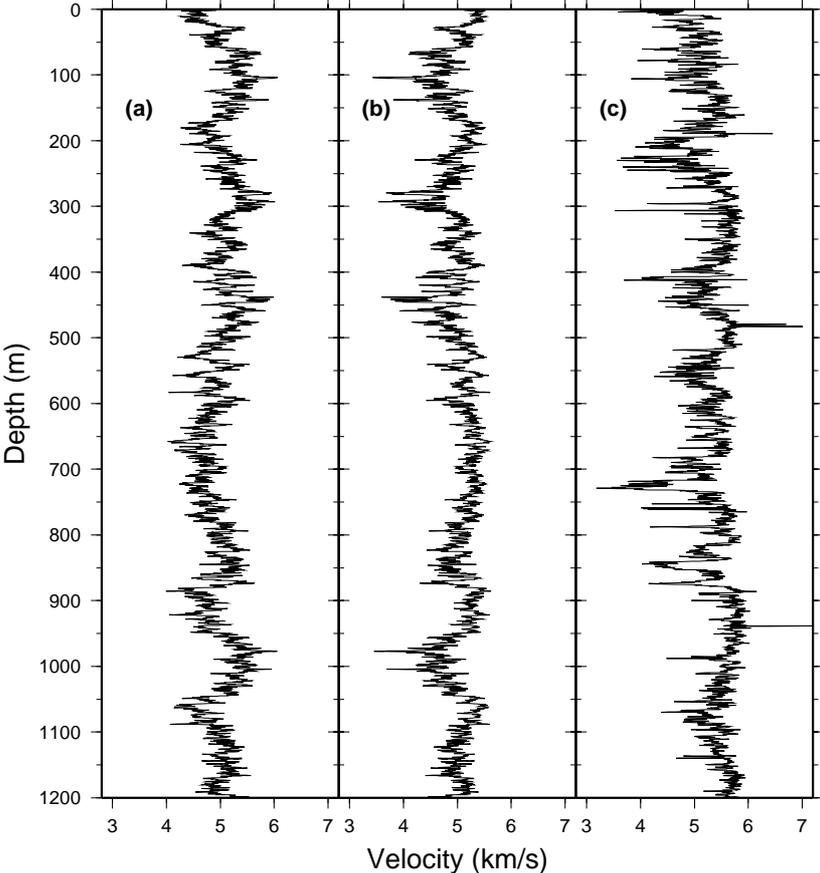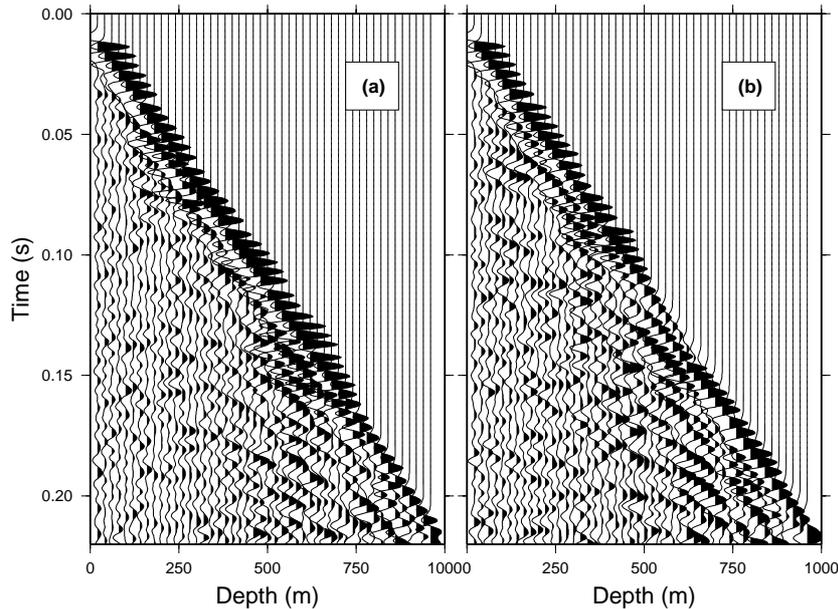
Figure 8.19. Comparison of synthetic VSP data from (a) a Gaussian and (b) a lognormal medium. The modeling was performed on a $256 \times 256 \times 512$ grid, with $2\,m$ grid spacing and $0.1\,ms$ time step. The source is a plane Ricker wavelet with a main frequency of $100\,Hz$ located at the surface.

Resources Used at PDC

To generate a realistic 3D velocity model that is large enough to be geologically significant, an array size of 512^3 nodes is normal. When performing the numerical modeling, we divide the model onto 3–10 nodes, which makes it possible to have large models with minimum runtime. However, to generate a random model a threed Fourier Transform is necessary. This is done using only one processor and allocating memory that is at least twice the size of the model; for a 512^3-sized model, about $1.1\,Gbyte$ memory is needed. Here, the larger nodes (Z and G nodes) with $1\,Gbyte$ and $2\,Gbyte$ RAM, respectively, are used. Without the large nodes, it would be impossible to generate these large models. A few large nodes to generate the models and a larger number of smaller nodes to do the actual modeling on is, for our research, the best combination.

Conclusion

Using a model with a lognormal velocity distribution is better when trying to simulate fractured rock, because the lognormal distribution allows for the dominance of low-velocity fluctuations

caused by the fractures.

Bibliography

[Alonso *et al.*, 1998] ALONSO, D. A., BRANDT, P., NORDIN, S., AND AN-DERSSON, P. G. (1998). Ru(Arene)(Aminoalcohol)-Catalyzed Transfer Hydrogenation of Ketones: The Mechanism and the Origin of the Enantioselectivity. Submitted. 39

[Andersson, 1998a] ANDERSSON, U. (1998a). Parallelization of a 3D FD-TD Code for the Maxwell Equations Using MPI. In: *EMB 98 – Electromagnetic Computations for Analysis and Design of Complex Systems*, edited by G. Kristensson. SNRV, November 1998, p. 94–101. 122

[Andersson, 1998b] ANDERSSON, U. (1998b). Parallelization of a 3D FD-TD Code for the Maxwell Equations Using MPI. In: *Applied Parallel Computing, PARA'98*, edited by B. Kågström *et al*, Lecture Notes in Computer Science, No. 1541, June 1998, p. 12–19. 122

[Aranyos *et al.*, 1999] ARANYOS, A., CSJERNYIK, G., SZABO, K. J., AND BÄCKVALL, J.-E. (1999). Evidence for a Ruthenium Dihydride Species as the Active Catalyst in the $RuCl_2(PPh_3)_3$-Catalyzed Hydrogen Transfer Reaction in the Presence of Base. *Chem. Commun.* **4**: 351–352. 37

[Aranyos *et al.*, 1998] ARANYOS, A., SZABO, K. J., AND BÄCKVALL, J.-E. (1998). Palladium-Catalyzed 1,4-Acetoxy-Trifluoroacetoxylation of Cyclic 1,3-Dienes. Scope and Mechanism. *J. Org. Chem.* **63**: 2523–2529. 37

[Baldwin and Lomax, 1978] BALDWIN, B. S. AND LOMAX, H. (1978). Thin Layer Approximation and Algebraic Model for Separated Turbulent Flows. Technical Report Paper 78-257, AIAA. 95

[Ballone and Andreoni, 1999] BALLONE, P. AND ANDREONI, W. (1999). *Metal Clusters*. New York: John Wiley and Sons. 31

[Becke, 1988] BECKE, A. D. (1988). Density-Functional Exchange-Energy Approximation with Correct Asymptotic Behavior. *Phys. Rev. A* **38**: 3098. 31, 31

[Bengtsson *et al.*, 2000] BENGTSSON, L., SVENSSON, K., HASSEL, M., BELLMAN, J., PERSSON, M., AND ANDERSSON, S. (2000). H_2 Adsorbed in a 2D Quantum-Rotor State on a Stepped Copper Surface. *Phys. Rev. B* **61**: 16921. 113

[Ben, 1998] Bently Nevada Corporation. (1998). *Aeroelasticity in Turbomachines: Effects of Coupling Modelling and Blade Material Changes*, 1998. 116

[Berendsen *et al.*, 1995] BERENDSEN, H. J. C., VAN DER SPOEL, D., AND VAN DRUNEN, R. (1995). GROMACS: A Message-Passing Parallel Molecular Dynamics Implementation. *Comp. Phys. Comm.* **95**: 43–56. 16

[Berger *et al.*, 1997a] BERGER, O., EDHOLM, O., AND JÄHNIG, F. (1997a). Molecular Dynamics Simulation of a Fluid Bilayer of Dipalmiotylphosphatidylcholine at Full Hydration, Constant Pressure and Constant Temperatur. *Biophys. J* **72**: 2002–2013. 17

[Berger *et al.*, 1997b] BERGER, O., EDHOLM, O., AND JÄHNIG, F. (1997b). Molecular Dynamics Simulations of a Fluid Bilayer of Dipalmitoylphosphatidylcholine at Full Hydration, Constant Pressure and Constant Temperature. *Biophysical Journal* **72**: 2002–2013. 16

[Bertini *et al.*, 1999] BERTINI, I., KOWALEWSKI, J., LUCHINAT, C., NILSSON, T., AND PARIGI, G. (1999). Nuclear Spin Relaxation in Paramagnetic Complexes of $S = 1$: Electron Spin Relaxation Effects. *J. Chem. Phys* **111**: 5795–5807. 126

[Brandt *et al.*, 1999] BRANDT, P., HEDBERG, C., LAWONN, K., PINHO, P., AND ANDERSSON, P. G. (1999). A Theoretical and Experimental Study of Asymmetric Dialkylzinc Additions to N-(Diphenylphosphinoyl) Benzalimin. *Chem. Eur. J.* **5**: 1692. 38

[Brinck *et al.*, 1999] BRINCK, T., LEE, H. N., AND JONSSON, M. (1999). Quantum Chemical Studies on the Thermochemistry of Alkyl and Peroxyl Radicals. *J. Phys. Chem. A* **103**: 7094. 24

[Brown *et al.*, 1998] BROWN, J. T., ALLEN, M. P., DEL RÍO, E. M., AND DE MIGUEL, E. (1998). Effects of Elongation on the Phase Behaviour of the Gay-Berne Fluid. *Phys. Rev. E* **57**: 6685. 51

[Car and Parrinello, 1985] CAR, R. AND PARRINELLO, M. (1985). Unified Approach for Molecular Dynamics and Density-Functional Theory. *Phys. Rev. Lett.* **55**: 2471. 30

[Cella, 1998] CELLA, U. (1998). Assessment of Physical and Numerical Models in NSMB for Flow around Aerofoils and Wings. Master's thesis, Royal Institute of Technology (KTH), Stockholm, Sweden. 95

[Ceperley and Adler, 1980] CEPERLEY, D. M. AND ADLER, B. J. (1980). Ground State of the Electron Gas by a Stochastic Method. *Phys. Rev. Lett.* **45**: 566. 31

[Chandrasekhar, 1992] CHANDRASEKHAR, S. (1992). *Liquid Crystals*. Cambridge: Cambridge University Press. 51, 53

[Crasemann, 1998] CRASEMANN, B. (1998). Synchrotron Radiation in Atomic Physics. *Can. J. Phys.* **76**: 251–272. 55

[Crawford *et al.*, 1991] CRAWFORD, J. F., DAUM, M., FROSCH, R., JOST, B., KETTLE, P. R., MARSHALL, R. M., WRIGHT, B. K., AND ZIOCK, K. O. H. (1991). Precision Measurement of the Pion Mass Difference $m_{\pi^-} - m_{\pi^0}$. *Phys. Rev. D* **43**:46. 118

[Davidson and Farhanieh, 1992] DAVIDSON, L. AND FARHANIEH, B. (1992). CALC-BFC: A Finite-Volume Code Employing Collocated Variable Arrangement and Cartesian Velocity Components for Computation of Fluid Flow and Heat Transfer in Complex Three-Dimensional Geometries. Technical Report 92/4, Deptment of Thermo and Fluid Dynamics, Chalmers University of Technology, Gothenburg. 88

[De Kerpel *et al.*, 1998] DE KERPEL, J. O. A., PIERLOOT, K., RYDE, U., AND ROOS, B. O. (1998). Theoretical Study of the Electronic Spectrum of Stellacyanin. *J. Phys. Chem. B* **102**:4638–4647. 49

[De Kerpel and Ryde, 1998] DE KERPEL, J. O. A. AND RYDE, U. (1998). Protein Strain in Blue Copper Proteins Studied by Free Energy Perturbations. *Proteins: Struct. Funct. Genet.* **36**:157–174. 49

[de Try, 1999] DE TRY, F. (1999). Computational Study of Vortex Behavior over 70° Swept Delta Wings in Wind Tunnels. Master's thesis, Royal Institute of Technology (KTH), Department of Aeronautics, Stockholm. 79

[Draine, 1988] DRAINE, B. T. (1988). The Discrete-Dipole Approximation and its Application to Interstellar Graphite Grains. *Astrophys. J.* **333**:848–872. 134, 134

[Draine and Flatau, 1994] DRAINE, B. T. AND FLATAU, P. J. (1994). The Discrete-Dipole Approximation for Scattering Calculations. *J. Opt. Soc. Am. A* **11**:1491–1499. 134

[Draine and Goodman, 1993] DRAINE, B. T. AND GOODMAN, J. (1993). Beyond Clausius-Mossotti: Wave Propagation on a Polarizable Point Lattice and the Discrete Dipole Approximation. *Astrophys. J.* **405**:685–697. 134

[Draper *et al.*, 1998] DRAPER, D., PEREIRA, A., PRADO, P., SALTELLI, A., CHEAL, A., EGUILIOR, S., MENDES, B., AND TARANTOLA, S. (1998). Scenario and Parametric Uncertainty in GESAMAC: A Case Study in Nuclear Waste Disposal Risk Assessment. Forthcoming, *Computational Physics Communication.* 133

[Draper *et al.*, 1999] DRAPER, D., PEREIRA, A., PRADO, P., SALTELLI, A., CHEAL, A., EGUILIOR, S., MENDES, B., AND TARANTOLA, S., (1999). GESAMAC, Final report. To appear. 133

[Edholm, 1998] EDHOLM, O., (1998). Surface Tension in Lipid Bilayers from Molecular Dynamics Simulations. Manuscript. Submitted December 1998. 18

[Egberts *et al.*, 1994] EGBERTS, E., MARRINK, S., AND BERENDSEN, H. (1994). Molecular Dynamics Simulation of a Phospholipid Membrane. *Eur. Biophys. J.* **22**: 423–436. 16

[Eguilior and Prado, 1995] EGUILIOR, S. AND PRADO, P., (1995). GESAMAC Technical Annex. Conceptual and Computational Tools to Tackle Long-Term Risk from Nuclear Waste Disposal in the Geosphere. Geosphere Modeling, Geosphere Sensitivity Analysis, Model Uncertainty in Geosphere Modeling, Advanced Computing in Stochastic Geosphere Simulation. Contract FI4W/CT95/0017. 132

[Eguilior and Prado, 1998] EGUILIOR, S. AND PRADO, P., (1998). GTM-CHEM Computer Code: Description and Application to the Level E/G Test Case (GESAMAC Project). CIEMAT/DIAE/550/55900/14/98. 133

[Einarsdotter *et al.*, 1997] EINARSDOTTER, K., SADIGH, B., GRIMVALL, G., AND OZOLINS, V. (1997). Phonon Instabilities in fcc and bcc Tungsten. *Phys. Rev. Lett.* **79**: 2073–2076. 111

[Eklund *et al.*, 1988] EKLUND, D., BADINAND, T., AND FRANSSON, T. (1988). A Numerical Study of Radiation Effects in a Gas Turbine Combustion Chambers. In: *34th AIAA/ASME/SAE/ASEE Joint Propulsion Conference & Exhibit*, Cleveland, OH. 92

[Engström *et al.*, 2000a] ENGSTRÖM, M., HIMO, F., AND ÅGREN, H. (2000a). *Ab Initio g*-Tensor Calculations of the Thioether Substituted Tyrosyl Radical in Galactose Oxidase. *Chem. Phys. Lett.* **319**: 191–196. 36

[Engström *et al.*, 2000b] ENGSTRÖM, M., HIMO, F., GRÄSLUND, A., MINAEV, B., VAHTRAS, O., AND ÅGREN, H. (2000b). Hydrogen Bonding to the Tyrosyl Radical Analyzed by *Ab Initio g*-Tensor Calculations. *J. Phys. Chem. A* **104**: 5149–5153. 35

[Engström *et al.*, 1999a] ENGSTRÖM, M., OWENIUS, R., AND LINDGREN, M. (1999a). Solvent Effects on Nitroxide Spin Labels. Manuscript in preparation. 36

[Engström *et al.*, 1999b] ENGSTRÖM, M., VAHTRAS, O., AND ÅGREN, H. (1999b). Hartree-Fock Linear Response Calculations of *g*-Tensors of Substituted Benzene Radicals. *Chem. Phys.* **243**: 263–271. 35

[Engström *et al.*, 2000] ENGSTRÖM, M., VAHTRAS, O., AND ÅGREN, H. (2000). MCSCF and DFT Calculations of EPR Parameters of Sulfur-Centered Radicals. *Chem. Phys. Lett.* **328**: 483–491. 36

[Evans and Morriss, 1990] EVANS, D. J. AND MORRISS, G. P. (1990). *Statistical Mechanics of Nonequilibrium Liquids*. London: Academic Press. 53

[Feifel and *et al.*, 2000] FEIFEL, R. *et al.* (2000). Observation of a Continuum-Continuum Interference Hole in Ultrafast Dissociating Core-Excited Molecules. *Phys. Rev. Lett.* **85**: 3133–3136. 55

[Frankeland and Clayton, 1986] FRANKELAND, A. AND CLAYTON, R. W. (1986). Finite Difference Simulations of Seismic Scattering: Implications for the Propagation of Short-Period Seismic Waves in the Crust and Models of Crustal Heterogeneity. *J. Geophys. Res* **91**: 6465–6489. 144

[Frenje and Juhlin, 1998] FRENJE, L. AND JUHLIN, C. (1998). Scattering of Seismic Waves Simulated by Finite Difference Modelling in Random Media: Application to the Gravberg-1 Well, Sweden. *Tectonophysics* **293**: 61–68. 144

[Frisch and *et al.*, 1998] FRISCH, M. J. *et al.* (1998). *Gaussian 98, Revision A.7*. Gaussian, Inc., Pittsburgh, PA, 1998. 37

[Gacherieu and Weber, 1998] GACHERIEU, C. AND WEBER, C. (1998). Assessment of Algebraic and One-Equation Turbulence Models for the Transonic Turbulent Flow around a Full Aircraft Configuration. Technical Report Paper 98-2737, AIAA. 94

[Gay and Berne, 1981] GAY, J. G. AND BERNE, B. J. (1981). Modification of the Overlap Potential to Mimic a Linear Site-Site Potential. *J. Chem. Phys.* **74**: 3316. 51

[Gel'mukhanov and Ågren, 1996] GEL'MUKHANOV, F. AND AGREN, H. (1996). X-ray Resonant Scattering Involving Dissociative States. *Phys. Rev. A* **54**: 379–393. 55

[Gel'mukhanov and Ågren, 1999] GEL'MUKHANOV, F. AND ÅGREN, H. (1999). Resonant X-ray Raman Scattering. *Phys. Rep.* **312**: 87–330. 55

[Goff and Jordan, 1988] GOFF, J. A. AND JORDAN, T. (1988). Stochastic Modeling of Seafloor Morphology: Inversion of Sea Beam Data for Second-Order Statistic. *J. Geophys. Res* **93**: 13,589–13,608. 144

[Golub and Van Loan., 1989] GOLUB, G. H. AND VAN LOAN., C. F. (1989). *Matrix Computations*. Baltimore: The John Hopkins University Press. 119, 119, 119

[Görtz, 1998] GÖRTZ, S. (1998). Computational Study of Vortex Breakdown over 70° Swept Delta Wings. Master's thesis, Royal Institute of Technology (KTH), Department of Aeronautics, Stockholm. 76

[Görtz *et al.*, 1999] GÖRTZ, S., RIZZI, A., AND MUNUKKA, K. (1999). Computational Study of Vortex Breakdown over Swept Delta Wings. Technical Report Paper 99-3118, AIAA. 78

[Grönbeck *et al.*, 1997] GRÖNBECK, H., ROSÉN, A., AND ANDREONI, W. (1997). *Ab Initio* Molecular Dynamics Investigations of Transition Metal Clusters. In: *PDC Progress Report*. Parallelldatorcentrum, p. 136–140. 31

[Grönbeck *et al.*, 1998] GRÖNBECK, H., ROSÉN, A., AND ANDREONI, W. (1998). Structural, Electronic, and Vibrational Properties of Neutral and Charged Nb_n ($n = 8, 9, 10$) Clusters. *Phys. Rev. A* **58**: 4630. 31

[Haeffner *et al.*, 1999] HAEFFNER, F., HU, C.-H., BRINCK, T., AND NORIN, T. (1999). The Catalytic Effect of Water in Basic Hydrolysis of Methyl Acetate: A Theoretical Study. *J. Mol. Struc. Theochem* **459**: 85. 23

[Hartford, 2000] HARTFORD, J. (2000). Interface energy and Electron Structure for Fe/VN. *Phys. Rev. B* **61**: 2221. 114

[Helgaker and *et al.*, 1997] HELGAKER, T. *et al.* (1997). *DALTON: A Second-Order MCSCF Molecular Property Program*, 1997. 37

[Hess *et al.*, 1997] HESS, B., BEKKER, H., BERENDSEN, H. J. C., AND FRAAIJE, J. G. E. M. (1997). LINCS: A Linear Constraint Solver for Molecular Simulations. *J. Comp. Chem.* **18**: 1463–1472. 17

[Hohenberg and Kohn, 1964] HOHENBERG, P. AND KOHN, W. (1964). Inhomogenous Electrons Gas. *Phys. Rev* **136**: 864. 30

[Holliger, 1996] HOLLIGER, K. (1996). Seismic Scattering in the Upper Crystalline Crust Based on Evidence from Sonic Logs. *Int. Geophys. J.* **128**: 65–72. 144, 144

[Hu and Brinck, 1999] HU, C.-H. AND BRINCK, T. (1999). Theoretical Studies of the Hydrolysis of the Methyl Phosphate Anion. *J. Phys. Chem. A* **103**: 5379. 23

[Hu *et al.*, 1998] HU, C. H., BRINCK, T., AND HULT, K. (1998). *Ab Initio* and Density Functional Theory Studies of the Catalytic Mechanism for Ester Hydrolysis in Serine Hydrolases. *Int. J. Quant. Chem.* **69**: 89. 23

[Irbäck and Sandelin, 1999] IRBÄCK, A. AND SANDELIN, E. (1999). Monte Carlo Study of the Phase Structure of Compact Polymer Chains. *J. Chem. Phys.* **110**: 12256–12262. 21

[Ismail-Zadeh *et al.*, 1998] ISMAIL-ZADEH, A. T., KOROTKII, A. I., NAIMARK, B. M., SUETOV, A. P., AND TSEPELEV, I. A. (1998). Implementation of a Three-Dimensional Hydrodynamic Model for Evolution of Sedimentary Basins. *Computational Mathematics and Mathematical Physic* **38**: 1138–1151. 108

[Ismail-Zadeh and Naimark, 1996] ISMAIL-ZADEH, A. T. AND NAIMARK, B. M. (1996). Gravitational Instability of Salt Layer and Relic Slab: Numerical Experiments. *TRITA-PDC Report* **4**: 24. 106

[Jacquet-Richardet *et al.*, 1996] JACQUET-RICHARDET, G., MOYROUD, F., AND FRANSSON, T. (1996). A Modal Coupling of Fluid and Structure Analyses for Turbomachine Flutter: Application to a Fan Stage. Technical Report 96-GT-335, ASME. 116

[Jacquet-Richardet *et al.*, 1997] JACQUET-RICHARDET, G., MOYROUD, F., AND FRANSSON, T. (1997). An Influence of Shroud Design on the Dynamic and Aeroelastic Behaviour of Bladed-Disk Assemblies. Technical Report 97-GT-191, ASME. 116

[Jameson, 1991] JAMESON, A. (1991). Time Dependent Calculations Using Multigrid, with Applications to Unsteady Flows Past Airfoils and Wings. Technical Report Paper 91-1596, AIAA. 84, 84

[Jonsell *et al.*, 1999] JONSELL, S., WALLENIUS, J., AND FROELICH, P. (1999). Influence of $pp\pi$ Ions on Pion Absorption in H_2. *Phys. Rev. A* **59**: 3440. 119

[Juozapavičius *et al.*, 1999] JUOZAPAVIČIUS, A., CAPRARA, S., AND ROSENGREN, A. (1999). Critical Properties and Phase Diagram of the Quantum Anisotropic XY Spin Chain in a Random Magnetic Field: A Density-Matrix Renormalization-Group Analysis. *Phys. Rev. B* **60**: 14771–14778. 129

[Kamimura, 1988] KAMIMURA, M. (1988). Nonadiabatic Coupled-Rearrangement-Channel Approach to Muonic Molecules. *Phys. Rev. A* **38**: 621. 119

[Karlsson and Brorsson, 1998] KARLSSON, S. AND BRORSSON, M. (1998). Producer-Push: A Protocol Enhancement to Page-Based Software Distributed Shared Memory System. Technical report, Department of Information Technology, Lund University, P.O. Box 118, SE-221 00 Lund, Sweden. Submitted for publication. 109

[Kevan and Gaylord, 1987] KEVAN, S. D. AND GAYLORD, R. H. (1987). High-Resolution Photoemission Study of the Electronic Structure of the Noble-Metal (111) Surfaces. *Phys. Rev. B* **36**: 5809. 32

[Kietzmann *et al.*, 1998] KIETZMANN, H., MORENZIN, J., BECHTHOLD, P. S., GANTEFÖR, G., AND EBERHARDT, W. (1998). Photoelectron Spectra of Nb_n^--Clusters: Correlation between Electronic Stucture and Hydrogen Chemisorption. *J. Chem. Phys.* **109**: 2275. 31

[Klopfer and Yoon, 1993] KLOPFER, G. AND YOON, S. (1993). Multizonal Navier-Stokes Code with the LU-SGS Scheme. Technical Report Paper 93-2965, AIAA. 84

[Kohn and Sham, 1965] KOHN, W. AND SHAM, L. J. (1965). Self-Consistent Equations Including Exchange and Correlation Effects. *Phys. Rev.* **140**: A1133. 30

[Larsson and Carlsson, 1998a] LARSSON, K. AND CARLSSON, J. O. (1998a). Adsorption of Gaseous Species to (111) Surfaces of b-SiC and Diamond. In manuscript. 47

[Larsson and Carlsson, 1998b] LARSSON, K. AND CARLSSON, J. O. (1998b). Surface Processes during Thin Film Growth of Diamond vs. c-BN. In manuscript. 47

[Larsson and Carlsson, 1999a] LARSSON, K. AND CARLSSON, J. O. (1999a). Partial Electron Transfer during Vapor Growth of Diamond on a (111) Surface. *J. Phys. Chem. B* **103**: 2735–2739. 47

[Larsson and Carlsson, 1999b] LARSSON, K. AND CARLSSON, J. O. (1999b). Surface Migration during Diamond Growth Studied by Molecular Orbital Calculations. *Phys. Rev. B* **59**: 8315–8322. 47

[Larsson and Carlsson, 1999c] LARSSON, K. AND CARLSSON, J. O. (1999c). Surface Processes in Cubic Boron Nitride Growth: A Theoretical Study. *J. Phys. Chem.* **103**: 6533–6538. 47

[Leary, 1991] LEARY, P. C. (1991). Deep Borehole Evidence for Fractal Distribution of Fractures in Crystalline Rock. *Int. Geophys. J.* **107**: 615–627. 144

[Lee *et al.*, 1988] LEE, C. L., YANG, W., AND PARR, R. G. (1988). Development of the Colle-Salvetti Correlation-Energy Formula into a Functional of the Electron Density. *Phys. Rev. B* **37**: 785. 31

[Lidmar and Wallin, 1999] LIDMAR, J. AND WALLIN, M. (1999). Superconducting Coherence and the Helicity Modulus in Vortex Line Models. *Phys. Rev. B* **59**: 8451–8454. 123

[Lindahl and Edholm, 1998] LINDAHL, E. AND EDHOLM, O. (1998). Solvent Diffusion outside Macromolecular Surfaces. *Physical Review E* **57**: 791–796. 16

[Linde and Thomas, 1996] LINDE, J. AND THOMAS, J. O. (1996). Molecular Dynamic Simulation of the Vanadium Pentoxide Gel Host. *Solid State Ionics* **85**: 1. 34

[Linse, 1999] LINSE, P. (1999). On the Convergence of Simulation of Charged Asymmetric Electrolytes. *J. Chem. Phys.* **110**: 3493–3501. 42

[Lobaskin and Linse, 1998a] LOBASKIN, V. AND LINSE, P. (1998a). Accurate Simulation of Highly Asymmetric Electrolytes with Charge Asymmetry 20:1 and 20:2. *J. Chem. Phys.* **109**: 2530. 42

[Lobaskin and Linse, 1998b] LOBASKIN, V. AND LINSE, P. (1998b). Computer Simulation Study of Highly Asymmetric Electrolyte with Charge Asymmetry 60:1. Hard-Sphere *vs.* Soft-Sphere Mode. Manuscript in preparation. 42, 42

[Lorente and Persson, 1999] Lorente, N. and Persson, M. (1999). Theory of Single-Molecule Vibrational Spectroscopy and Microscopy. Submitted to *Phys. Rev. Lett.* 114

[Lyubartsev and Laaksone, 1998] Lyubartsev, A. P. and Laaksone, A. (1998). Parallel Molecular Dynamics Simulations of Biomolecular System. In: *Applied Parallel Computing, PARA'98*, edited by B. Kågström *et al*, Lecture Notes in Computer Science, No. 1541, June 1998, p. 296–303. 18

[Malmlöf, 2000] Malmlöf, A. (2000). Investigation of Grid Topology for 70° Swept Delta Wings. Master's thesis, Royal Institute of Technology (KTH), Department of Aeronautics, Stockholm. 79

[Mårtensson *et al.*, 1997] Mårtensson, N., Weinelt, M., Karis, O., Magnuson, M., Wassdahl, N., Nilsson, A., Stöhr, J., and Samant, M. (1997). Coherent and Incoherent Processes in Resonant Photoemission. *Appl. Phys. A: Mater. Sci. Process.* **65**: 159–167. 55

[McGhee and Beasley, 1979] McGhee, R. J. and Beasley, W. D. (1979). Low-Speed Aerodynamic Characteristics of a 13-Percent-Thick Medium-Speed Airfoil Designed for General Aviation Application. Technical report, NASA Langley Research Center, Hampton, Virginia. 95, 96

[Mendes and Pereira, 1999] Mendes, B. and Pereira, A. (1999). *The PMCD Code: A Parallel Monte Carlo Driver*. Dept. of Physics, Stockholm University, 1999. In manuscipt. 132

[Moos and Zoback, 1983] Moos, D. and Zoback, M. D. (1983). *In Situ* Studies of Velocity in Fractured Crystalline Rock. *J. Geophys. Res* **88**: 2345–2358. 144

[Moyroud, 1997] Moyroud, F. (1997). Literature Review of Forced Response and Fatigue Problems in Turbomachines. Technical Report HPT/KTH 98/18, Department of Heat and Power Technology, KTH. 115

[Moyroud, 1998a] Moyroud, F. (1998a). *Fluid-Structure Integrated Computational Methods for Turbomachinery Blade Flutter and Forced Response Prediction*. PhD thesis, KTH and Institut National des Sciences Appliquées. 118

[Moyroud, 1998b] Moyroud, F. (1998b). Forced Response Analysis and High Cycle Fatigue Prediction of Bladed-Disk Assemblies, Milestone Report No. 1. Technical Report HPT/KTH 98/05, Department of Heat and Power Technology, KTH. 118

[Moyroud, 1998c] Moyroud, F. (1998c). Forced Response Analysis and High Cycle Fatigue Prediction of Bladed-Disk Assemblies, Milestone Report No. 2. Technical Report HPT/KTH 98/22, Department of Heat and Power Technology, KTH. 116

[Moyroud and Jacquet-Richardet, 1997] MOYROUD, F. AND JACQUET-RICHARDET, G. (1997). Reduced Order Models for the Free Vibrations and Forced Response of Mistuned Bladed-Disks. Technical Report HPT/KTH 98/19, Chair of Heat and Power Technology, KTH. 116

[Moyroud and Jacquet-Richardet, 1999a] MOYROUD, F. AND JACQUET-RICHARDET, G. (1999a). Finite Element Reduction Techniques for Mistuned Bladed-Disks, Part I: Theory and Simple Geometries. Submitted for publication at the ASME Turbo Expo Land Sea & Air '99, Indianapolis, IN. 116

[Moyroud and Jacquet-Richardet, 1999b] MOYROUD, F. AND JACQUET-RICHARDET, G. (1999b). Finite Element Reduction Techniques for Mistuned Bladed-Disks, Part II: Theory and Simple Geometries. Submitted for publication at the ASME Turbo Expo Land Sea & Air '99, Indianapolis, IN. 116, 117

[Moyroud et al., 1998] MOYROUD, F., JÖCKER, M., FRANSSON, T., AND JEANPIERRE, J. (1998). Design and Analysis of a Turbine with Extremely Large Blade Loads, KTH Study, Part 1: Literature Study. Technical Report HPT/KTH 98/21, Department of Heat and Power Technology, KTH. 115

[Muller and Rizzi, 1990] MULLER, B. AND RIZZI, A. (1990). Modelling of Turbulent Transonic Flow around Aerofoils and Wings. *Comm. in Applied Numerical Methods* **6**: 603–613. 95

[Nagle, 1993] NAGLE, J. (1993). Area/Lipid of Bilayers from NMR. *Biophysical Journal* **64**: 1476–1481. 16

[Neyertz et al., 1995] NEYERTZ, S., BROWN, D., AND THOMAS, J. O. (1995). Molecular Dynamics Simulations of the Amorphous Polymer Electrolyte PEOxNaI. *Computational Polymer Science* **5**: 107–120. 34

[Nilsson, 1997] NILSSON, H. (1997). A Parallel Multiblock Extension to the CALC-BFC Code Using PVM. Technical Report 97/11, Department of Thermo and Fluid Dynamics, Chalmers University of Technology, Gothenburg. 88

[Nilsson and Davidson, 1998] NILSSON, H. AND DAVIDSON, L. (1998). CALC-PVM: A Parallel Multiblock SIMPLE Multiblock Solver for Turbulent Flow in Complex Domains (in preparation). Technical report, Department of Thermo and Fluid Dynamics, Chalmers University of Technology, Gothenburg. 88

[Nilsson et al., 1998] NILSSON, T., SVOBODA, J., WESTLUND, P.-O., AND KOWALEWSKI, J. (1998). Slow-Motion Theory of Nuclear Spin Relaxation in Paramagnetic Complexes ($S = 1$) of Arbitrary Symmetry. *J. Chem. Phys* **109**: 6364–6375. 125

[Nordgren, 1997] NORDGREN, J. (1997). Recent Progress in Resonant Soft X-Ray Fluorescence Studies of Molecules. *J. Phys. IV (France)* **2**: C2–9–C2–20, Proceedings of the 9th International Conference on X-Ray Absorption Fine Structure. 55

[Odelius, 1999] ODELIUS, M. (1999). First Principle Study of the Dehydroxylation of Muscovite. Unpublished. 28

[Odelius *et al.*, 1997a] ODELIUS, M., BERNASCONI, M., AND PARRINELLO, M. (1997a). First Principles Study of the Structure of $2M_1$-Muscovite. Unpublished. 28

[Odelius *et al.*, 1997b] ODELIUS, M., BERNASCONI, M., AND PARRINELLO, M. (1997b). Two-Dimensional Ice Adsorbed on Mica Surface. *Phys. Rev. Lett.* **78**: 2855. 29, 29, 29, 29

[Olsson *et al.*, 1998a] OLSSON, M. H. M., PIERLOOT, K., RYDE, U., AND ROOS, B. O. (1998a). On the Relative Stability of Tetragonal and Tetrahedral Cu(II) Complexes with Relevance to the Blue Copper Proteins. *J. Biol. Inorg. Chem.* **3**: 109–125. 48, 48

[Olsson *et al.*, 1998b] OLSSON, M. H. M., RYDE, U., AND ROOS, B. O. (1998b). Quantum Chemical Calculations of the Reorganisation Energy of the Blue Copper Proteins. *Protein Science* **7**: 2659–2668. 49

[Perdew, 1986] PERDEW, J. P. (1986). Density-Functional Approximation for the Correlation Energy of the Inhomogeneous Electron Gas. *Phys. Rev. B* **33**: 8822. 31

[Perdew *et al.*, 1996] PERDEW, J. P., BURKE, K., AND ERNZERHOF, M. (1996). Generalized Gradient Approximation Made Simple. *Phys. Rev. Lett.* **77**: 3865. 31

[Perdew and Zunge, 1981] PERDEW, J. P. AND ZUNGE, A. (1981). Self-Interaction Correction to Density-Functional Approximations for Many-Electron Systems. *Phys. Rev. B* **23**: 5048. 31

[Persson *et al.*, 1999] PERSSON, M., STRÖMQUIST, J., BENGTSSON, L., JACKSON, B., SHALASHILIN, D., AND HAMMER, B. (1999). A First-Principles Potential Energy Surface for Eley-Rideal Reaction Dynamics of H Atoms on Cu(111). *J. Chem. Phys.* **110**: 2240. 113

[Piancastelli *et al.*, 2000] PIANCASTELLI, M. N., FINK, R. F., FEIFEL, R., BÖSSLER, M., SORENSEN, S. L., MIRON, C., WANG, H., HJELTE, I., BJÖRNEHOLM, O., AUSMEES, A., SVENSSON, S., SAŁEK, P., GEL'MUKHANOV, F. K., AND ÅGREN, H. (2000). Bond-Distance-Dependent Decay Probability of the N 1s-π^* Core-Excited State in N_2. *J. Phys. B.* **33**: 1819–1826. 55

[Pierloot *et al.*, 1998] PIERLOOT, K., DE KERPEL, J. O. A., OLSSON, M. H. M., RYDE, U., AND ROOS, B. O. (1998). Relation between the

Structure and Spectroscopic Properties of Blue Copper Proteins. *J. Am. Chem. Soc.* **120**: 13156–13166.   48, 49

[Quinteros and Bjuggren, 1998a] QUINTEROS, T. AND BJUGGREN, M. (1998a). The Discrete-Dipole Approximation to Model the Optical Behaviour of Clusters of Pigments in Paper Coatings. In: *Proc. 3rd. Workshop on Electromagnetic and Light Scattering: Theory and Applications*, Bremen, Germany. Bremen University.   134

[Quinteros and Bjuggren, 1998b] QUINTEROS, T. AND BJUGGREN, M. (1998b). *PDC Progress Report 1997*. Center for Parallel Computers, chapter Paper Optics on Fujitsu VX.   134

[Quinteros *et al.*, 2000] QUINTEROS, T., NEBEKER, B., AND BERGLIND, R. (2000). Scattering from Two-Dimensional Random Surfaces. In: *Northern Optics 2000 and EOSAM 2000*, Sweden. Uppsala.   134

[Reinhardt, 1982] REINHARDT, W. P. (1982). Complex Coordinates in the Theory of Atomic and Molecular Structure and Dynamics. *Rev. Phys. Chem.* **33**: 223.   119

[Rhie and Chow, 1983] RHIE, C. AND CHOW, W. (1983). Numerical Study of the Turbulent Flow Past an Airfoil with Trailing Edge Separation. *AIAA Journal* **21**: 1525–1532.   88

[Rodman and Brorsson, 1998] RODMAN AND BRORSSON, M. (1998). Programming Effort *vs.* Performance with a Hybrid Programming Model for Distributed Memory Parallel Architectures. Technical report, Department of Information Technology, Lund University, P.O. Box 118, SE-221 00 Lund, Sweden. Submitted for publication.   109

[Ryde *et al.*, 2000] RYDE, U., OLSSON, M. H. M., ROOS, B. O., PIERLOOT, K., AND DE KERPEL, J. O. A. (2000). On the Role of Strain in Blue Copper Proteins. Submitted.   49

[Sarman, 1995] SARMAN, S. (1995). Microscopic Theory of Liquid Crystal Rheology. *J. Chem. Phys.* **103**: 393.   53

[Sarman, 1996] SARMAN, S. (1996). Molecular Dynamics of Biaxial Nematic Liquid Crystals. *J. Chem. Phys.* **104**: 342.   51

[Sarman, 1998] SARMAN, S. (1998). Transport Properties of Liquid Crystals via Molecular Dynamics Simulation Methods. In: *Molecular Dynamics: From Classical to Quantum Methods*, edited by P. Balbuena and J. Seminario. Amsterdam: Elsevier, p. 325.   53

[Sarman, 1999] SARMAN, S. (1999). Molecular Theory of Thermomechanical Coupling in Cholesteric Liquid Crystals. *J. Chem. Phys.* **110**: 12218.   53

[Sarman, 2000] SARMAN, S. (2000). Molecular Dynamics Simulation of Thermomechanical Coupling in Cholesteric Liquid Crystals. *Mol. Phys.* **98**: 27.   53

[Sarman *et al.*, 1998] SARMAN, S., EVANS, D. J., AND CUMMINGS, P. T. (1998). Recent Developments in Non-Newtonian Molecular Dynamics. *Phys. Rep.* **305**: 1. 53

[Schmehl, 1994] SCHMEHL, R. (1994). The Coupled-Dipole Method for Light Scattering for Light Particles on Plane Surfaces. Technical report, Department of Mechanical and Aerospace Engineering, Arizona State University and the Institut für Thermische Strömungsmaschinen, Universität Karlsruhe, Germany. 134

[Schmehl *et al.*, 1997] SCHMEHL, R., NEBEKER, B. M., AND HIRLEMAN, E. D. (1997). The Coupled-Dipole Method for Scattering by Particles on Surfaces Using a Two-Dimensional Fast Fourier Transform Technique. *J. Opt. Soc. Am A* **14**: 3026–36. 134

[Schmitt and Charpin, 1979] SCHMITT, V. AND CHARPIN, F. (1979). Pressure Distibutions on the ONERA M6 Wing at Transonic Mach Numbers. Technical Report AR-138, Office National D'Etudes et de Recherches Aerospatiales. 95, 99

[Schmitt *et al.*, 1983] SCHMITT, V., DESTARAC, D., AND CHAUMET, B. (1983). Viscous Effects on a Swept Wing in Transonic Flow. Technical Report Paper 83-1804, AIAA. 99

[Schneider and Freed, 1989] SCHNEIDER, D. J. AND FREED, J. H. (1989). Spin Relaxation and Motional Dynamics. *Adv. Chem. Phys.* **73**: 387. 119

[Shalashilin *et al.*, 1998] SHALASHILIN, D. V., JACKSON, B., AND PERSSON, M. (1998). Eley-Rideal and Hot-Atom Dynamics of HD formation by H(D) incident from the gas phase on D(H)-covered Cu(111). *Faraday Discussions* **110**: 287. 113

[Sigfridsson and Ryde, 1999] SIGFRIDSSON, E. AND RYDE, U. (1999). On the Significance of Hydrogen Bonds for the Discrimination between CO and O_2 by Myoglobin. *J. Biol. Inorg. Chem.* **4**: 99–110. 49

[Simdyankin *et al.*, 2000] SIMDYANKIN, S. I., TARASKIN, S. N., DZUGUTOV, M., AND ELLIOTT, S. R. (2000). Vibrational Properties of the One-Component σ-Phase. *Phys. Rev. B* **62**: 3223–3231. 140

[Smith and Forester, 1999] SMITH, W. AND FORESTER, T. (1999). *The DL_POLY Project*. TCS Division, Daresbury Laboratory, Daresbury, Warrington, England, 1999. 34

[Spalart and Allmaras, 1992] SPALART, P. R. AND ALLMARAS, S. R. (1992). A One-Equation Turbulence Model for Aerodynamic Flows. Technical Report Paper 92-0439, AIAA. 95

[Srinivasan, 1997] SRINIVASAN, A. V. (1997). Flutter and Resonant Vibration Characteristics of Engine Blades. *Journal of Engineering for Gas Turbines and Power* **119**: 742. 115

[Stipe *et al.*, 1998] STIPE, B. C., REZAEI, M. A., AND HO, W. (1998). Single-Molecule Vibrational Spectroscopy and Microscopy. *Science* **280**: 1732–1735. 113

[Strömquist *et al.*, 1998] STRÖMQUIST, J., BENGTSSON, L., PERSSON, M., AND HAMMER, B. (1998). The Dynamics of H Absorption in and Adsorption on Cu(111). *Surf. Sci.* **397**: 382. 113

[Svensson *et al.*, 1999] SVENSSON, K., BENGTSSON, L., BELLMAN, J., HASSEL, M., PERSSON, M., AND ANDERSSON, S. (1999). Two-Dimensional Quantum Rotation of Adsorbed H_2. **83**: 124, Phys. Rev. Lett. 113

[Svensson and Ausmees, 1997] SVENSSON, S. AND AUSMEES, A. (1997). Recent Results on Auger Resonant Raman Spectroscopy of Free Atoms. *Appl. Phys. A: Mater. Sci. Process* **65**: 107–114. 55

[Szabo, 1988] SZABO, K. J. (1988). Effects of Polar γ-Substituents on the Structure and Stability of Palladacyclobutane Complexes. *Theochem.* **455**: 205–211. 37

[Szabo, 1998] SZABO, K. J. (1998). Benzoquinone-Induced Stereoselective Chloride Migration in (η^3-allyl)palladium Complexes. A Theoretical Mechanistic Study Complemented by Experimental Verification. *Organometallics* **17**: 1677–1686. 37, 37

[Szabo *et al.*, 1998] SZABO, K. J., FRISELL, H., ENGMAN, L., PIATEK, M., OLEKSYN, B., AND SLIWINSKI, J. (1998). α-(Phenylselenyl) Ketones: Structure, Molecular Modelling and Rationalization of Their Glutatione Peroxidase-Like Activity. *J. Mol. Struct.* **448**: 21–28. 37

[Troullier and Martins, 1992] TROULLIER, N. AND MARTINS, J. L. (1992). Structural and Electronic Properties of C60. *Phys. Rev. B* **46**: 1754. 30

[Tulapurkara, 1997] TULAPURKARA, E. G. (1997). Turbulence Models for the Computation of Flow Past Airplanes. *Progress in Aerospace Sciences* **33**: 71–165. 95

[Ulman, 1996] ULMAN, A. (1996). Formation and Structure of Self-Assembled Monolayers. *Chem. Rev.* **96**: 1533. 33

[Vatsa, 1987] VATSA, V. N. (1987). Accurate Numerical Solution for Transonic Viscous Flow over Finite Wings. *Journal of Aircraft* **24**: 377–385. 95

[Vos and *et al.*, 1998] VOS, J. B. *et al.* (1998). NSMB Handbook. EPFL, Lausanne. 95

[Vos *et al.*, 1998] Vos, J. B., Rizzi, A. W., Corjon, A., Chaput, E., and Soinne, E. (1998). Recent Advances in Aerodynamics inside the NSMB (Navier Stokes Multi Block) Consortium. Technical Report Paper 98-0225, AIAA. 76, 94, 94

[Weber, 1996] Weber, C. (1996). Implementation of the Lower-Upper Symmetric Gauss-Seidel (LU-SGS) Implicit Method into the Navier-Stokes Multiblock Flow Solver NSMB. Technical Report TR/CFD/96/43, CERFACS. 84

[Weber and *et al.*, 1998] Weber, C. *et al.* (1998). Recent Applications in Aerodynamics with NSMB Structured MultiBlock Solver. In: *Frontiers of Computational Fluid Dynamics 1998*, edited by D. Caughey and M. Hafez. Singapore: World Scientific Publishing. 77

[Whetten *et al.*, 1996] Whetten, R. L., Khoury, J. T., Alvarez, M. M., Murthy, S., Vezmar, I., Wang, Z. L., Stephens, P. W., Cleveland, C. L., Luedtke, W. D., and Landman, U. (1996). Nanocrystal Gold Molecules. *Adv. Mat.* **8**:428. 31

[Yoon and Jameson, 1986] Yoon, S. and Jameson, A. (1986). A Multigrid LU-SSOR Scheme for Approximate Newton Iteration Applied to the Euler Equations. Technical Report CR-179524, NASA. 84, 96

Index